Investigating Large Quantum States with Telecommunication-band Integrated Photonics



Merritt Moore

Corpus Christi College

University of Oxford

A thesis submitted for the degree of

Doctor of Philosophy

Trinity 2017

This thesis is dedicated to

my mom,

forever my double black belt guardian angel

Acknowledgements

I would like to express my deep gratitude to Professor Ian Walmsley, my research supervisor, for his wise guidance, enthusiastic encouragement and support. It has been an incredible experience with the most inspiring group! I would like to thank Dr. Andreas Eckstein for his advice and encyclopedic technical knowledge throughout the experiments. I thank Dr. Steve Kolthammer for his incredible wisdom, and I could not have asked for a better mentor than Dr. Benjamin Brecht, who helped guide me through this writing process-thank you! Also thank you Dr. Mihai Vidrighin, Thomas Hiemstra, Joelle Boutari, Gil Triginer, William Clements, Dr. Helen Chrzanowski, Dr. Jelmer Renema, for the discussions and guidance.

Finally thank you Schuyler being a rockstar sister. We've been through a lot, but together we can get through anything. Thank you dad. Thank you von Clemm Fellowship, Iselin family, Michelle, Sandy, Rose for the endless support and for being such angels.

Abstract

In this thesis, I generate, characterize, and utilize quantum states with up to eight photons. In particular, I measure the interference of heralded two-photon Fock states, which has not been possible before this work. My results demonstrate that these states provide increased measurement precision compared to coherent states, a result that is of great interest for the field of quantum metrology. To investigate this, I built photon sources at telecom wavelengths, minimised optical loss, and integrated these sources with single-photon number resolving detectors. Specifically, I used periodically poled KTP waveguides for my spontaneous parametric downconversion sources and worked with superconducting photon number resolving transition edge sensors. This enabled me to characterise my source to a very high level of detail, by measuring and analysing the resulting joint photon number statistics. From a single measurement, I am able to infer all significant parameters describing the properties of the photon source including noise contributions, determine relative weights and give an accurate measure of the systems overall efficiency. Further, I developed an innovative theory, which accurately predicts the measurement results using actual experimental parameters. Based on this theory, I am able

to suggest immediate next steps to further increase the performance of my setup. This work paves a route towards new approaches to studying 'high' photon number states for quantum metrology.

Author's Publications

1. J. Sperling, A. Eckstein, W. R. Clements, M. Moore, J. J. Renema, W. S. Kolthammer, S. W. Nam, A. Lita, T. Gerrits, I. A. Walmsley, G. S. Agarwal, and W. Vogel, "Identification of nonclassical properties of light with multiplexing layouts," Phys. Rev. A 96, 013804 (2017).

2. J. Sperling, W. Clements, A. Eckstein, M. Moore, J. Renema, W. Kolthammer, S. Nam, A. Lita, T. Gerrits, W. Vogel, G. Agarwal, and I. Walmsley, "Detector-Independent Verification of Quantum Light," Phys. Rev. Lett. 118, 163602 (2017).

3. S. Barz, V. Dunjko, F. Schlederer, M.Moore, E. Kashefi, and I. Walmsley, "Enhanced delegated computing using coherence," Phys. Rev. A 93, 032339 (2016).

4. J. Spring, P. Salter, P. Mennea, B. Metcalf, P. C. Humphreys, M. Moore, J. C. Gates, N. Thomsa-Peter, M. Barbieri, X. Jin, N. K. Langford, S. W. Kolthammer, P. G. Smith, M. Booth, B. J. Smith, and I. A. Walmsley, "Quantum interference of multiple on-chip heralded sources of pure single photons," in Research in Optical Sciences, OSA Technical Digest (online) Optical Society of America,

(2014).

5. P. Humphreys, B. Metcalf, J. Spring, M. Moore, P. Salter, M. Booth, S. Kolthammer, and I. Walmsley, "Strain-optic active control for quantum integrated photonics," Opt. Express 22, 21719-21726 (2014).

6. P. Humphreys, B. Metcalf, J. Spring, M. Moore, X. Jin, M. Barbieri, S. Kolthammer, and I. Walmsley, "Linear Optical Quantum Computing in a Single Spatial Mode," Phys. Rev. Lett. 111, 150501 (2013).

7. J. Spring, P. Salter, B. Metcalf, P. Humphreys, M. Moore, N. Thomas-Peter, M. Barbieri, X. Jin, N. Langford, W. Kolthammer, M. Booth, and I. Walmsley, "On-chip low loss heralded source of pure single photons," Opt. Express 21, 13522-13532 (2013).

Contents

1 Introduction **1**

1.1 Preface 1

1.2 HOM Interference 4

1.3 Multi-photon interference 7

1.4 Experiment 8

1.4.1 Periodically Poled KTP waveguides 9

1.4.2 Setup 11

1.5 Structure of this thesis 16

2 Our sources: Parametric Downconversion Theory **18**

2.1 Theoretical description of SPDC 19

2.1.1 Classical description of non-linear processes 19

2.1.2 Quantum non-linear process - SPDC 21

2.2 Simulation - Spectral distribution of output state 25

2.2.1 Pump envelope function 26

2.2.2 Phasematching function 26

2.2.3 Joint Spectral Intensity 31

2.2.4 Detecting single photons with DCF fiber 35

2.2.5 Stimulated emission tomography 37
2.3 Techniques to experimentally measure joint spectral intensity 37
2.4 Summary 42

3 Further source characterization **43**
3.1 Schmidt decomposition 44
3.1.1 Schmidt number lower bound from measured JSI 46
3.1.2 Schmidt modes → Two-mode squeezing 48
3.2 Correlation function and photon number statistics 51
3.2.1 Experiment 52

4 Joint photon statistics and heralding photon number states **56**
4.1 Introduction 56
4.2 Detection 58
4.2.1 Operating principle 58
4.2.1.1 Click detectors (in particular InGaAs SPADs) 59
4.2.1.2 Superconducting transition edge sensor 59
4.2.2 Caveats when using these detectors 63
4.2.2.1 TES response 66
4.2.3 Photodetection theory 67
4.2.3.1 Simple mathematical model for perfect detectors . . 67
4.2.3.2 Including loss theory 69
4.2.3.3 Measuring Loss - Klyshko Efficiency 70
4.3 Photon-number statistics measurements 73

4.3.1 Theory of different field contributions 73
4.3.2 Marginal photon-number statistics 76
4.3.2.1 Theory expressions 76
4.3.2.2 Measurements and fits to data 78
4.3.3 Joint photon-number statistics 79
4.3.3.1 Theory 80
4.3.3.2 Measurements and fit to data 82
4.3.4 Correlation functions 85
4.3.4.1 Unheralded $g^{(2)}$ 85
4.3.4.2 Heralded $g^{(2)}$ 87
4.3.5 Heralding higher photon number states 88
4.4 Conclusion 89

5 Quantum Interference of Photon Number States 92

5.1 HOM interference with balanced beam-splitter 93
5.1.1 Full broadband theory 93
5.1.2 Single Photon HOM Experiment 98
5.2 Theory of Multiphoton HOM interference 101
5.2.1 Mach-Zehnder interferometer analogous to variable beam-splitter model 101
5.2.2 Potential applications - Measuring increased sensitivity 108
5.2.3 Joint probability distribution and loss simulations 112
5.3 Experimental measurements 117

5.3.1 Determining BS ratio from single counts 118

5.3.2 Multi-photon experimental measurements 119

5.4 Pressing forward for higher-photon number heralded Fock states . . . 123

6 Conclusion **126**

A Schmidt number from mean photon number weights **131**

Bibliography **134**

List of Figures

1.1 Probability of generating one, two and three PDC photon pairs . . . 3

1.2 Single photon interference at a 50:50 beam-splitter 5

1.3 Beam-splitter reflection and transmission coefficients 5

1.4 Mach-Zehnder interferometer 7

1.5 Mach-Zehnder interferometer measured signal model 8

1.6 Layout of the experimental setup 11

1.7 Laser beam intensity profile 13

2.1 SPDC momentum and energy conservation 23

2.2 Simulated pump envelope function 27

2.3 Phasematching types 28

2.4 Quasi-phasematching 29

2.5 Simulated phasematching function 30

2.6 Simulated joint spectral intensity 31

2.7 Simulated correalted and uncorrelated JSI 33

2.8 Experimental setup to measure single photons with DCF fiber 36

2.9 Reconstructing the JSI 38

2.10 Experimental setup for stimulated emission tomography 39

2.11 Experimental JSI 40

2.12 Marginal spectrum of idler photons form two sources 41

3.1 SPDC optical pulse modes and Schmidt coefficients 45

3.2 Illustration of the mode operators 46

3.3 Connection between frequency correlations and broadband Schmidt modes 47

3.4 SPDC as an ensemble of independent two-mode squeezers 48

3.5 Measuring state with multiple Schmidt modes 50

3.6 Experimental setup for unheralded $g^{(2)}$ measurement 53

3.7 Unheralded $g^{(2)}$ measurements 54

4.1 Simple SPDC model 58

4.2 SPAD schematic 60

4.3 TES schematic 61

4.4 TES traces 62

4.5 TES photon number histogram 62

4.6 Table comparing detectors 64

4.7 Experimental TES histograms 66

4.8 Model loss with beam-splitter 70

4.9 Setup for Klyshko measurements 72

4.10 Experimental Klyshko efficiencies 73

4.11 Detailed model of SPDC process 74

4.12 Poissonian and thermal probability distributions 76

4.13 Poissonian and thermal probability distributions multiple 77
4.14 Experimental photon number distribution for range of mean photon numbers 78
4.15 Marginal photon-number probability distributions 80
4.16 Experimental mean photon number vs pump power 81
4.17 Simulations of joint probability photon-statistics 82
4.18 Normalized cross sections of the joint photon number probability distributions 83
4.19 Experimental joint probability photon-statistics 84
4.20 Experimental and simulated unheralded $g^{(2)}$ 86
4.21 Simulated heralded $g^{(2)}$ vs transmission efficiency 88
4.22 Experimental and simulated heralded $g^{(2)}$ 89

5.1 Setup for HOM interference 93
5.2 Sample theory HOM dip 97
5.3 Experimental Heralded two-photon HOM-dip 100
5.4 Mach-Zehnder interferometer 102
5.5 Mach-Zehnder interferometer measured signal model 104
5.6 Simulated normalized probabilities for the 1111, 2222, and 3333 case . 108
5.7 Multiport interferometer 109
5.8 Interferometers with specific distribution of beam splitter reflectivities 110
5.9 Modelling two sources 112
5.10 Simulation different efficiencies for 1111, 2222, 3333, 4444 case 116

5.11 Sensitivity plot for low efficiencies 117

5.12 Reconstructing the JSI 119

5.13 Experimental data plots for 0000, 1111, 2222 case 120

5.14 Experimental 1111, 2222 case and fits 121

5.15 Normalized probabilities for the 1111 and 2222 experimental case . . 123

Chapter 1

Introduction

1.1 Preface

There is significant interest in harnessing the unusual quantum mechanical phenomena to surpass classical capabilities. For example quantum key distribution can improve secure communication [9, 10], quantum computers can be more powerful than classical computers [64, 83], and quantum measurements can be more precise than classical measurements [41]. To benefit from these advantages, these applications often rely on photons because they offer fast transmission and do not interact strongly with their environment. Depending on the application, sometimes single photons or multi-photon states are necessary. For example quantum key distribution benefits strongly from the presence of single photons to circumvent photon-number splitting attacks, whereas quantum metrology benefits from larger states.

This raises the question: how do we generate large quantum states with many photons (either many linked single photons or one big multi-photon construct)? Ideally we want perfect single photon sources and then larger states can be built by combining photons. One option is to use deterministic single photon-emitting sources, such

as quantum dots [58, 92, 97], ions [48], and atoms [79, 60, 66], but these approaches generally have difficulty scaling up because of the required complex technology that impedes progress towards precision control of large quantum states. As an alternative, we can use photon-pair sources and heralding [73, 104, 17]. Unfortunately, photon pair sources are probabilistic, so we do not necessarily generate photons every time we trigger the source, and sometimes we generate too many photons. This behavior will be discussed in more detail in Chapter 4, where we will show that this seeming disadvantage can actually be an opportunity to generate quantum states with more than two photons. This has not been possible until recently, because the combination of bright sources and efficient detectors has just started to emerge.

Now there have been technological developments that enable the realization of heralded single-photon sources at telecom wavelengths. This is of particular interest because of the potential for low losses and mature telecommunication technology. Firstly, it has been demonstrated that a very promising bright spontaneous parametric downconversion source (SPDC) of pure heralded single photons, is possible with periodically poled potassium titanyl phosphate (KTP) waveguides [32, 45]. SPDC is a nonlinear interaction which causes pump photons to be converted into pairs of daughter photons, traditionally called signal and idler (to be discussed more in Chapter 2). The signal arm is then measured to herald the presence of photons in the idler arm. Such a source is technically simple - it is set up at room temperature without a need for a vacuum system. We will discuss more of the experimental setup later in this chapter. To make sure that we get the most out of our sources, it is necessary to have a setup that is as efficient as possible and to have a way to discard unwanted

events. Figure 1.1 shows the probabilities to generate a certain number of photon pairs as a function of the squeezing, which is the strength with which we drive the PDC. We see that for the most efficient single photon pair rate, higher photon number pairs will also be present, so photon-number resolving detection would be necessary to select a specific photon number state. There now exist photon-number resolving,

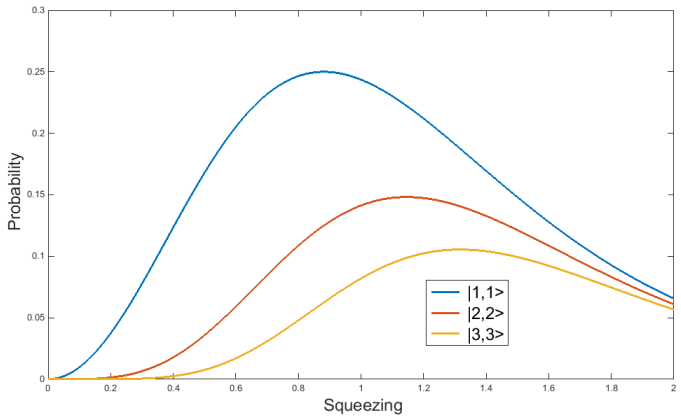


Figure 1.1: This plot shows the probability of generating exactly one, two and three photon pairs in PDC as a function of squeezing strength, colored blue, red, and yellow respectively. The probability for exactly one photon pair peaks at 25%, which already has a significant amount of higher-order components [24]. Therefore to attain the maximum number of single photon pairs, photon-number resolved detection is required to discard the higher photon-number events.

super-efficient detectors that are compatible with integrated optics platforms (to be discussed more in Chapter 4). We are, therefore, in an excellent position because we can now leverage these advances in detectors and waveguide downconversion sources. This enables us to generate, characterize, and utilize quantum states with up to eight photons to see a measurement signature that has not been seen in the lab before (to be discussed more in Chapter 5).

1.2 HOM Interference

Hong-Ou-Mandel interference (HOM) is one of the most basic quantum interference effects, where something happens that goes against our "classical" intuition. It was first demonstrated in 1987 [51], where the pair photons from a PDC source were interfered on a balanced beam-splitter. It has since been identified as the most fundamental building block for photonic quantum technologies and the archetype of quantum interference between independent single photons [64]. In HOM interference something counter-intuitive happens: two indistinguishable photons that are sent into the two input ports of a balanced beam-splitter bunch and always exit the beam-splitter together and it cannot be known from which port they exit. So why does this bunching occur? It is because the two probability amplitudes that describe both photons being reflected and both being transmitted interfere destructively, leaving only the outcomes shown in Figure 1.2.

From energy conservation, we arrive at the Heisenberg unitary transformation that relates the input modes, a and b, to the output modes, c and d, and use the asymmetric beam-splitter description, where the beam-splitter has the reflection and transmission coefficients labelled R and T and a phase shift occurs only for one reflection, shown in Figure 1.3.

$$\hat{c}^\dagger = R\hat{a}^\dagger + T\hat{b}^\dagger \tag{1.1}$$

$$\hat{d}^\dagger = T\hat{a}^\dagger - R\hat{b}^\dagger. \tag{1.2}$$

The phase relationship gives rise to the minus sign in the second equation so that

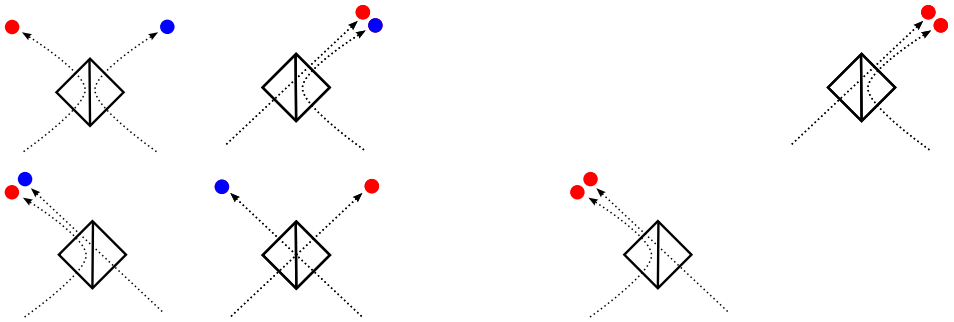


Figure 1.2: A representation of single photon interference at a 50:50 beam-splitter, which is a partially reflecting mirror with two input and two output ports and the same reflection and transmission coefficients. Figure (a) shows the four possible outcomes when the single photons entering at the two input ports of the beam-splitter and distinguishable: either one photon is reflected and the other is transmitted, or both photons are reflected, or both are transmitted. Figure (b) shows the scenario when the single photons entering at the two input ports of the beam-splitter are indistinguishable. Photon bunching is observed due to the fact that the two outcomes, when both are reflected and transmitted, destructively interfere.

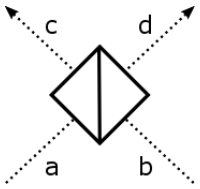


Figure 1.3: The equations in (1.2) describe output modes, c and d, given the reflection and transmission coefficients R and T and the inputs, a and b, as shown in the beam-splitter figure to the right.

R and T are real, and energy conservation requires $R^2+T^2 = 1$. It is useful to describe the beam-splitter with a matrix, H_{bs} (and we will refer back to this in Chapter 5):

$$H_{bs} = \begin{bmatrix} R & T \\ T & -R \end{bmatrix} \tag{1.3}$$

Let us look at the transformation in terms of the creation operators from equation

(**??**):

$$|\psi_{\text{in}}\rangle = \hat{a}^\dagger \hat{b}^\dagger |0\rangle \tag{1.4}$$

$$\xrightarrow{H_{bs}} (R\hat{c}^\dagger + T\hat{d}^\dagger)(T\hat{c}^\dagger - R\hat{d}^\dagger) |0\rangle \tag{1.5}$$

$$= (RT\hat{c}^\dagger\hat{c}^\dagger - R^2\hat{c}^\dagger\hat{d}^\dagger + T^2\hat{d}^\dagger\hat{c}^\dagger - TR\hat{d}^\dagger\hat{d}^\dagger) |0\rangle . \tag{1.6}$$

If single photons are injected simultaneously at both inputs, a and b, of a 50:50 beam-splitter, then classically we would assume that there are four possible ways the photons could exit (see Figure 1.2- both are reflected, both are transmitted, or one is reflected and the other transmitted). However, there are not four possible arrangements as one might assume, but rather only two, as we introduced in Figure 1.2. When we substitute in the transmission and reflection coefficients of a 50:50 beam-splitter, $R = T = (1/\sqrt{2})$, and recognize that $\hat{c}$ and $\hat{d}$ commute, then equation (1.6) reduces to:

$$\begin{aligned} |\psi_{\text{out}}\rangle &= \frac{1}{\sqrt{2}}(\hat{c}^\dagger\hat{c}^\dagger - \hat{d}^\dagger\hat{d}^\dagger) |0\rangle \\ &= \frac{1}{\sqrt{2}}(|20\rangle - |02\rangle). \end{aligned} \tag{1.7}$$

The two terms with one photon in each output mode have interfered destructively and cancelled each other out. This means that the two photons from each input will always emerge together in the same output mode, but this only is possible when the photons are indistinguishable in all degrees of freedom and pure (as opposed to a mixed state). To clarify the quality of interference depends on the photon indistiguishability, meaning identical in their physical properties (i.e., polarization, spatio-temporal mode structure, and frequency), and by purity, meaning that the state cannot be written as a mixture of other states.

1.3 Multi-photon interference

It has been shown that multi-photon states (for instance squeezed vacuum states with N> 2) can be advantageous for quantum metrology [29]. Let us consider a Mach-Zehnder interferometer, shown in Figure 5.4. With a Mach-Zehnder, the basic measurement-estimation procedure is to estimate the phase based on the value of the intensity or photon-number difference between the two output ports of the interferometer. If we sent classical laser light into one input port of the Mach-Zehnder

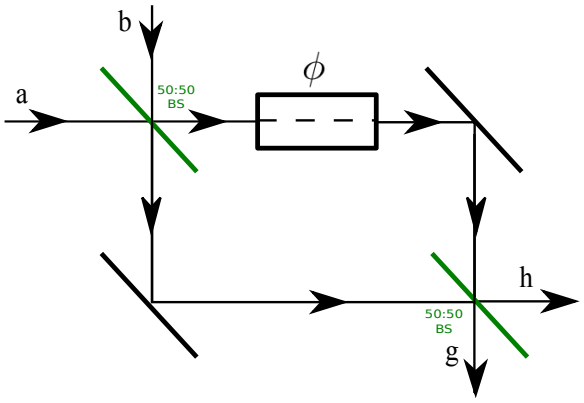


Figure 1.4: A Mach-Zehnder interferometer is a phase shift sandwiched between two balanced beam-splitters. The two input light modes are at a, b and two output modes are g, h. In a standard configuration a coherent state of light $|\alpha\rangle$ is sent into mode a. Detectors at the outputs measure the difference between the two output intensities $M = I_g - I_h$, which we shall call the signal, as a function of the phase shift, see Figure 5.5. In order to obtain quantum enhancement, one needs to make use of the b input port also, sending e.g. the squeezed vacuum state.

interferometer and measure the intensity difference betweeen the two output arms as a function of phase, we obtain the standard oscillating response shown by the red curve in Figure 5.5. Now, if we feed it with single photons instead, we get a bunched state[1] after the first beam-splitter. This results in faster oscillations, shown by the

[1]The photons are found together, referred to as "bunched", in one or the other output beam-splitter arms.

green curve in Figure 5.5, when we measure the photon-number difference between the two final output ports of the interferometer. This provides higher measurement sensitivity. The same change in phase leads to a larger change in intensity, which translates to a higher sensitivity. We will continue to investigate this in more detail in Chapter 5.

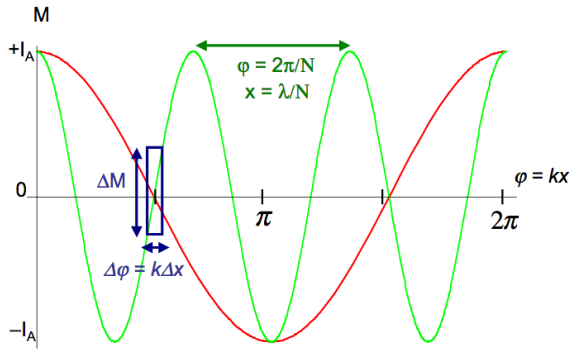


Figure 1.5: When classical light is inserted into the input ports of a Mach-Zehnder, we achieve what we refer to as the standard sensitivity. After the Mach-Zehnder, we look at the intensity of one output port as function of the phase shift (red). Where the slope of the curve $\Delta M/\Delta\phi$ is largest, is where we achieve minimal phase uncertainty $\Delta\phi$. In order to obtain quantum enhancement, one needs to send in for example squeezed vacuum into the input. When squeezed vacuum is inserted into the input ports of the Mach-Zehnder, we get a bunched state after the first beam-splitter, and the fringes oscillate faster, resulting in larger slopes and hence higher measurement sensitivity. This specific example shown by the green fringe is of a three photon N00N state. A N00N state is a path-entangled N-photon state, which is a superposition of N photons in one arm and zero in the other and vice versa. This signal oscillates N times as fast as the coherent state (super resolution) and has maximum slope that is N times as steep (super sensitivity). (Here is an example of N=3). Figure from [29]. The effect is as if the N00N state was composed of photons with an effective wavelength of λ/N instead of λ.

1.4 Experiment

The experimental investigations presented in this thesis are mainly based on one particular photon source setup which will be discussed in this section. While looking

at the source design we want to focus on the different technical options to optimize the photon indistinguishability which is critical for the following measurements.

As mentioned before in the introduction there are various ways of building single photon sources. The approach that we are pursuing is based on a nonlinear process called parametric down conversion, which will be discussed in detail in Chapter 2.1. The key advantage of this process is that it is an established tool for the generation of heralded single photons. We will push beyond this single-photon regime to the generation of heralded multi-photons. This gives us the ability to control the properties of its 'output' very well. This process is very well suited to us since it allows us to adapt the source properties to the very stringent requirements of our experimental measurements. To make this platform viable for future experiments there are further requirements that need to be fulfilled: scalability requires integration and indistinguishable emission between all integrated sources, high heralding efficiency is required and the heralded photons need to be pure. Therefore we choose SPDC in waveguides on a KTP chip because it fulfills the criteria of all those requirements, which will become clear in the rest of this thesis.

1.4.1 Periodically Poled KTP waveguides

The photon source design we want to focus on is based on waveguides in crystalline structure rather than bulk sources. SPDC via crystals with a waveguide structure helps to decorrelate the spatial degree of freedom from any spectral degree of freedom and eliminate spatial correlations between SPDC photons. The waveguide structure confines the pump beam and helps ensure brightness, since the geometry of a single

spatial mode waveguide helps to increase the efficiency of the interaction by two orders of magnitude compared to bulk SPDC sources [35, 91]. Waveguides are compact (for instance intricate computational circuits that use to take up meters in bulk optics can be compressed to just a few millimeters). Waveguides can be placed onto monolithic chips, which provide inherent phase stability and give the capability to be scaled up [84].

We optimize the creation of pure indistinguishable photons by using periodically poled KTP as the specific crystal to generate photon pairs via SPDC [53, 105, 45]. Recently, the study of spectrally pure state generation in periodically poled KTP crystals has significantly progressed [evans2010, gerrits2011, eckstein2011, zhou2013,jin2013, bruno2014]. Even though KTP is hard to grow, is difficult for fabrication, and has lower nonlinearity than lithium niobate or BBO, it provides a very specific dispersion which allows for the generation of pure heralded single photons without filtering. Since KTP is a ferroelectric medium, it can be periodically poled, allowing quasi phasematching (to be discussed more in Chapter 2) which provides more flexibility for SPDC. It has low absorption and scattering losses, high surface damage threshold and a high thermal conductivity. It also has low thermo-optic coefficients that allow for excellent environmental stability during the downconversion processes. Therefore we chose periodically poled KTP as the non-linear optical medium for SPDC in our highly efficient source of photon pairs. Next we discuss our setup.

1.4.2 Setup

The basic setup used for all my experiments is shown in Figure 1.6. A pump beam is spectrally and spatially filtered before it is divided into two distinct paths. It is then guided into two different waveguides on the same non-linear crystal, and the interaction of the pump beam and non-linear crystal causes the PDC process to occur inside each of these waveguides. Pairs of signal and idler photons are created and either interfered with each other and/or guided directly into fibers to be detected. I will go into the details of the setup here so it can be referred to throughout this thesis.

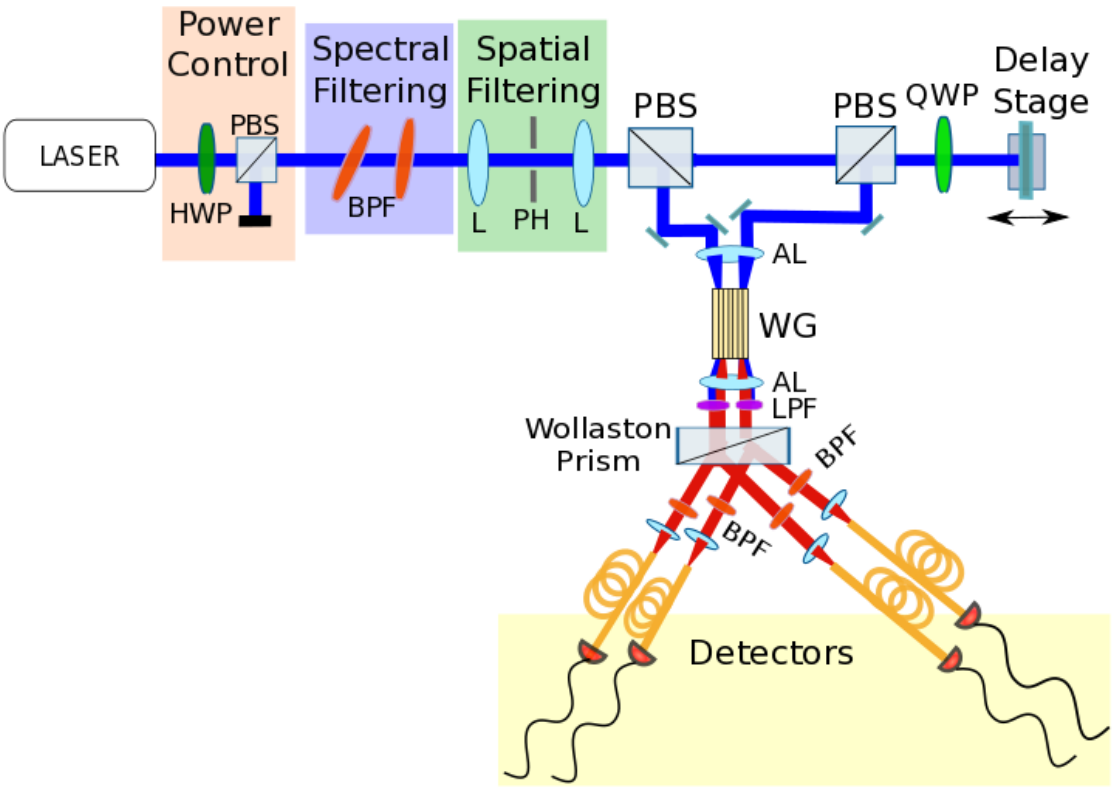


Figure 1.6: Layout of the experimental setup. Abbreviations: HWP half-wave plate, PBS polarizing beam-splitter, BPF bandpass filter, PH pinhole, L lens, QWP quarter waveplate, WG waveguide sample, LPF long pass filter, AL aspheric lens. For more information see the text.

The laser: the pump light comes from a system that consists of a CW diode pumped solid state laser (Verdi V18), a Ti:Sapphire mode-locked laser (Coherent Mira 900), and a regenerative amplifier (Coherent Rega 9000). The generated femtosecond laser pulses are purposely centered at 775 nm for our experiments, and the repetition rate is set to 80 kHz or 80 MHz, depending on the measurement. We control the power of the laser with a combination of a half-wave plate (HWP) and a polarising beam-splitter (PBS) to work at pulse energies that are roughly 1 pJ.

Spectral filter: since the pulses coming out of the laser are too spectrally broad for our experiment, 40 nm FWHM, we use two carefully chosen bandpass filters (BPF, Semrock LL01-780-25) to narrow the spectrum down to 2 nm in bandwidth. Both bandpass filters are centered around 780 nm, and by angle-tuning, the center wavelength can be shifted to shorter wavelengths[2].

Spatial filter: Ideally we want a pump beam that has a clean Gaussian intensity profile. Lasers are built and specified to be as single mode as possible but are not perfect. Our system is old and the laser is far away from the setup. In our experiment the spatial mode from the laser and is multi-mode rather than ideally single mode. In addition, as the beam passes through the setup, scattering and diffraction from optical components and dust in the air results in a distorted, spatially varying intensity profile. It is therefore important to improve the beam quality before it is focused into a waveguide so coupling can be optimised and the potential of exciting higher order processes is minimised. To do this, unwanted modes are cleaned with a spatial

[2]For the Semrock bandpass filters, the wavelength shift with angle of incidence, can be calculated by: $\gamma = \gamma_o[1 - (n_o/n_e)2sin(2\theta)]1/2$. Where γ is the wavelength at the new angle of incidence; γ_o is the center wavelength; n_o is the index of refraction of the environment ($n_o = 1$ in air); n_e is the effective index of refraction of the filter; and θ is the angle of incidence.

filter, which consists of a small pinhole aperture placed at the focal plane between two lenses. The beam is focused with the first lens. On the focal plane, the main fundamental mode will focus to a single spot in the centre and unwanted modes will show up as side fringes (see Figure 1.7).

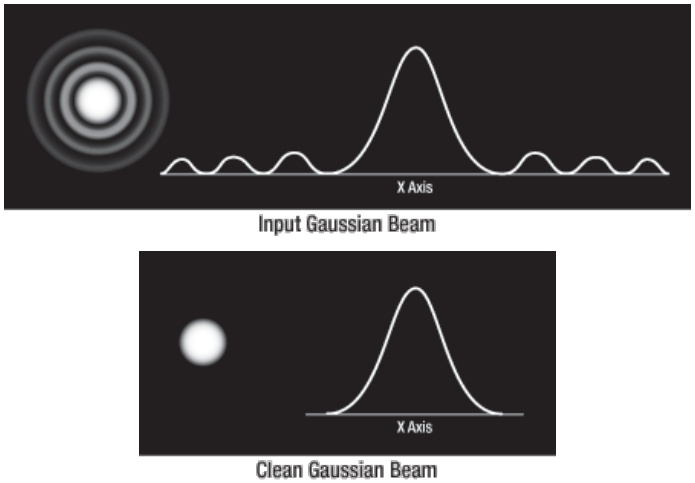


Figure 1.7: Figure (a) shows a multi-mode beam which results in a distorted spatially varying intensity profile before it is cleaned up by a spatial filter. Figure (b) shows the result after a spatial filter- clean Gaussian intensity profile.

By centering a pinhole, in our experiment this pinhole is 25 μm in diameter, on the central Gaussian spot, the clean portion of the beam will pass through while the noise fringes are blocked (see Figure 1.7).The second lens then recollimates the beam, resulting in cleaned intensity and phase Gaussian profile.

The resulting mode diameter should be carefully matched to the width of the waveguide since the waveguide coupling efficiency is defined (in part) by the modal overlap of the guided mode of the waveguide and the spatial mode of the pump beam. Optimal efficiency is only achieved if these two modes are equal. Since the waveguide mode cannot be changed, the beam has to be adjusted to fit the waveguide by adjusting the lenses. For our setup, we adjust the width of the beam spatial

mode with the two lenses from the spatial filter which both have a focal length of $f = 50$ mm.[3] In our experiments we have found that careful pump coupling can very effectively minimize other down-conversion processes originating from higher-order spatial pump modes.

The pump is then split at the first polarizing beam-splitter into two paths so that they can be coupled into two independent waveguides. One of the paths (path A) has a reflecting mirror on a motorised linear translation stage (PI M-111) so that its pulses can be adjusted to match the timing of the pulses from the other path (path B). We use a standard experimental technique for implementing a time delay- the horizontally polarised light in path A passes straight through a PBS to reflect off the translation stage. after a 90^o degrees rotation from passing through the quarter waveplate (QWP) twice during the round-trip reflection, the light is reflected by the PBS and goes towards the source.

The two pump beams are coupled into two waveguides with an aspheric lens, (AL, Thorlabs C230TMD-B, F = 4.5 mm) that is anti-reflection coated for 600-1050 nm. Eighteen waveguides are available on the periodically poled potassium titanyl phosphate chip (PPKTP) that was bought from the company AdvR. The two waveguides we couple into and use for the experiments are 3 μm wide, 10 mm long, and have a poling period of γ =120 μm. They also have anti-reflection coatings on both ends of the chip (770 nm for the input side and 1540 nm on the output side). The signal and idler fields generated during the PDC process are centered at 1546nm and

[3]In general a spot size with a diameter larger than the waveguide profile provides pump propagation that is closer to single mode, whereas a smaller beam will tend to exhibit more multimode effects [23].

1554nm, respectively. After the WG, the generated PDC light is collimated with an AL (Thorlabs C230TMD-C, F = 4.5 mm) that is anti-reflection coated for 1050-1700 nm.

After chip filtering: a dichroic longpass filter (LPF, Semrock LP02-808RE-25) is used to filter out the remaining pump light from the PDC output. The signal and idler photons are spatially separated at deviating angles using a Wollaston prism. Unlike many other polarizers, both output beams from a Wollaston prism are highly polarized with an extinction ratio 100000:1 in each output (compared to for example a Laser-Line Polarizing Beam-splitter Cube with an 3000:1 extinction ratio). Each arm of the signal and idler beams have their own bandpass filters, which are angle-tuned for maximum output, (BPF, Semrock NIR01-1550/3-25 and BPF, Semrock NIR01-1570/3-25) for the signal and idler arms respectively. The bandpass filters have a full width at half max 6-9 nm so as to not cut off the photon spectra, but provide background suppression.

Coupling: the spatial modes of the light emitted from the waveguides is typicaly elliptical from the effective waveguide shape and refractive index profile[4] so we use cylindrical concave mirrors f=100 mm (Thorlabs CCM254-100-P01) to reshape the signal and idler beams before coupling into four FiberPorts (Thorlabs, PAF-X-5-C). The fibers (Thorlabs P1-SMF28EAR) have anti-reflection coating to optimise coupling efficiency. When coupling classical 1550 nm light, we achieve coupling efficiencies of 89% and 80%, in the idler and signal arms respectively.

[4]Imaged with a beam profiling camera (WinCamD-LCM 2 CMOS Beam Imaging Camera 190 1605 nm)

The detection scheme is different for each setup so we will discuss those details throughout the thesis when we get to the individual experiments.

1.5 Structure of this thesis

In Chapter 2, we start discussing the fundamental theory of spontaneous down-conversion sources, the building block for my experiments. The beginning of my DPhil was spent building SPDC sources at telecom wavelengths in periodically poled KTP waveguides. Understanding the theory was important to adjust experimental parameters accordingly to produce as closley as possible highly pure indistinguishable heralded photons. Once the sources are built, it is important to characterise their performance. We start by looking at and analysing the spectral correlations of the generated photon pairs. This gives us the first indication of how indistinguishable and pure the heralded photons from different sources will be. In Chapter 3, we investigate possible phase correlations by measuring the output photon number statistics to continue characterising the generated heralded photons. In doing so, we quantify the degree of spectral and temporal correlations and compare it to the spectral measurements we took in Chapter 2. In Chapter 4, we integrate our photon sources with photon-number resolving detectors which allows us to characterise our sources with a greater level of detail and improve heralding single-photon and multi-photon states. From a single measurement, we are able to infer all significant parameters describing the properties of the photon source including noise contributions, determine relative weights and give an accurate measure of the systems overall efficiency. Further, we are able to accurately simulate the measurement results using actual experimental

parameters. In Chapter 5, we measure the interference of heralded two-photon Fock states, which has not been possible before this work. Our results demonstrate that these states provide increased measurement precision compared to coherent states, a result that is of great interest for the field of quantum metrology. This work paves a route towards new approaches to studying 'high' photon number states for quantum metrology.

Chapter 2

Our sources: Parametric Downconversion Theory

For the experiments we want to pursue, our goal is to build photon sources that emit pure indistinguishable heralded photons via spontaneous parametric downconversion (SPDC). In order to do so, it is important to understand the necessary background theory because the theory is what informs which parameters are optimal to adjust when building the photon sources in the laboratory.

This chapter will focus on the quantum theory of SPDC. SPDC is a quantum process that comes about from a non-linear light-matter interaction. As a starting point, we begin with understanding the nonlinear light-matter interaction from a classical point of view, and then delve deeper to describe the quantum non-linear SPDC process with much more detail. We focus on the Type-II SPDC process, the foundation for all our experiments in this thesis, and in particular in periodically poled KTP waveguide sources. We highlight what parameters affect the spectral distribution of the SPDC output state and then discuss two different experimental methods in which we measured the joint spectral distribution in the lab.

2.1 Theoretical description of SPDC

SPDC is a quantum process that occurs when a laser beam (often referred to as the pump) propagates through a non-linear medium. This downconversion process converts pump photons into pairs of lower energy photons, called the signal and idler. A probabilistic nature is revealed when trying to prepare a specific photon-number state; although the SPCD process is deterministic, the output state is a superposition of different number of photon pairs which has a probability of collapsing to a single photon number state when heralded.

Factors such as the properties of the medium, the bandwidth of the pump, and the geometry of the setup all play a role in the downconversion process. In the following section, we describe the influence of those parameters on the resulting output state and identify ideal settings that maximize the probability of generating the desired photon-number state from the PDC process.

2.1.1 Classical description of non-linear processes

Let's start by describing the interaction when an electromagnetic field travels through non-linear medium. A driving electric field causes the atoms in the medium to acquire a net dipole moment per unit volume, a.k.a. the polarization density $\mathbf{P}(\omega)$:

$$\mathbf{P}(\omega) \approx \chi \mathbf{E}(\omega), \tag{2.1}$$

where χ is the susceptibility tensor that is characteristic of the material and ω is the frequency of the electric field, $\mathbf{E}$. At low powers, this interaction is linear and the resulting polarization causes a harmonic oscillation of the electrons. When pumped

harder with a high-intensity electric field, these oscillations become anharmonic and higher order terms need to be included in the series expansion of Equation (2.1):

$$\mathbf{P}(\omega) = \epsilon_0 \chi^{(1)} \mathbf{E}(\omega) + \underbrace{\epsilon_0 \chi^{(2)} \mathbf{E}^2(\omega)}_{\substack{\text{Term focused on} \\ \text{in this chapter.}}} + \epsilon_0 \chi^{(3)} \mathbf{E}^3(\omega) + \cdots , \tag{2.2}$$

where ϵ_0 is the vacuum permittivity, $\chi^{(1)}$ is the linear susceptibility, and $\chi^{(2)}$, $\chi^{(3)}$, etc. are the nonlinear susceptibilities of the medium. With anharmonic oscillation, the non-linear terms of the polarization act as driving terms in the wave-equation (the moving charges themselves act as sources of electromagnetic radiation). This causes the medium to generate new frequency components.

We focus on the second-order nonlinear interaction, the $\chi^{(2)}$ term in Equation (2.2). This term drives a couple of processes. The classical processes are sum and difference frequency generation [11]. Sum frequency generation is when two input waves, by interacting with a nonlinear medium, effectively "combine to generate another wave that is the sum of two other frequencies. Second harmonic generation, also known as frequency doubling, is the most common type of sum frequency generation when both input waves have the same frequency. Difference-frequency generation results in the generation of light with a frequency that is the difference between two other frequencies. The analogous second-order nonlinear non-classical interaction that we will focus on is called spontaneous parametric down-conversion (SPDC). It is referred to as "spontaneous" because there is no input signal/fields to simulate the process. The process is "parametric" [11], meaning that the photons satisfy energy conservation, leaving the matter unchanged. Down-conversion refers to the fact that process causes a high-frequency pump photon to spontaneously splits in two lower-

frequency photons [3]. For our purposes, we will mostly ignore the $\chi^{(3)}$ term (and higher order terms) because it has a non-linear interaction that is significantly smaller than $\chi^{(2)}$[1].

In the classical picture, the interaction Hamiltonian from the interaction between the polarization, Equation (2.1), and the electric field over the interaction volume V is:

$$H_{\text{Int}} = \int_{\text{V}} dV \mathbf{P}(\omega) \cdot \mathbf{E}(\omega). \tag{2.3}$$

We will now compare this to the quantum picture.

2.1.2 Quantum non-linear process - SPDC

The SPDC process is a strictly quantum effect and cannot be explained in terms of classical nonlinear optics. To see how certain physical parameters affect the emitted photon's spectral properties, it is useful to look more closely at the SPDC interaction Hamiltonian. The main takeaway from this section is that the SPDC process is governed by two conservation criteria: energy and momentum conservation.

For this quantum process, we rewrite the interaction Hamiltonian, Equation (2.3), for the second order contribution, $\mathbf{P}(\omega) \rightarrow \epsilon_0 \chi^{(2)} \mathbf{E^2}(\omega)$, in terms of quantized electric fields:

$$\hat{H}_{\text{PDC}} \propto \chi^{(2)} \int_0^L dz \hat{E}_{\text{p}}^{(+)} \hat{E}_{\text{s}}^{(-)} \hat{E}_{\text{i}}^{(-)} + h.c. \tag{2.4}$$

Our experiments use waveguides in crystals as sources, so we assume single spatial-mode collinear propagation and therefore integrate over the waveguide length L (for

[1]For reference, the $\chi^{(3)}$ term becomes important in centrosymmetric mediums where the $\chi^{(2)}$ process is not possible since the ordered susceptibilities cancel due to inversion symmetry [11]. The $\chi^{(3)}$ term is associated with four-wave mixing, self-phase modulation, and cross-phase modulation.

more general PDC treatments see [50, 40, 88, 26]). $\hat{E}_{\mathrm{p}}$, $\hat{E}_{\mathrm{s}}$, and $\hat{E}_{\mathrm{i}}$ represent the quantised pump, signal, and idler fields respectively, which can be expressed in terms of the creation/annihilation operators $\hat{a}$, $\hat{a}^{+}$, which obey [72]:

$$\left[\hat{a}(\omega), \hat{a}(\omega')^{\dagger}\right] = \delta(\omega - \omega') \qquad [\hat{a}(\omega), \hat{a}(\omega')] = 0, \tag{2.5}$$

where ω is the frequency of the field. The quantised electric field of signal and idler then takes the form:

$$\hat{E}_{s,i}^{(-)}(z,t) = \hat{E}_{s,i}^{(+)\dagger}(z,t) = C \int d\omega_{s,i} e^{-i(k_{\mathrm{s,i}} z - \omega t)} \hat{a}_{\mathrm{s,i}}^{\dagger}(\omega), \tag{2.6}$$

in which all constants and slowly varying field amplitudes have been merged in the overall parameter C, k is the wave vector, and z is the position along the waveguide. The pump field is a strong laser field which is negligibly depleted, so it can be treated as a classical field:

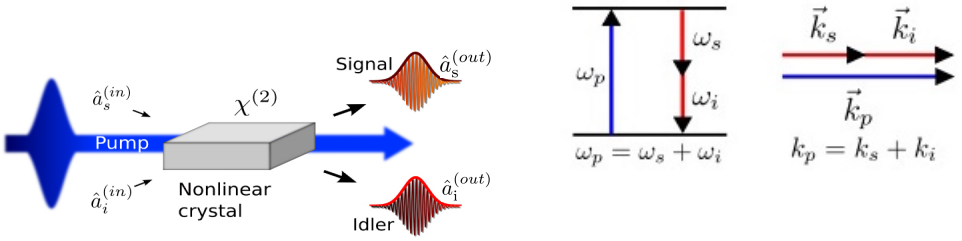
$$E_{\mathrm{p}}^{(+)} \propto \int \mathrm{d}\omega_{\mathrm{p}} e^{i(k_p z - \omega_p t)} \alpha(\omega_{\mathrm{p}}), \tag{2.7}$$

where $\alpha(\omega_p)$ is the pump envelope function generated by an ultrafast laser system, and normalizes $\int d\omega \left|\alpha(\omega)\right|^2 = 1$.

From the effective PDC Hamiltonian in Equation (2.4), the unitary transformation that describes the transformation of the beams during propagation through the crystal can be generated from the Schrödinger equation [89, 83]:

$$\hat{U} = \exp\left[\frac{-i}{\hbar} \int_0^T dt \hat{H}_{\mathrm{PDC}}(t)\right]. \tag{2.8}$$

In the low gain regime of the presented experiments, time-ordering effects can be neglected [103, 74, 87]. By combining Equations (2.4), (2.6) and (2.7), the unitary from Equation (2.8), which can be rewritten as:



(a) SPDC process

(b) Energy and phasematching conservation

Figure 2.1: In the SPDC process, a pump beam in arm $\hat{a}^{(in)}$ and vacuum in arm $\hat{b}^{(in)}$ interacts with a nonlinear crystal and generates two daughter beams, the signal and idler. The spectral properties for the generated photon-pair are determined by momentum and energy conservation between the three interacting fields. [21]

$$\hat{U} = \exp\left[-\frac{i}{\hbar}\left(C\iiint d\omega_{\mathrm{p}} d\omega_{\mathrm{s}} d\omega_{\mathrm{i}} \underbrace{\int_{-\infty}^{\infty} dt' e^{\mathrm{i}\Delta\omega t}}_{\substack{\text{Energy}\\ \text{Conservation}}} \underbrace{\int_{L_z} dz e^{\mathrm{i}\Delta k z}}_{\text{Phasematching}} \underbrace{\alpha(\omega_{\mathrm{p}})}_{\substack{\text{Pump}\\ \text{Envelope}}} \hat{a}_{\mathrm{s}}^{\dagger}(\omega_{\mathrm{s}}) \hat{a}_i^{\dagger}(\omega_i)\right) + h.c.\right], \tag{2.9}$$

where C denotes the overall efficiency of the SPDC process that depends linearly on the length of the crystal and the field amplitude of the pump beam, and $\Delta\omega = \omega_s + \omega_i - \omega_p$ and $\Delta k = k_s + k_i - k_p$. The Hermitian conjugate, $h.c.$, from the Hamiltonian, $\hat{H}_{PDC}$, in Equation (2.4) is zero because $\hat{E}_{\mathrm{s}}^{(+)} \hat{E}_{\mathrm{i}}^{(+)} |0\rangle \propto \hat{a}_{\mathrm{s}} \hat{a}_{\mathrm{i}} |0\rangle = 0$.

We work in the interaction picture and ignore time-ordering effects, which are insignificant for our measurements [87]. The interaction time, t, of the fields passing through the crystal is long compared to the ultrashort pump pulses[2], so that the time integral in Equation (2.9), labelled "Energy Conservation", can be approximated from negative infinity to positive infinity, $\int_0^T dt \to \int_{-\infty}^{\infty} dt$ to a delta function $\delta(\Delta\omega)$ [40].

[2]The interaction time is approximately 10^{-11}s compared to the ultrashort pulses which are approximately 10^{-13}s.

This delta function enforces the energy conservation condition:

$$\int_{-\infty}^{\infty} dt e^{\mathrm{i}\Delta\omega t} = \delta(\Delta\omega)$$

$$\omega_{\mathrm{p}} = \omega_{\mathrm{s}} + \omega_i \quad \rightarrow \quad \text{Energy Conservation,}$$

which means the pairs of signal and idler photons can only be produced if their combined energy equals the energy of the pump photon.

Momentum conservation manifests itself in the next integral from Equation (2.9). This integral is labelled as the phasematching function $\phi(\omega_{\mathrm{s}}, \omega_i)$:

$$\phi(\omega_{\mathrm{s}}, \omega_i) \approx \int_0^{L_z} dz e^{\mathrm{i}\Delta kz} = L_z \mathrm{sinc}\left(\frac{\Delta k L_z}{2}\right) e^{i\frac{\Delta k L_z}{2}}, \tag{2.10}$$

where $\Delta k = k_{\mathrm{p}} - k_{\mathrm{s}} - k_{\mathrm{i}}$ and $\mathrm{sinc}(x) = \sin(x)/x$. This shows that the conversion process of pump photons into daughter photons is most efficient when the sum of the momenta of the signal and idler photons are equal to the momentum of the pump photon:

$$k_{\mathrm{p}} = k_{\mathrm{s}} + k_i, \quad \rightarrow \quad \begin{array}{c}\text{Momentum Conservation} \\ \text{a.k.a Phasematching}\end{array} \tag{2.11}$$

If the phasematching condition is met, the intensity of the generated SPDC fields will grow at a steady quadratic growth with crystal length. However if $\Delta k \neq 0$, the generated field becomes out of phase and destructively interfere every coherence length. There are techniques to overcome these barriers. Such as quasi-phasematching, which we will explain in section 2.2.2.

In conclusion the SPDC process is governed by energy and momentum conservation. The next crucial step is to see what parameters can be adjusted to tailor the two-photon spectral output to ensure a factorable photon-pair state, from which

we can herald pure and indistinguishable photons. If the state is non-factorable, heralding will cause the idler state to collapse into a mixed state. A measurement of a non-factorable state can not distinguish the degree of freedom that the correlation exists. In other words, detection of the heralding photon collapses the state of the heralded photon in a way that can be different from one pair to the next [34]. Therefore, factorable states are desirable because the characteristics of the heralded photon are completely independent of the measurement obtained from detection of the heralding photon. This will be discussed in more detail in Chapter 3.

2.2 Simulation - Spectral distribution of output state

To focus on the spectral properties of the resulting two-photon state, the unitary from Equation (2.9) is simplified to the form:

$$|\Psi_{out}\rangle = \exp\Bigg[-\frac{i}{\hbar}\Bigg(C \int_0^\infty d\omega_s d\omega_i \underbrace{f(\omega_s,\omega_i)}_{\substack{\text{Spectral}\\ \text{Information}}} \hat{a}_s^\dagger(\omega_s)\hat{a}_i^\dagger(\omega_i)\Bigg) + \text{ h.c.}\Bigg]\Big]\,|0\rangle\,. \tag{2.12}$$

This is done by combining the product of the phasematching function $\phi(\omega_s,\omega_i)$, Equation (2.10), and the pump envelope function $\alpha(\omega_s+\omega_i)$, Equation (2.7), into what we define as the joint spectral amplitude (JSA), $f(\omega_s,\omega_i)$:

$$f(\omega_s,\omega_i) = \alpha(\omega_s+\omega_i)\phi(\omega_s,\omega_i), \tag{2.13}$$

The JSA holds all the spectral and temporal information about the resulting two-photon state. Lets take a closer look at how the pump function and phasematching function affect correlations between the signal and idler.

2.2.1 Pump envelope function

The pump envelope function $\alpha(\omega_s + \omega_i)$ is assumed to a single transverse mode that is modelled as a Gaussian function:

$$\alpha(\omega_s + \omega_i)) = A_p \exp\left[\left(\frac{\omega_s + \omega_i - \omega_{p0}}{\sigma_p}\right)^2\right], \tag{2.14}$$

where A_p is the field amplitude, ω_i and ω_s are the idler and signal frequencies respectively, ω_{p_0} is the pump central frequency, and σ_p is proportional to the full width at half maximum bandwidth of the spectral intensity.

We want the output photons central wavelength close to 1550nm in order to take advantage of the low loss telecom regime; therefore we set the central pump spectrum appropriately at 775 nm. We simulate the pump envelope function centered at 775 nm, plotted with the signal and idler wavlengths as the x and y axis, in Figure 2.2. As shown, it always lies at $-45°$ to the axis to ensure that all possible signal-idler frequency pairs satisfy conservation of energy. The width of this function in the joint spectral space is proportional to the bandwidth of the pump, FWHM_λ.

2.2.2 Phasematching function

The phasematching function, from Equation (2.10), reveals the importance of momentum conservation for optimal downconversion efficiency. The optical properties of the nonlinear crystal determine the particular configuration of an individual phasematching function. The refractive index, $n(\omega)$, as a function of frequency ω is often described by an empirical set of equations, known as the Sellmeier equations [28]. Let's look at the wave-vector mismatch Δk, from Equation (2.11), in terms of the

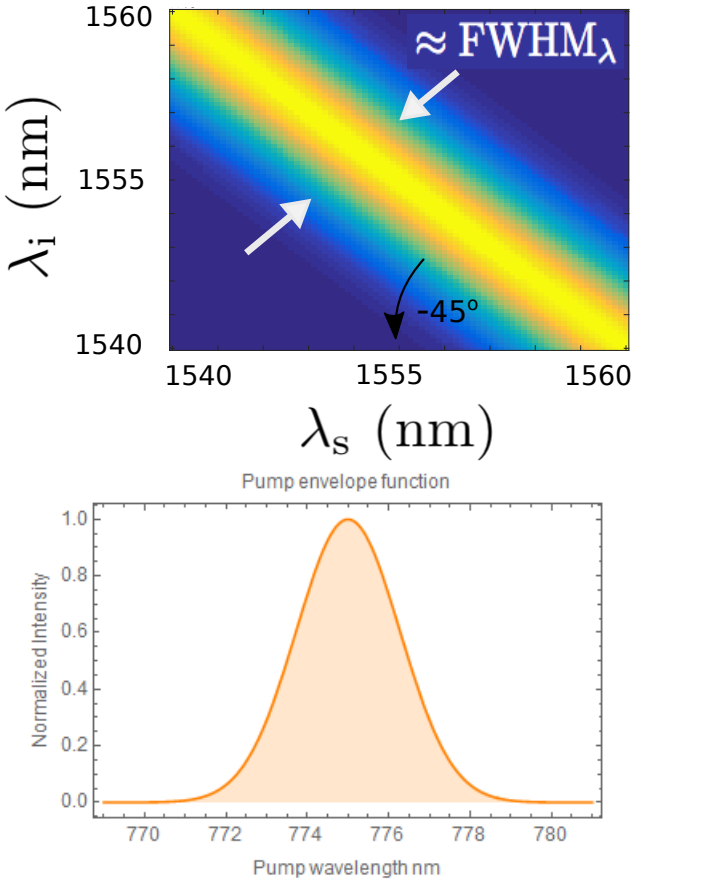


Figure 2.2: The pump envelope function of PPKTP simulated with a numerical model. The axes on the bottom and left of the figure are the wavelengths of the signal and idler respectively. The Gaussian pump envelope function is shown centered at 775 nm with a 1.8 nm FWHM bandwidth.

relation $k = \frac{n(\omega)}{c}\omega$, where c is the the speed of light:

$$\Delta k = \frac{n_{x,y,z}(\omega_\mathrm{p})}{c}\omega_\mathrm{p} - \frac{n_{x,y,z}(\omega_\mathrm{s})}{c}\omega_\mathrm{s} - \frac{n_{x,y,z}(\omega_i)}{c}\omega_i, \tag{2.15}$$

For birefringent crystals, the refractive index $n(\omega)$ is given for each of the principal axes (x, y, z) of a non-linear crystal. So depending on the polarisations of the incoming and outgoing fields there are different types of polarisation phasematching possibilities for parametric downconversion, shown in Figure 2.3: Type-0 is when the

two generated photons and the pump all have the same polarization, Type-I is where the two generated photons are identically polarized and orthogonal to the pump, and Type-II is where the two generated photons are orthogonally polarized. Specifically this model (and the experiments for this thesis) are designed for Type II SPDC, where $\hat{V}$ polarized pump is converted into orthogonal signal, $\hat{V}$, and idler, $\hat{H}$.

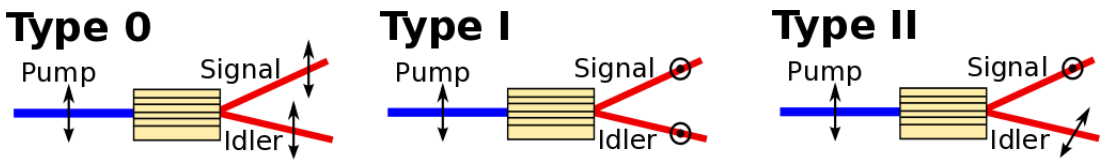


Figure 2.3: Type-0 phasematching, shown in the far left figure, is when pump signal and idler all have the same polarization. Type-I phasematching, shown in the middle figure, is full-filled if the signal and idler having the same polarization which is orthogonal to the pump. Type-II phasematching, shown in the right figure, is full-filled if the signal and idler having opposite polarizations.

When the process is perfectly phasematched by birefringence, the intensity grows quadratically with the crystal length, shown by the green curve in Figure 2.4. It is important to note that this only occurs at a specific combination of input and output frequencies; otherwise the process is non-phasematched, and the power oscillates between zero and a small value, shown by the red curve in Figure 2.4. Quasi-phasematching [37], shown by the blue curve, enables the generation of wavelengths that may not be possible with birefringent phase matching in a particular material. The resulting intensity quadratically increases with crystal length, however by a factor of $4/\pi^2$ lower than perfect phasematching. It should be noted that in practice longer crystals are not generally used since the production of longer waveguides is more susceptible to imperfections. Periodic poling in crystals is an important quasi-phasematching technique, which adds an additional phase contribution. This allows

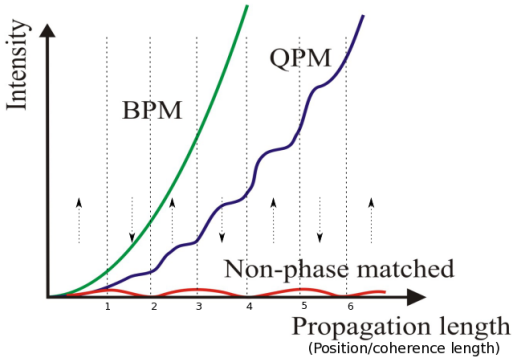


Figure 2.4: The graph shows the parametric signal generation as a function of length, with perfect phasematching by birefringence (BPM in green) and non-phasematched (in red). The quasi-phasematching technique (QPM in blue) shows how the relative phase is corrected - the crystal domain structure is periodically inverted along the length of the crystal, shown with the inverting arrows every coherence length.

flexibility in the momentum conservation condition:

$$\Delta k = k_{\mathrm{p}} - k_{\mathrm{s}} - k_i - \frac{2\pi}{\Lambda}, \tag{2.16}$$

where Λ is the poling period [11].

We simulate the phasematching function for KTP crystal with a periodic poling of $117\mu m$. The slope of the phase matching function, shown in Figure 2.5, depends on the group velocities of the three interacting waves (pump, signal and idler) in the crystal [101]:

$$\theta = -\arctan\left[\frac{(\nu_{\mathrm{s}} - \nu_{\mathrm{p}})\nu_i}{(\nu_{\mathrm{i}} - \nu_{\mathrm{p}})\nu_{\mathrm{s}}}\right] \tag{2.17}$$

where $\nu_{\mathrm{p,i,s}}$ are the group velocities for the pump, idler and signal beams respectively. In order to achieve group velocity matching such that the phasematching slope is positive, it is required that the group velocity of the pump pulse ν_{p} is in-between the group velocity of the signal ν_{s} and idler ν_{i} pulses:

$$\nu_{\mathrm{s}} < \nu_{\mathrm{p}} < \nu_{\mathrm{i}} \quad \text{or} \quad \nu_{\mathrm{i}} < \nu_{\mathrm{p}} < \nu_{\mathrm{s}}. \tag{2.18}$$

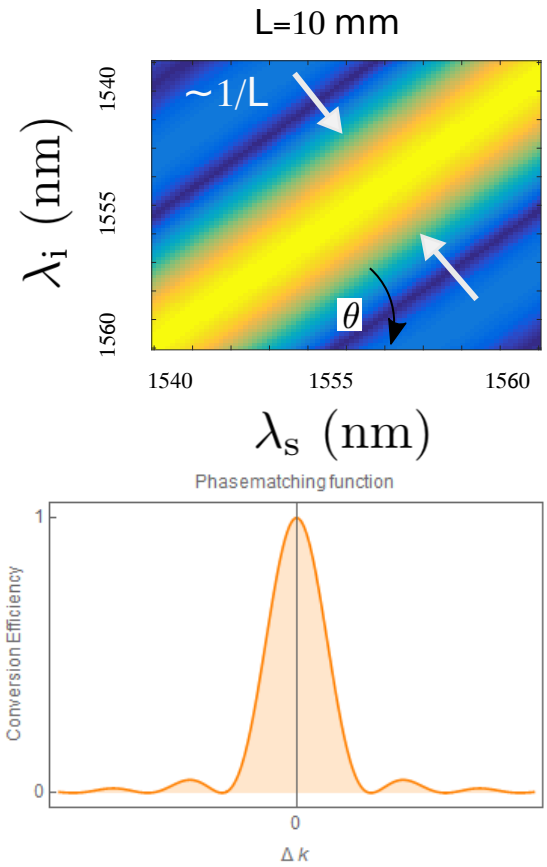


Figure 2.5: The top figure shows the phasematching function simulated with a numerical model for a PPKTP crystal with a poling period of 117μm. The axes on the bottom and left of the figure are the wavelengths of the signal and idler respectively. The right figure shows a cross section of the phasematching function, which reveals its Sinc function from.

KTP is unique because it can achieves group velocity matching for Type-II SPDC at 1550 nm. This is an important advantage because it can only be realized in limited kinds of crystals and at limited wavelengths [65, 55, 59, 36]. In the special case when the pump group velocity is equidistant from signal and idler group velocities, the phase matching function lies close to +45° to the axis as shown in Figure 2.5. The width of the phasematching function is inversely proportional to the length of the nonlinear crystal.

2.2.3 Joint Spectral Intensity

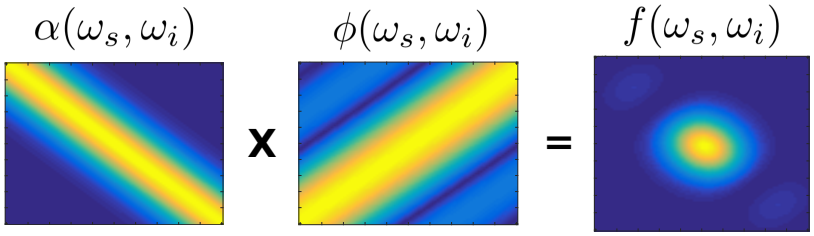


Figure 2.6: The pump envelope function, phasematching function and joint spectral intensity of PPKTP simulated with a numerical model. The pump envelope function centered at 775 nm and 1.8 nm bandwidth (FWHM). The middle figure shows the phasematching function in a PPKTP crystal with a poling period of $117\mu m$. The joint spectral intensity of PPKTP, is the product of the pump function and phasematching function with signal and idler wavelengths as two input variables.

The JSA function, from Equation (2.13), is a combination of the pump function and phasematching function shown in Figure 2.6. The JSA is crucial because it holds all the spectral-temporal information about the resulting two-photon state, including whether or not the generated states are spectrally and temporally separable or entangled. That is to say, the JSA function describes a two-photon state that can ideally be written as a separable product state of two single-photon states:

$$f(\omega_s, \omega_i) = g(\omega_i)h(\omega_s), \tag{2.19}$$

or in the non-ideal case an entangled state that is not factorable.

The JSA is hard to measure because it entails measuring the phase, however the joint spectral intensity (JSI) for the photon pairs $F(\omega_s, \omega_i)$, which is the modulus squared of the JSA:

$$\mathrm{F}(\omega_s, \omega_i) = |f(\omega_s, \omega_i)|^2. \tag{2.20}$$

can be a useful way to measure and visualize the two-dimensional probability distribution of detecting a signal photon with frequency, ω_s, and a corresponding idler

photon with frequency, ω_i.

We take a look at a couple different pump bandwidths σ_p and phasematching widths to see their effects on the overall JSI shape, plotted on the (λ_s, λ_i) spectral plane in Figure 2.7. The top row shows the calculated pump field envelope for a range of spectral widths: 0.5 nm, 1 nm and 1.8 nm. The far left column shows the simulated phasematching condition for a range of crystal lengths: 10 mm, 15 mm and 20 mm. We show the results for various JSI configurations with a 3x3 matrix. If the resulting JSI is a narrow line along the diagonal or anti-diagonal (most apparent in the top right and bottom left plots in Figure 2.7) this means the two photons from each pair are spectrally entangled. And if the signal and idler are spectrally entangled, the use of detectors that can not determine the frequency in the signal arm will leave the idler in a mixed state, which is not ideal. If the JSI is shaped as a circle, this visually shows that a frequency measurement of one of the photons from the pair will not give any information about the frequency of the other photon, and there is promise that we can write the JSA as a separable product state (2.19) [100].

We see that the case for which the JSI is optimized to be as circular as possible is when the pump bandwidth is 1.8 nm wide and the length of the crystal is 10 mm long and periodically poled at $117\mu m$. The goal is to minimize effects of frequency correlations in each source in order to increase the purity of the heralded single photon in each source. It should be noted that the sinc dependence of the phasematching function causes secondary side lobes shown in the plot, which spoils perfect factorability. Experimentally we use spectral filters to clean up the side lobes and leave the central portion of the JSA which is factorable. Some setups have to strongly filter in order to

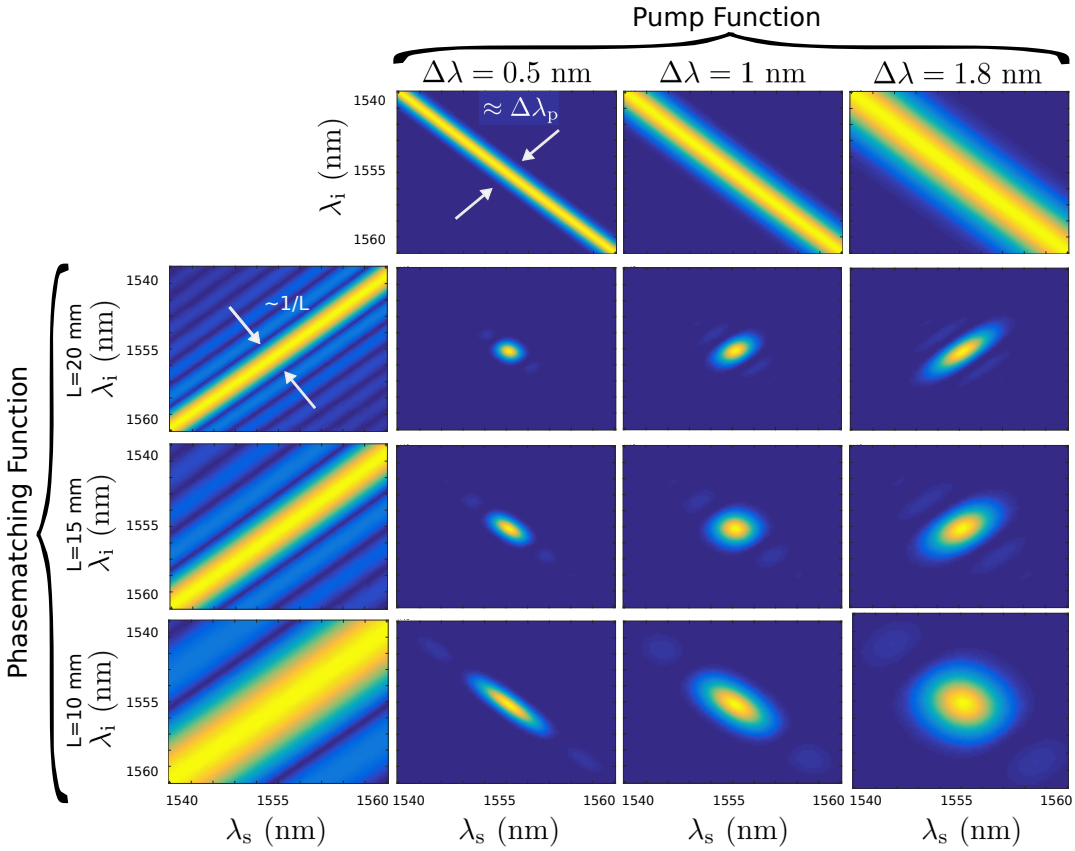


Figure 2.7: The pump function is along the top row for different pump bandwidths ($\Delta\lambda_p = 0.5$, 1, and 1.8 nm spectral intensity FWHM with a central pump wavelength of 775 nm. The phasematching function is along the far left column for different crystal lengths (L= 10 mm, 15 mm, 20 mm). The resulting theoretical JSI the lower right 3x3 array of plots as a function of the signal and idler wavelengths for periodically poled KTP. The (off-diagonal) plots show spectral correlations between the signal and idler and the on-diagonal plots shows an uncorrelated (factorable) state.

achieve a factorable output. We only have to weakly filter the side lobes for the last bit of improvement, meaning that are source still maintains 90% of its brightness.

To sum up this section, the simulations show that the heralded photons from PPKTP around 1550 nm have the potential to be highly factorable, pure and indistinguishable, when the right crystal geometry, poling period, and pump spectrum are optimized. Recent similar experiments verify this conclusion [45, 39]. We will discuss this in more detail below by comparing these simulations to the actual experimental

JSI results.

We use two different experimental methods to look at the spectral characterization of the two-photon state generated from the SPDC process. As discussed above, the joint spectral amplitude function (JSA), known as the biphoton wavefunction $f(\omega_s, \omega_i)$, characterizes the spectral-temporal correlation of the two-photon state and describes any correlation between the two emitted photons. However since the JSA is hard to measure because it entails measuring phase, the JSI (the modulus square of the JSA) is a useful way to measure and visualize the spectral correlations.

Since the JSI is composed of the phasematching and pump envelope functions, it is therefore determined by the physical parameters: pump wavelength, pump bandwidth, crystal index of refraction, crystal length, and periodic poling. Adjusting these variables can change the central wavelength of signal and idler photons and the shape of the joint spectral intensity, which importantly determines whether the heralded SPDC photons are pure [43, 101, 82].

Here we summarize two methods for measuring the JSI and single photon marginal spectrum. shown in Figure 2.9. One way is to detect the actual pairs of single photons produced from SPDC in order to characterize the sources, which is described in more detail in [6, 61, 103, 31]. However this method requires single photon detectors, which limits the speed and accuracy of the measurements. Another fairly new approach makes use of difference frequency generation (DFG) and has been shown to obtain faster and more accurate results. It has been the preferred method when characterising our source, and is discussed with more detail in Eckstein's paper [31].

2.2.4 Detecting single photons with DCF fiber

The JSI distribution can be measured by spectrally resolving single photon coincidence measurements [6, 61, 103]. A fiber spectrometer is used to reconstruct the JSI by collecting one photon pair at a time. The fiber spectrometer is a highly dispersive fiber that causes different spectral components to map to different arrival times due to chromatic group velocity dispersion (GVD). This causes different spectral components to map to different arrival times at the detectors, which are then recorded [8, 13, 102].

The method for this type of measurement is shown in Figure 2.8 and proceeds as follows. Pump pulses[3] are guided into a PPKTP waveguide and generate pairs of photons with orthogonal polarizations, via Type-II SPDC, that are then separated with a polarizing beamspliter (PBS). These photons are coupled into highly dispersive single mode fibers[4] and detected by the avalanche photo-diode (APD) detectors[5] [8, 13, 102]. The photon arrival times to the avalanche photodiodes APDs relative to the pump lasers electrical trigger pulse are recorded with a time-to-digital converter (TDC)[6]. Each data point in the joint spectral probability distribution is from a coincidence measurement between two APDs, which indicates the arrival of a pair of photons from the same triggered pulse. When enough photon pairs have been detected, the full JSI can be reconstructed.

However this method of obtaining the JSI comes with its limitations. It requires

[3] 250kHz from a mode-locked Coherent Mira Ti:Sapph+RegA 9000 at 775 nm, filtered to a 2nm spectral FWHM

[4] Corning PureFrom DCM Module for 1550 nm C-band dispersive -987ps/nm with 5.37 dB loss

[5] idQuantique id220 avalanche photo-diodes

[6] quTools quTau

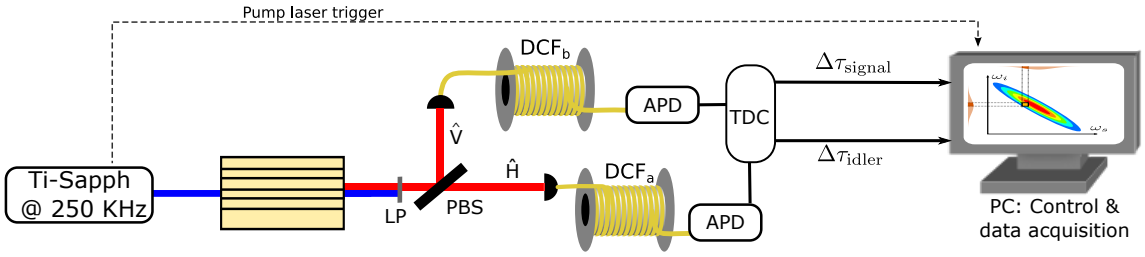


Figure 2.8: Layout of the experimental setup for SPDC-based spectral correlation measurements. Pump pulses are coupled into a PPKTP waveguide, which creates pairs of signal and idler photons via SPDC Type-II generation. The signal and idler photons are separated by a PBS and coupled into 10 km of dispersion compensating fibre (DCF) that causes the photons to have a certain delay depending on their frequency due to the high group velocity dispersion in the fibers. The arrival time of the photons at the avalanche photodiodes APDs relative to the pump lasers electrical trigger signal is recorded via a time-to-digital converter (TDC).

single photon detectors, which limits the measurement speed and accuracy. The speed of the measurement is affected by the single photon detector's deadtime $t_d = 10\mu s$, the detector's low efficiency Eff= 20%, and noisy background counts. The rate at which coincidences are detected is given by $R_s = R_p Eff_1 Eff_2$, where R_p is the pair production rate and Eff_1 and Eff_2 are the two systems' detection efficiencies, including loss from the source and the detector [31] (for example for a mean photon number of 0.2, a pump laser repetition rate of 100kHz, and 50% efficiency in both arms, we get $R_s = 0.2 * 100KHz * 0.5 * 0.5 = 5kHZ$. The pair production rate R_p is limited by the deadtime t_d because it must be less than $1/t_d$, otherwise the measurements will suffer from saturation effects. However lowering the coincidence count rate means that measurements must last for longer and are therefore more susceptible to drifts.

The other limitation is the accuracy of the spectral resolution which can be obtained from the ratio of photon-arrival uncertainty and fiber dispersion [31]. The photon-arrival uncertainty comes from the timing jitter of the electrical detection

signal from the APDs $\tau_{APD} = 250ps$ and from the mean temporal bin size of the quTools quTau TDC $\tau_{TDC} = 81ps$, which measures the photons' arrival times at the APDs relative to the pump laser's electrical trigger pulse. Therefore the total spectral resolution given by the fiber spectrometer is the joint temporal jitter of the APD and the TDC time resolution over DCF dispersion resulting in $\Delta\lambda_{SPDC} = \frac{\sqrt{\tau_{APD}^2+\tau_{TDC}^2}}{D_{DCF}} = 0.2$ nm.[31].

2.2.5 Stimulated emission tomography

2.3 Techniques to experimentally measure joint spectral intensity

Our preferred technique described in [69, 31] is to measure the JSI with stimulated emission tomography (SET). This stimulated process via difference frequency generation (DFG) is a faster and more precise process than waiting for coincidence counts as in the method above. The DFG process is considered the classical analog to SPDC because an injected seed beam stimulates the conversion of pump photons to signal and idler photons; whereas, for the SPDC process conversion is stimulated by vacuum fluctuations [47].

Both SPDC and DFG have the same phase-matching function [77, 18], so if they are given the same pumping scheme, then their JSI, which is the product of the phase-matching and pump function, is shown in Figure 2.10. In fact, the number of photon pairs produced from SPDC is proportional to the number of pairs emitted from the stimulated DFG process, with a proportionality constant approximately equal to the

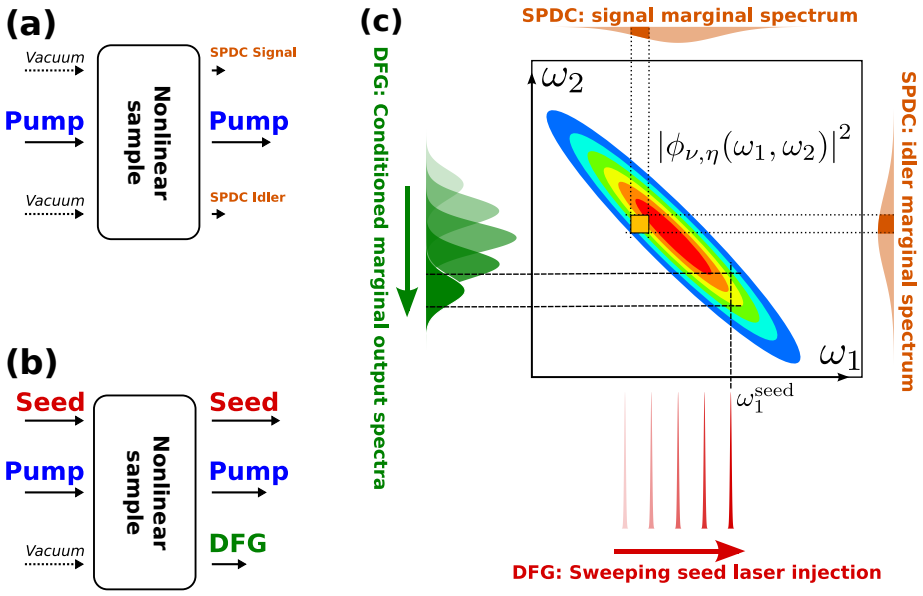


Figure 2.9: (a) A pump pulse interacting with a nonlinear crystal produces pairs of photons, labelled signal and idler, with a certain probability via SPDC. (b) When a coherent "seed beam, in the same mode of either the signal or idler photons, is coupled into the crystal with the same pumping scheme, it stimulates the conversion of pump photons into signal and idler pairs via DFG with an intensity proportional to the strength of the seed beam. (c) The joint spectral intensity for the same nonlinear crystal, pumped with the same configuration, can be measured by detecting the generated single photons from SPDC or the stimulated output from the DFG process, as shown. In the SPDC case, the emitted photons are sent to spectrometers and the wavelength intensities, for corresponding signal and idler photons, form pixels of the JSI as shown on the top and right axis of the graph. In the DFG case, a CW laser, swept through a range of wavelengths in either the signal or idler mode, acts as a "splice of the JSI. The full JSI is reconstructed by adding up the output spectrum for the respective stimulated output mode at each wavelength of the seed.

average number of photons in the stimulating seed [69]:

$$\frac{\langle n_{\omega_i} \rangle_{A_{\omega_i}}}{\langle n_{\omega_i} n_{\omega_s} \rangle} \approx |A_{\omega_1}|^2, \tag{2.21}$$

where $\langle n_{\omega_i} \rangle_{A_{\omega_i}}$ is the average number of signal photons with frequency ω_s stimulated by an idler seed with frequency ω_i, $\langle n_{\omega_i} n_{\omega_s} \rangle$ is the average number of photon pairs that would be generated in the spontaneous process, and $|A_{\omega_1}|^2$ is the average photon number within the coherence time of the seed. Therefore the correlations of

photon pairs generated by SPDC can be investigated through measurements of the corresponding classical DFG process, which in principle will provide a signal several orders of magnitude larger.

Since the output signal from DFG is several orders of magnitude larger in number than the output from SPDC, we can see the response on an optical spectrum analyzer (OSA)[7]. Therefore this measurement is helpful because it does not require single photon detectors and can occur with much shorter integration time and with more spectral resolution. By measuring the average number of stimulated idler photons, we perform a virtual tomography on the state that would be emitted by the corresponding spontaneous process.

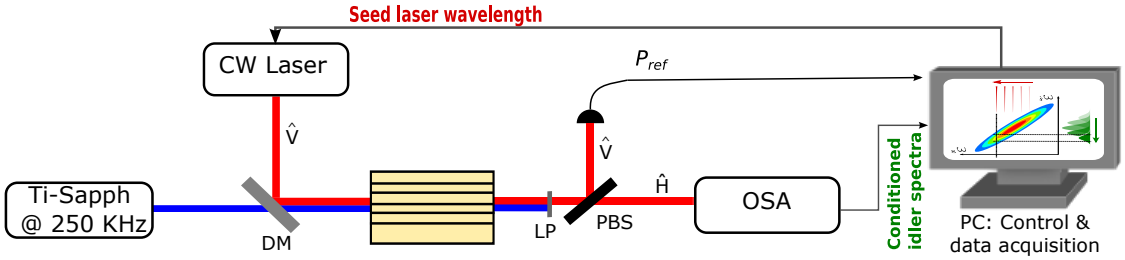


Figure 2.10: Layout of the experimental setup for stimulated emission tomography measurements. Additional CW laser light, in the V polarization of the signal mode, is added to the original pump scheme with a dichroic mirror and coupled into the PPKTP waveguide. The generated photons from DFG in the $\hat{H}$ polarized idler mode are separated from the $\hat{V}$ polarized signal mode and CW laser light by a beam-splitter and are sent to an optical spectrum analyzer. The spectrum of the idler light for a range of seed wavelengths are recorded to obtain the JSA.

To perform stimulated emission tomography with DFG, the same SPDC pump configuration as above, is coupled into a PPKTP waveguide but now with an additional seed beam from a CW laser[8]. Since the output signal produced from the DFG

[7]Yokogawa AQ6370D
[8]TUNICS T100S-HP: High-Power Tunable Lasers

process is proportional to the expected number of photon pairs from SPDC, we can reconstruct the JSI by varying the wavelength of the seed signal, shown in Figure 2.10.

When the CW seed beam is swept over the signal bandwidth of the spontaneous process with the same pumping condition for SPDC, the generated idler spectrum is collected and each of these "slices can be added up to give the JSI, as shown in Fig. 2.11. The spectral resolution is then determined by the accuracy of the seed

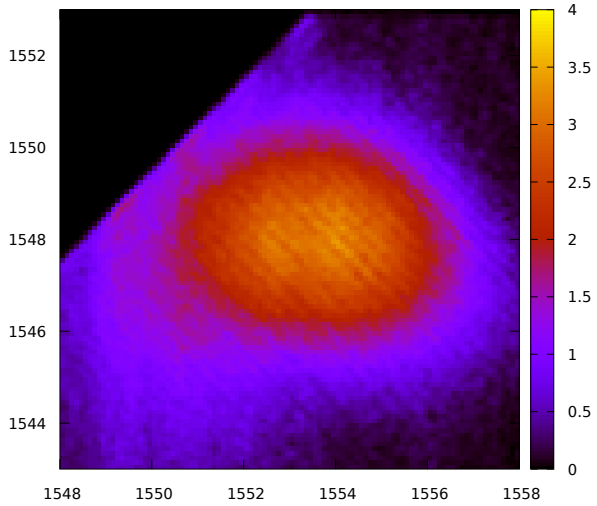


Figure 2.11: The experimental JSI acquired from stimulated DFG measurement (see Fig. 2.10). Since the signal and idler photons are centered around 1548 nm and 1554 nm respectively, the CW laser is set to sweep from 1538 nm to 1548 nm with 2mW of power and the OSA is set to measure the wavelengths from 1548nm to 1558 nm with 0.1nm resolution. The measurement is cutoff in the upper left corner so leak through of the seed CW light doesn't washout the stimulated signal. Diagonal stripes in the JSI with the seeding can explained due to reflections in the waveguide that causes a cavity effect.

laser wavelength (20 pm) along one axis and by the OSA resolution (20 pm) along the other. This means that the spectral resolution with this DFG stimulated method

is 10x more precise than spectrally resolving single photon coincidence measurements and realisable in a much shorter time [31]. The experimental JSI from our source is shown in Figure 2.11. It suggests that our source will be able to generate pure heralded photons.

Moreover from the JSI, we can compare the spectral overlap between idler photons from two different sources. From our measurements of the JSI, we define a matrix $\mathbf{M}$, which represents the mean spectral power for certain wavelengths of CW seed laser and corresponding binned OSA wavelengths such that each matrix element $\mathbf{M}_{m,n}$ represents the JSI where ω_s and ω_i are discretized frequency component of signal and idler respectively. The matrix elements of the columns are summed together to get the idler marginals distributions from each source. To calculate the overlap we take the inner product of the spectra, which in our experiment 99%, showing really high spectral indistinguishability.

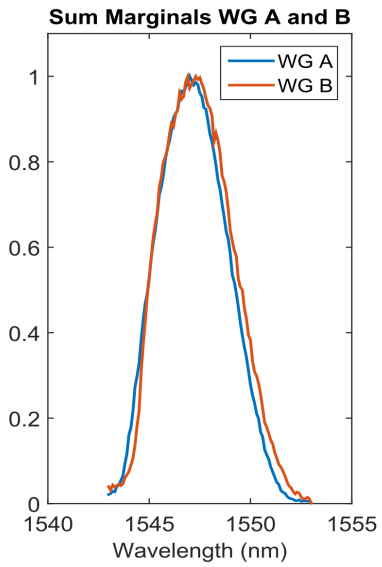


Figure 2.12: Marginal spectrum of idler photons from the two differrent waveguides with 99% overlap.

2.4 Summary

In this chapter we have discussed the theory behind the SPDC process. We saw how the process is governed by energy conservation and momentum conservation. This lead us to see how the joint spectral amplitude, $f(\omega_i, \omega_s)$, which describes the spectral distribution of the signal and idler photons, is affected by the pump envelope and phasematching function. It can be visualized by measuring the joint spectral intensity, $|f(\omega_i, \omega_s)|^2$, which we proceed to show via two different techniques, the preferred method being stimulated emission tomography. The resulting measurement shows promise that our sources are able to produce pure heralded photons. In the next chapter we will further investigate this.

Chapter 3

Further source characterization

In the previous chapter we looked at the joint spectral intensity (JSI) to determine possible spectral correlations. In order to attain the highest possible purity, spectral and phase correlations of each heralded photon need to be minimized. Although the JSI is a good visual, it neglects possible phase correlations. Therefore we show that it can only determine a lower bound for the effective number of entangled modes. If we want a more encompassing measurement that includes both spectral and phase correlations, we need to look at the output photon number statistics.

In this chapter we continue to characterize our source to determine if the generated heralded photons are indeed pure and indistinguishable. In this chapter, we begin with a mathematical tool called Schmidt decomposition. This allows us to describe the joint spectral amplitude in a useful way that helps us determine correlations from the effective number of correlated optical modes. We mathematically show that the SPDC process is equivalent to a superposition of two-mode squeezing operators acting on a vacuum state. This leads us to recognize how to distinguish, by using the marginal statistics, between the ideal case, when there is a single two-mode squeezing operator involved, versus the non-ideal case, when there are more than one two-mode

squeezing operator. We use the second order correlation function as a measure of the marginal photon statistics to help us quantify the degree of spectral and temporal correlations. The measurement we get from the second order correlation function coincides with the measurements we took with the JSI.

3.1 Schmidt decomposition

We use a mathematical tool called Schmidt decomposition [90] to decompose the joint spectral amplitude (which contains spectral and phase information) into orthonormal basis functions g_k and h_k [67]:

$$f(\omega_i, \omega_s) = \sum_k \sqrt{c_k} g_k(\omega_i) h_k(\omega_s) \qquad \text{and} \qquad \sum_k c_k = 1, \tag{3.1}$$

where each pair of modes is weighted by its Schmidt magnitude c_k, and ω_i and ω_s are the frequencies of the signal and idler photons. From the c_k distribution and from the concept of state factorization, we are able to evaluate what is known as the Schmidt number, K, from the relation [30, 44]:

$$K = \frac{1}{\Sigma_k c_k^2} \tag{3.2}$$

The physical meaning of the Schmidt number is useful because it counts the effective number of entangled optical modes present in the PDC state, shown in Figure 3.1. If there is just one mode then the Schmidt number equals one, K = 1; if there are more than one then the Schmidt number approaches zero.

By applying Equation (3.1) to the SPDC unitary from Equation (2.12), the ex-

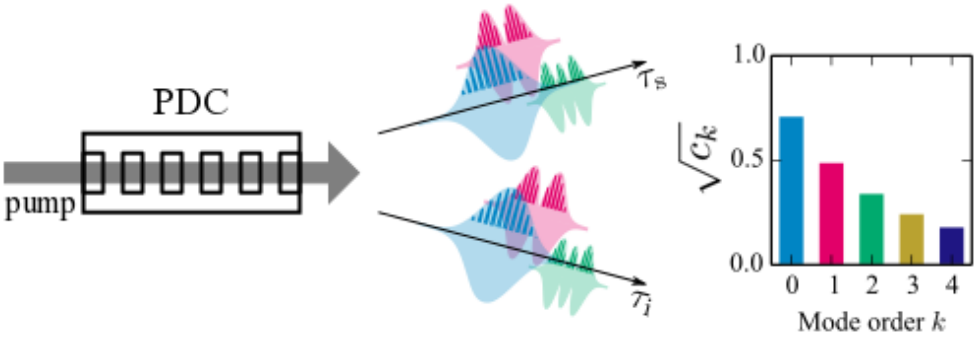


Figure 3.1: Here is a visual of the pump interacting with a non linear crystal in which independent pairs of pulses are produced via SPDC into a superposition of different ultrafast optical pulse modes, designated by the different colors (blue, pink, green). The graph to the right shows the relative weights given by the Schmidt coefficients c_k versus the mode order k on the x-axis [12].

pression is rewritten:

$$\hat{\mathrm{U}} = \exp\Bigg[\sum_k r_k \underbrace{\int_0^\infty d\omega_i g_k(\omega_i)\hat{a}_i^\dagger(\omega_i)}_{\hat{A}_k^\dagger} \underbrace{\int_0^\infty d\omega_s h_k(\omega_s)\hat{a}_s^\dagger(\omega_s)}_{\hat{B}_k^\dagger} + h.c.\Bigg], \tag{3.3}$$

where the two ω integrals for signal and idler become independent. As illustrated in Figure 3.2, new broadband mode creation operators, $\hat{A}^\dagger$ and $\hat{B}^\dagger$, represent a superposition of monochromatic creation operators, $\hat{a}_i^\dagger(\omega)_i$ and $\hat{a}_s^\dagger(\omega)_s$, weighted with the functions, g_k and h_k, from the Schmidt basis:

$$\hat{A}_k^\dagger := \int d\omega_{\mathrm{i}} g_k(\omega)\hat{a}_{\mathrm{i}}{}^\dagger(\omega) \quad \text{and} \quad \hat{B}_k^\dagger := \int d\omega_{\mathrm{s}} h_k(\omega)\hat{a}_{\mathrm{s}}{}^\dagger(\omega). \tag{3.4}$$

$\hat{A}^\dagger$ and $\hat{B}^\dagger$, are related to the broadband signal and idler modes respectively.

The spectral shapes of the broadband signal and idler modes, $\hat{A}^\dagger$ and $\hat{B}^\dagger$, are defined by the two-dimensional frequency representation of the joint spectral amplitude. In Figure 3.3, a superposition of broadband Schmidt modes indicates the presence of time-frequency correlations between the generated signal and idler. In the special

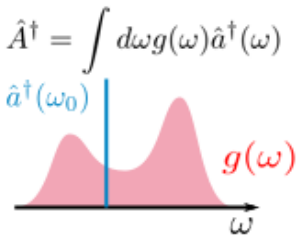


Figure 3.2: An illustration of the mode operators. $\hat{\alpha}^\dagger(\omega_o)$ creates a photon at the specific frequency ω_o, whereas $\hat{A}^\dagger$ creates a single photon into the broadband mode [12].

case when signal and idler have a Gaussian spectral distribution, the signal and idler broadband Schmidt modes are well approximated by Hermite-Gaussian functions.

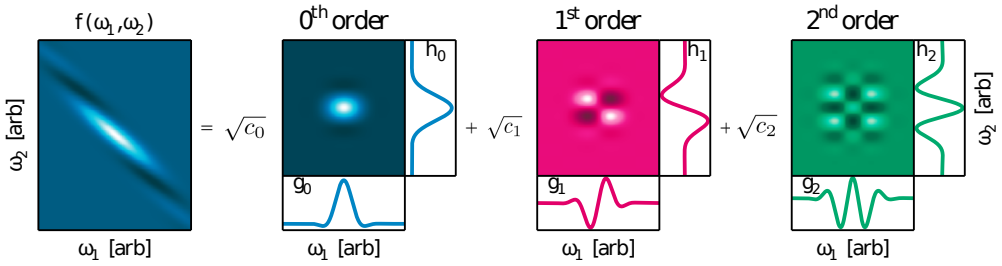
As a quick recap, from Equation 3.1 and 3.2, the JSA is written in terms of the Schmidt orthonormal basis and the Schmidt number K is defined, which takes into account both spectral and phase correlations.

3.1.1 Schmidt number lower bound from measured JSI

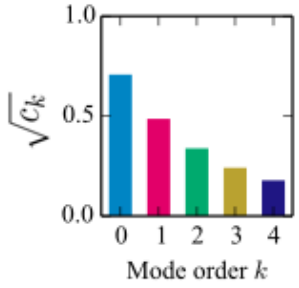
Before we take into account both phase and temporal correlations, let us take a look at the joint spectral intensity measured in Chapter 2 to determine a lower bound for the Schmidt number.

From our measurements of the JSI, Figure 2.11, we define a matrix $\mathbf{M}$, which represents the mean spectral power for certain wavelengths of the CW seed laser beam and corresponding binned OSA wavelengths such that each matrix element $\mathbf{M}_{s,i}$ represents a discretized frequency component of signal and idler respectively. This mean spectral power matrix $\mathbf{M}$, obtained by measuring the JSI, can then be used to measure the lower bound of the Schmidt number $K_{\min}$ [30, 31]:

$$\frac{1}{K_{\min}} \approx \frac{\mathrm{Tr}[(\mathbf{M}^\dagger\mathbf{M})^2]}{\mathrm{Tr}[\mathbf{M}^\dagger\mathbf{M}]^2}, \tag{3.5}$$



(a) Broadband Schmidt modes



(b) Weights of Schmidt coefficients

Figure 3.3: The frequency correlations between the signal and idler beams is shown by the tilt of the JSI, on the far left of figure (a). The degree of frequency correlations is closely connected with the number of different broadband Schmidt modes, which resemble Hermite functions, shown on the axes in (a). Figure (b) shows the relative weights given by the Schmidt coefficients c_k versus the mode order K on the x-axis [12].

Since the JSI does not include any phase or temporal information, from our experimental measurements we calculate the lower bound of the Schmidt number $K_{\min} = 1.06$ and for the second source we measure a Schmidt number of $K = 1.12$. Next we will see if this coincides with our measurement via marginal statistics.

3.1.2 Schmidt modes → Two-mode squeezing

Related to Figure 3.3, the time-integrated Hamiltonian in Equation (3.3) can then be expressed in terms of these broadband mode operators:

$$\hat{\mathrm{U}} = \exp\left[\sum_k (r_k \hat{A}_k^\dagger \hat{B}_k^\dagger - r_k^* \hat{A}_k \hat{B}_k)\right] \tag{3.6}$$

$$= \bigotimes_k \exp\left[(r_k \hat{A}_k^\dagger \hat{B}_k^\dagger - r_k^* \hat{A}_k \hat{B}_k)\right] \tag{3.7}$$

$$= \bigotimes_k \hat{S}_k(-r_k) \rightarrow \text{Two-mode Squeezing.} \tag{3.8}$$

These equations above are important because it shows that the state evolution due to type II SPDC is equivalent to an ensemble of independent two-mode squeezing operators, $\hat{S} = \exp\left(-\zeta \hat{A}^\dagger \hat{B}^\dagger + \zeta^* \hat{A}\hat{B}\right)$, applied to a vacuum state [67], illustrated in Figure 3.4, where $-\zeta$ parameterises the squeezing. The coefficient r_k is known as the squeezing parameter, and it's distribution determines the relative strength of all squeezers as well as spectral correlation between signal and idler beams. These coefficients depend on the fields spatial overlap, the pump amplitude, the phasematching, and the length of the crystal.

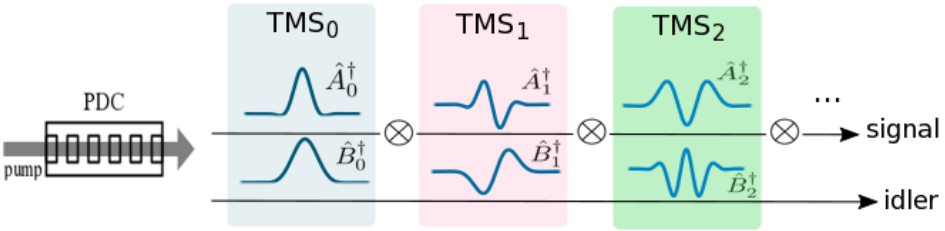


Figure 3.4: This figure illustrates how the SPDC unitary equals an ensemble of independent two-mode squeezers.

Now we want to ask what effect a superposition of two-mode squeezers has on our photon generated state, in particular if we have a state that is composed of multiple

squeezers what happens to the purity of the idler photon when we herald on the signal photon? The full output state for the two-photon state of the signal, s, and idler, i, photons can be expressed as the joint density matrix $\hat{\rho} = |\Psi\rangle\langle\Psi|$. The individual photon state for each signal and idler mode is obtained by taking a partial trace of $\hat{\rho}$ by integrating over the spectrum of the idler and vice versa:

$$\hat{\rho}_i = \mathrm{Tr}_s\hat{\rho} \qquad \hat{\rho}_s = \mathrm{Tr}_i\hat{\rho} \tag{3.9}$$

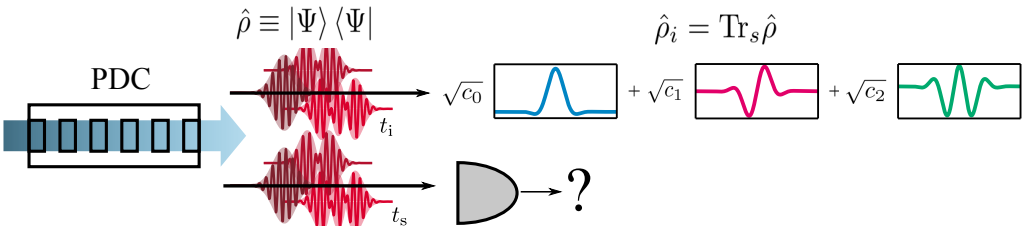
where Tr_s is the partial trace over the signal subsystem and Tr_i over the idler subsystem. Undesired entanglement between the signal and idler fields that can not be resolved with, for example, the detector on the signal arm will result in the collapse of the idler photon into a mixture of all possible Schmidt modes, as depicted in Figure 3.5(a). This issue can also be visualised with the two-dimensional frequency representation of the PDC state, Figure 3.5(b). It shows that a successful detection event of a PDC photon in the signal mode cannot reveal the central frequency of the corresponding idler. Hence, the idler photon inevitably collapses into a mixture of all possible frequency modes.

Mathematically the two-mode squeezing operator produces an output state that can be written as a superposition of photon number states, where $e^{i\phi}r$ is the complex squeezing parameter:

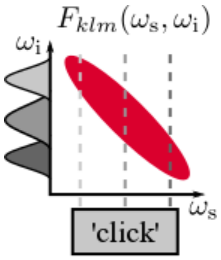
$$|\Psi\rangle = \hat{S}\,|0,0\rangle = \sqrt{1-\tanh(r)^2}\sum_{n=0}^{\infty}(-e^{i\phi}\tanh(r))^n\,|n,n\rangle\,. \tag{3.10}$$

In order to simplify Equation (3.10) let's define $\lambda = -e^{i\phi}\tanh(r)$:

$$|\Psi\rangle = \sqrt{1-|\lambda|^2}\sum_{n=0}^{\infty}\lambda^n\,|n,n\rangle\,, \tag{3.11}$$



(a) Fix



(b) JSA

Figure 3.5: The PDC pump (blue arrow) interacts with the nonlinear material inside the waveguide and creates a two-photon output state $\hat{\rho}$. When the signal arm is detected with detectors that can't resolve Schmidt modes, the idler state, represented by $\hat{\rho}_i$, collapses into a mixture of all possible Schmidt modes. The resulting figures representing $\hat{\rho}_i$ in the upper row is meant to show a resulting classical mixture. This can also be illustrated with the JSA. When the idler is detected, the heralded photon collapses into a mixture [12].

where λ is proportional to the pump beam energy and the strength of the crystal's nonlinearity $\chi^{(2)}$. Going back to Equation (3.9), the marginal state of either signal or idler mode from a single two-mode squeezer is:

$$\hat{\rho}_{s,i} = (1 - |\lambda|^2) \sum_n \lambda^{2n} |n_{s,i}\rangle \langle n_{s,i}| . \tag{3.12}$$

This shows that for a single two-mode source, the marginal distribution will be equivalent to a thermal number distribution $P_n = (1 - |\lambda|^2)\lambda^{2n}$. Therefore the marginal state from multiple squeezers will output N independent thermal distributions. Since our detectors cannot resolve Schmidt modes from multiple two-mode squeezers, the overall number statistics will be a convolution of the different thermal statistics of the individual modes, which approach Poissonian statistics for a large number of

two-mode squeezers [78, 4].

Now the question is how to use this information to measure the number of modes and have a way to infer the purity of the heralded photons. For this we will use a well-known measurement called the second order correlation function.

3.2 Correlation function and photon number statistics

From the marginal photon number statistics, we use the second order correlation function to allow us to differentiate between spectrally factorable and spectrally correlated. The unheralded second order correlation function [42], $g^{(2)}$, uses the statistics of intensity fluctuations in the electric field (or equivalently fluctuations in photon number) to discriminate between beams with thermal and Poissonian photon statistics [99]. In the weak interaction limit which is suitable for the low energy used for our sources, there is a useful connection between the $g^{(2)}$ correlation function, the effective mode number, K, and the heralded purity of the signal and idler modes, $\mathcal{P}_{s,i}$ [32, 22, 93]:

$$g^{(2)}(0) \approx 1 + \frac{1}{K} \approx 1 + \mathcal{P}_{s,i} \tag{3.13}$$

A $g^{(2)}$ measurement when combined with the knowledge of Equation (3.1), gives us the effective number of modes under the assumption that all squeezed states share an identical amount of squeezing [22]. It should be noted that the $g^{(2)}$ measurement does not give access to the exact distribution of squeezers. However we see that in the ideal limit of a perfectly factorable source that involves only a single Schmidt mode, $K = 1$ from Equation (3.1), then the heralded single photon purities of $\mathcal{P}_{i,s} = 1$

and the photon statistics of a single mode as discussed will be thermal leading to $g^{(2)}(0) = 2$. In the other limit of a mixed heralded state with many Schmidt modes, $K \to \infty$ from Equation (3.1), $\mathcal{P} = 0$, which results in a Poissonian distribution with corresponding $g^{(2)}(0) = 1$. In this case, the detector can not distinguish between the different thermal distributions so it sees a convolution of all of them [78, 5].

3.2.1 Experiment

The unheralded second order correlation $g^{(2)}$ measurement is a convenient and loss tolerant way to experimentally confirm the purity of the heralded photons [5, 94]. With non-number resolving (click) detectors, the degree of second order coherence of the heralded beam can be measured with a setup referred to as a Hanbury-BrownTwiss interferometer [14]. The output pairs from the SPDC source are split with a wollaston prism[1]; the signal (idler) is ignored/discarded, whereas the idler (signal) is sent to a non-polarizing beam-splitter (in this case a 50:50 single mode fibre coupler). Then the idler (signal) photon fields are split into two equal parts and sent to separate detectors to measure the number statistics on each output, shown in Figure 3.6.

The classical definition of the second order coherence is [72]:

$$g^{(2)}(\tau) = \frac{\left\langle \bar{I}(t)\bar{I}(t+\tau)\right\rangle}{\left\langle \bar{I}(t)\right\rangle^2} = \frac{\langle E^*(t)E^*(t+\tau)E(t+\tau)E(t)\rangle}{\langle E^*(t)E(t)\rangle^2}, \tag{3.14}$$

where $I(t)$ is the averaged intensity at time t and angle brackets denote a statistical average over a time longer than the coherence time. The second order correlation function is therefore a measure of the normalized level of intensity correlation for the same beam at times separated by τ. For low powers far from detector saturation,

[1]The wollaston prism acts like a polarizing beam-splitter.

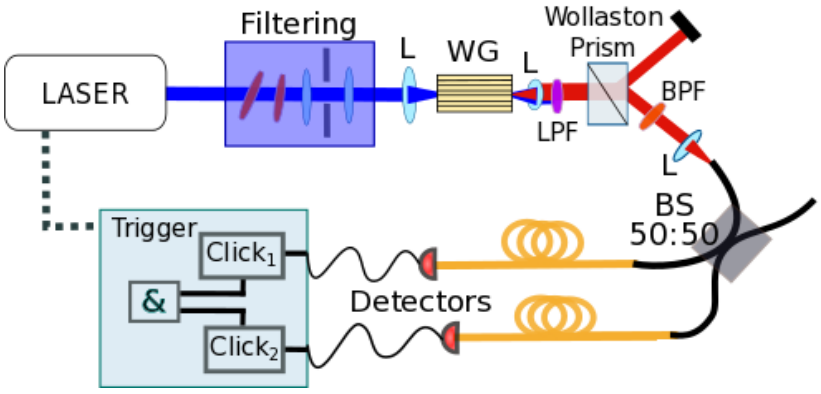


Figure 3.6: Layout of the experimental setup for unheralded $g^{(2)}$ measurement. Ultrafast pump pulses at 775 nm are filtered (full details in the Chapter 1) before theyre coupled into a PPKTP waveguide (wg) to create pairs of signal and idler photons via type II SPDC. After the waveguide, the pump is filtered out with a long pass filter (LPF), the signal and idler are separated by a wollaston prism, and the idler beam is discarded. The signal beam is cleaned up with a 8 nm FWHM bandpass filter (BPF) and then split by a 50/50 beam-splitter. The output modes are fed into APDs and the single, coincidence and trigger event rates are recorded.

rather than intensity measurements, one finds:

$$g^{(2)} = \frac{\langle \hat{n}_1 \hat{n}_2 \rangle}{\langle \hat{n}_1 \rangle \langle \hat{n}_2 \rangle} = \frac{N_{12} N_t}{N_1 N_2}; \tag{3.15}$$

where the mean number of photons at either output is equivalent to the ratio of detected photons to the number of triggers N_t, in this case the number of pump pulses. For example, the mean number of simultaneous photon events on both outputs is given by $\langle \hat{n}_1 \hat{n}_2 \rangle = N_{12}/N_t$ where N_{12} is the total number of times both detectors register coincident events with a click.

Since frequency correlations between signal and idler beam and thus the number of squeezed modes can be controlled by adjusting the spectral width of the PDC pump beam, we see experimental results in Figure 3.7 that show a maximum $g^{(2)}$ value of 1.91 ± 0.04 at 1.8 nm pump FWHM, in accordance with the simulations in chapter 2 Figure 2.7. When we move away from the optimal pump width, we see that the $g^{(2)}$

value decreases as expected.

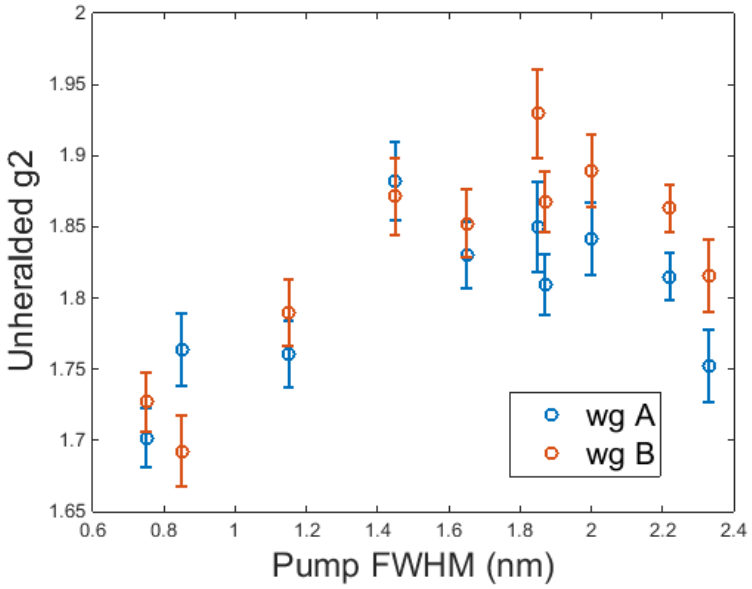


Figure 3.7: For different pump bandwidths, the unheralded $g^{(2)}$ was measured as the schematic shows in Figure 3.6. Since the pump bandwidths are adjusted with two bandpass filters, we were limited in the range of pump bandwidths that we could measure.

Looking back at Equation 3.13, this implies that our source corresponds to an effective mode number of $K = 1.1$, which coincides with the lower bound measured from the JSA in section 3.1.1 above. This shows that we have a close to perfect two-mode character of our PDC squeezing source. The waveguide nature of the source helps ensure the signal and idler occupy a single waveguide mode.

In this chapter, we have discussed decomposing the JSA, which contains the spectral and phase correlations, in terms of Schmidt modes. This helps us identify how many entangled modes our output state contains. We also discussed how we can view the parametric downconversion process as an ensemble of two-mode squeezing operators (in the ideal case a single two-mode squeezing operator is involved). This

lead us to the realization that we can use the marginal statistics to help us determine the purity of the heralded photons. We found from the JSI that the lower bound for our periodically poled KTP waveguide sources was $K_{min} = 1.06$. We then verified with a measurement of the second order correlation function that was indeed a lower bound and that by taking in phase correlations as well we found a more accurate Schmidt value $K = 1.1 \pm .05$. This is an indication that our source produces nearly pure heralded photons in the telecom wavelength regime. In the next chapter we are going to use photon number resolving detectors to more accurately characterize the source.

Chapter 4

Joint photon statistics and heralding photon number states

4.1 Introduction

With each chapter, we begin to understand our source with a greater level of detail. In Chapter 2, we explored spectral correlations with the joint spectral intensity. In Chapter 3, we began to look at the phase and spectral correlations and better understand our source as an ensemble of two-mode squeezers and conclude that our sources do indeed produce close to perfectly pure heralded photons. In this chapter, we further our investigation by exploring other possible sources of noise by integrating our source with state of the art photon-number resolving detectors. This allows us to characterize our source with a greater level of detail using just photon statistics. We then show that photon counting detectors can improve the single-photon nature of the heralded source. Finally we show that we can herald higher photon number states - a necessity when pushing the limits of our research capabilities.

We start the chapter by describing the types of detectors that were used in this thesis - click detectors and photon-number resolving detectors - and then discuss more

specifically the benefits and disadvantages of single photon avalanche click detectors and transition edge sensor photon-number resolving detectors. We show how to model photodetection by starting with the ideal basic model and then subsequently factor in loss to make the model more realistic and more appropriate to describe our situation. This helps us better understand how our experiments are limited by the type of detectors, detector efficiency and loss. It becomes clear that photon number resolving detectors increase the measurement capabilities that we have at our disposal, such as being able to explore a full reconstruction of the statistics of the fields involved in the generated SPDC output state. We use the photon number resolving detectors to investigate the photon number statistics, shown in Figure 4.1. This allows us to measure the marginal probability and joint probability distributions of our source to further characterize our source. We can then investigate the type of main fields involved and what the strengths of their contributions are.

We use this new model to fit our simulation to the unheralded and heralded correlation function. We are particularly interested in the fact that the heralded correlation function can be used to quantify the fidelity of an $n-$photon state and help us determine how well our source works as a single photon source. It is important to quantify multi-photon contamination and loss, both of which can introduce errors in linear optical quantum circuits. We conclude from our reconstruction that our source is nearly a single-mode source, with very high brightness and that we have the ability to herald larger photon number states.

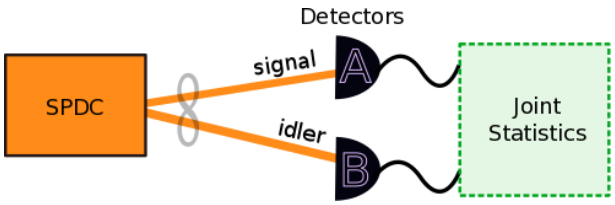


Figure 4.1: Here is the simplest model of our spontaneous parametric downconversion source, which creates pairs of photons, signal and idler. The detected events provide us with the joint statistics for us to analyze. In this chapter we will understand with more detail the breakdown of the fields generated from the SPDC process (i.e. understand with more detail what is coming from the orange SPDC box).

4.2 Detection

In this section, we discuss the operating principles and the pros and cons of click detectors (in particular InGaAs single photon avalanche detectors, SPADs) and photon number resolving transition edge sensors. Then a quick overview of the measurement theory is followed by a mathematical model for loss and the experimental measurements (Klyshko measurements) used to determine the overall loss in our system [63].

4.2.1 Operating principle

Photodetectors are devices that provide a macroscopic signal when a photon is absorbed. There are two types of detectors that are used for our experiments: click detectors and photon-number resolving detectors. click detectors can only indicate if there are no photons or more than one photon present, so heralding on a measured click eliminates the vacuum component, but forces the idler mode to contain a mixture of photon numbers that can not be resolved. Photon number resolving detectors (PNRDs) on the other hand can determine how many photons are present and come with the additional benefit of less noise and better efficiency than the conventional

APDs.

4.2.1.1 Click detectors (in particular InGaAs SPADs)

Single photon avalanche detectors (SPADs) are semiconductor-based devices that use the photoelectric effect to convert photons into electrons, which creates a macroscopic signal we can measure [33]. When an incoming photon hits the detector with an energy greater than the bandgap of the semiconducting material, it promotes an electron to the conduction band, which leaves a positive hole in the valence band. This creates a potential difference that is amplified by a power-supplied reverse voltage bias. Electrons and holes accelerate to the positive and negative ends respectively, shown in Figure 4.2, causing even more electrons to transfer from the valence band to the conduction band, which induces a selfsustaining avalanche effect as electron-hole pairs are exponentially created. From this avalanche effect, a macroscopic current is converted into a macroscopic voltage signal with a resistor, which is then emitted from the APD and can be detected as a voltage pulse from the detector, which is then registered as a "click" with conventional devices such as oscilloscopes or time-to-digital converters.

4.2.1.2 Superconducting transition edge sensor

A superconducting transition edge sensor (TES) is a much more precise device than the SPAD described above because it uses the change in resistance that occurs at the superconducting to normal-conducting transition. It requires ultracold temperatures, which makes the device more complicated to operate but provides photon number resolution and higher efficiency.

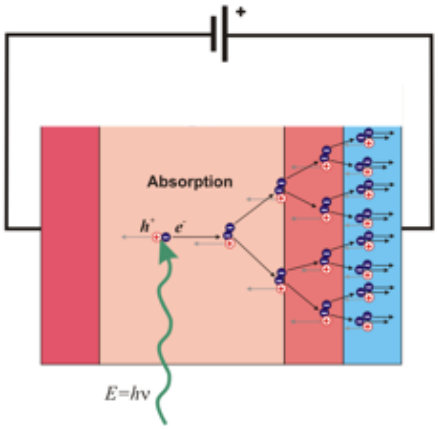


Figure 4.2: Simple schematic of single photon avalanche detector (SPAD). When a photon with energy $E = h\nu$ is absorbed by the semiconductor material of the SPAD, it creates an electron-hole pair. The voltage bias applied to the material causes the electrons and holes to accelerate to the positive and negative ends respectively. An avalanche effect occurs as more and more electron-hole pairs are produced and as a result a macroscopic current is produced, which allows us to know a photon has been detected.

How it works: A TES, consisting of a thin superconducting film deposited on an insulating substrate, is cooled below the critical temperature of the superconducting film. A small voltage is applied across the film, so it is biased at the edge of the superconducting-to-normal transition. Any incident photons that are absorbed in the superconducting film will cause the temperature to rise by an amount proportional to the amount of electromagnetic energy deposited in the detector. A small change in temperature (ΔT) results in an abrupt change in the material's resistance (ΔR) and thus a change in the measurable bias current, shown in Figure 4.3(a). The working point is selected such that the first photon, and the second photon, etc will increase the resistance by the same amount. Therefore the number of absorbed photons is proportional to the measured resistivity until too many photons are absorbed and the transition edge is saturated.

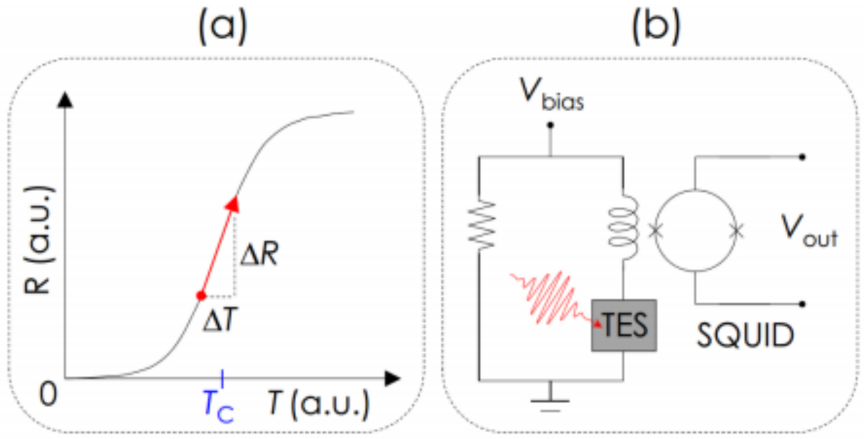


Figure 4.3: Figure (a) shows the resistance-temperature characteristics of a TES. When the TES is biased, an incident photon causes a small change in temperature (ΔT), which results in a large change in the material's resistance (ΔR). Figure (b) shows how the TES is held at a voltage bias by placing it in parallel with a bias resistor. The change in the resistance in the TES causes a change in the current. The inductor in series with the resistor converts generates a magnetic field that permeates the SQUID and is converted to an output voltage, which is then amplified and filtered.

Readout: As shown in Fig. 4.3(b), a superconducting quantum-interference device (SQUID) array is coupled to the TES and used to amplify the small change in the current for readout. The readout signal is a time-dependent voltage, V_{out}, that is proportional to the absorbed photon energy, shown in Figure 4.4. Each incoming trace, for n number of photons, can be described as a vector $\vec{V}_n(t)$, and it is assumed that if no photons enter the detector, the mean response is some baseline voltage that is defined to be 0, $\vec{V}_0(t) = 0$.

From these raw voltage traces, we need to infer the number of photons that have been detected. We reduce the large dimensional raw data set, to a single number specifying the relative energy of the absorbed pulse, by using a convenient method which computes the overlap (inner product) between each signal trace and a template

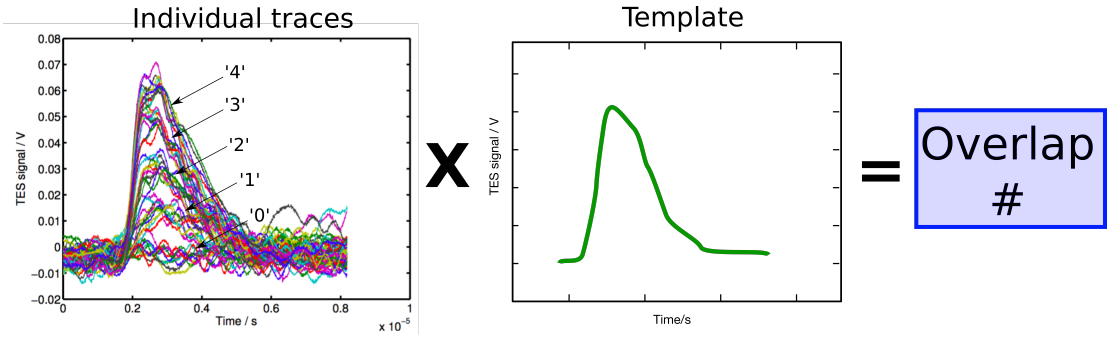


Figure 4.4: The figure to the far left shows the typical voltage traces that come from the detector. Here are 150 individual traces that have been plotted to the response of the detector. Despite the high frequency noise, it is possible to see the different levels which indicate different photon numbers hitting the detectors. The center figure illustrates the template trace, which is an average of all the multiple traces together. The one template trace is used to take the inner product for all the individual traces, which gives an associated overlap number. This one resulting number is much easier to deal with then the full vector of each individual trace.

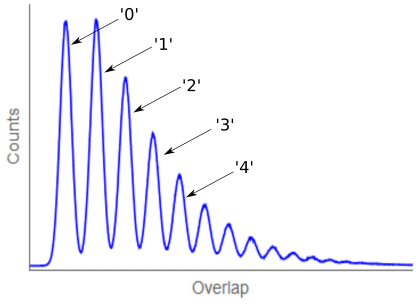


Figure 4.5: In this figure the histogram of the overlap integrals are plotted. Since the traces are grouped based on photon number, the resulting histogram is not a continuous distribution of overlap numbers. It is evident to see the binning due to the different TES photon numbers, labelled above each peak.

waveform [68]. A template is formed by averaging all of the waveforms:

$$\hat{V}_{\langle n \rangle}(t) = \frac{1}{M} \sum_{i=1}^{M} V_i(t), \tag{4.1}$$

where M is the total number of waveforms taken at the average photon number $\langle n \rangle$. The inner product between each waveform and this template yields an overlap which is proportional to the photon energy.

Figure 4.5 shows the experimental results from measuring the SPDC output. The overlap values are plotted in a histogram on a log and linear scale, revealing specific photon-number peaks. Under the assumption of white noise, we appropriately fit each of these peaks to a Gaussian distributions, which leads us to a reasonable fit to our data [68]. We can then assign photon numbers to the detector responses.

4.2.2 Caveats when using these detectors

We compare some of the current photon detector technologies in a table in Figure 4.6. We are most interested in the success rate of an experiment, where the success rate involving the detection of N photons scales as $P_{success} \approx R \cdot \eta^N$, where R is the measurement rate and η is the efficiency. Evidently from this relationship, the detection efficiency - the probability that we record a count given that a photon arrives at the detector - is the most important parameter for scalability because it scales exponentially. The measurement rate, which scales linearly, is limited by factors such as deadtime and jitter. Deadtime is the time immediately after a detection event that the detector can not register photon events (for APDs this deadtime, when it can not register photon events, is because the avalanche process needs time to be stopped by actively reversing the potential across the semiconductor, and for TESs the deadtime

Type of Detector	Wavelength Range	Max Efficiency	T (K)	Dark count rate (s^{-1})	Dead time	Jitter (ns)	Photon # resolving
Si SPAD	400-1100 nm	65% @810nm	300	20-5000	50 ns	< 1	x
InGaA SPAD	1000-1700 nm	12-20% @1550nm	230	20-5000	10 μs	<1	x
TES	Visible, Near IR	>98% @1550nm	0.1	<1	1 μs	< 4	✓
Nano-wire	Visible, Near IR	>93% @ 550nm	1	<1	40 ns	0.1	✓

Figure 4.6: A table comparing some of the current photon detector technologies [70, 25, 7, 80, 57]. For our experiments, InGaAs SPADs (from the company ID Quantique) and TESas (from the group of Sae Woo Nam at NIST) were used to detect the photons generated at telecom wavelengths. It is useful to compare InGaAs to silicon SPADs because it shows that silicon detectors are way more efficient at certain wavelengths but ineffective at 1550 nm, hence we were limited to 20% efficient InGaAs detectors. Superconducting nanowire single-photon detectors are also included in this table because they are very promising and were set up in our group towards the later half of my PhD. Even though superconducting nanowire detectors are technically click detectors, their high detection efficiency and speed make them very effective and possible to be multiplexed for photon number resolution.

is so the detector can be cooled back down to the necessary temperature). Jitter, mainly due to thermal noise, limits the rate of experimental events as a result of detector-timing noise. Dark counts and afterpulsing are potential sources of noise to be aware of, which happen when one or more spurious detector clicks follow an actual detection event. They can cause errors when assigning the correct photon number to a measurement.

Click detectors are limited because experimental power needs to stay inefficiently low to reduce the number of higher order events getting clumped together as a click signal with single photon events. Although limited, in general most quantum optics experiments have been compelled to perform with click detector. Silicon SPADs exist with 60% detection efficiency but they do not work at telecom wavelengths. InGaAs APDs work at telecom wavelengths but they are only 20% efficient and have high dark counts and long dead times, hence most experiments were compelled to stay in the wavelength ranges of silicon SPADs (400-900nm). Even if operating under ideal conditions of reflectance, crystal structure and internal resistance, a high quality silicon SPAD of optimum design would be capable of approaching an efficiency of 80%.

The recent development of superconducting detectors, which have low noise and are highly efficient at 1550nm, has opened the door for future more complicated quantum experiments at telecom. TESs benefit from having very low dark count rates in comparison to SPADs [71, 52]. The quantum efficiency of TESs' can be made even higher, by increasing the thickness of the superconducting material so almost all the incident photons are absorbed. However, thicker material means that it will

take longer for the material to cool down again to the initial temperature and the dead time is elongated (in the scale of μs), which means TES experiments require low repitition rates. TESs are in general relatively slow detectors (the speed of TES detectors is imposed by the maximum bandwidth of SQUID electronics, which have a maximum count rate of 1 MHz). TESs have a longer deadtime than SPADs since TESs have to cool back down to superconducting transition temperature after each measurement. TESs also experience large jitter due to the slow thermal process. All in all, the TESs slower detection rate but does not fundamentally affect the scalability of the system; their high efficiency more than makes up for it. We compare the most relevant detectors in the Table in Figure 4.6.

4.2.2.1 TES response

Besides loss and detector efficiency, we are also interested in the detector's accuracy in assigning the correct photon number to the measured state. Limitations can occur

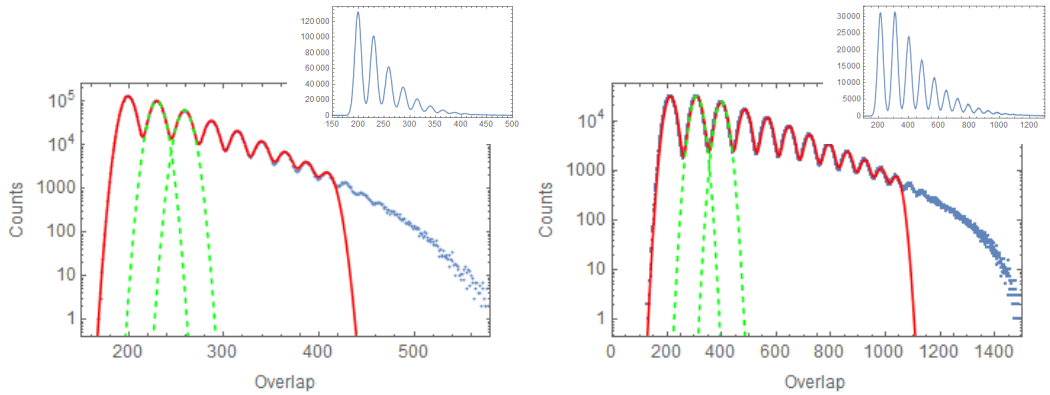


Figure 4.7: Figures (a) and (b) show the voltage pulse overlap values for the TESs we use, TES A and B respectively. The vertical axes in the main graphs are numbers of counts shown in log scale, while those in the insets are in linear scale. Every peak in each distribution was clearly separated, and was fitted with a Gaussian function in order to determine clicks for calculating photon-number probabilities.

in the regions where Gaussian fits overlap, shown in Figure 4.7, which causes photon numbers to be inaccurately assigned to the detected states.

From the detector response fit, we want the probability of wrongly assigning 'm' photons when there were in fact 'n':

$$P_d(m|n) = \int_{m_0}^{m_1} dx g_n(x), \tag{4.2}$$

where $g_n(x)$ represent the sample model functional form of the gaussian output response. The typical probability of false identification of photon numbers was roughly 0.4% for lower photon numbers and 2% for higher photon numbers. However from our simulations we were able to conclude that for our detector responses, the potential for inaccurately assigning the right photon numbers was not an issue and did not show any change in our model.

4.2.3 Photodetection theory

Now that we have described the detection apparatuses, let us continue by discussing the measurement theory for both click and photon number resolving detectors. This is necessary when we want to simulate our experimental data and further understand our source.

4.2.3.1 Simple mathematical model for perfect detectors

When simulating our experiment, we need to determine the most fitting positive operator value measure (POVM) as a general way to describe our measurement. Once the POVM, $\hat{M}$, is known, the probability distribution for the detector outcome

n, given by an input state ρ, is determined by the Born rule:

$$\text{Prob}_n = \text{Tr}[\hat{\rho}\hat{\text{M}}_n]. \tag{4.3}$$

POVMs on a physical system are used to describe the effect of a projective measurements performed on a larger system. For a perfect photon number resolving detector, the associated POVM is modelled as:

$$\hat{M}_n = |n\rangle \langle n| \tag{4.4}$$

where the photon number resolving measurement operator, $\hat{M}_n$ for every possible detection outcome (n), is a projection operator on the n-photon Fock state with the completeness relation $\sum_n \hat{M}_n = \mathbf{I}$. Following Born's Rule from Equation (4.3), the probability of recording n photons with a PNRD given an input state $\hat{\rho}$ is:

$$\text{Prob}_n = \text{Tr}[\hat{\rho}\hat{\text{M}}_n] = \langle n| \hat{\rho} |n\rangle , \tag{4.5}$$

where the probabilities are Hermitian and have to add up to one: $\sum_n^{\infty} \text{Prob}_n = 1$.

For ideal click detectors, the POVMs are modelled as:

$$\hat{\text{M}}_{\text{no click}} = |0\rangle \langle 0| \tag{4.6}$$

$$\hat{\text{M}}_{\text{click}} = 1 - |0\rangle \langle 0| = \sum_{n=1}^{\infty} |n\rangle \langle n| \tag{4.7}$$

where the 'no click' measurement operator, $\hat{\text{M}}_{\text{no click}}$, is a projection on the zero photon Fock state and the 'click' measurement operator, $\hat{\text{M}}_{\text{click}}$, is a projection on the sum of all possible Fock states minus the vacuum state, so that $\hat{\text{M}}_{\text{no click}} + \hat{\text{M}}_{\text{click}} = \mathbf{I}$. The probability of recording a detector 'no click' or click measurement, given an input

state $\hat{\rho}$, is given by:

$$\text{Prob}_{\text{no click}} = \text{Tr}[\hat{\rho}\hat{\text{M}}_{\text{no click}}] = \langle 0|\,\hat{\rho}\,|0\rangle \tag{4.8}$$

$$\text{Prob}_{\text{click}} = \text{Tr}[\hat{\rho}\hat{\text{M}}_{\text{click}}] = \sum_{n=1}^{\infty} \langle n|\,\hat{\rho}\,|n\rangle \tag{4.9}$$

where the probabilities of outcomes click and no click are Hermitian and have to add up to one: $\text{Prob}_{\text{no click}} + \text{Prob}_{\text{click}} = 1$.

However described above are ideal models for click and photon number resolving detectors when every photon is detected and converted to a signal. Let's look at how we would model loss and detector efficiency to make the model more realistic for both these types of detectors in the next section.

4.2.3.2 Including loss theory

It is important to be aware of the losses in the system because they degrade the precision of a measured value. Losses also include the inability for detectors to absorb and convert light into an electrical signal. To account for these effects, a global collection efficiency η is introduced on each of the arms. The probability to register an n-photon event, compared to the lossless case as we noted before, scales roughly as η^n.

The standard beam-splitter model is used to analyze linear optical losses in our setup, shown in Figure 4.8. For detectors, if k photons enter a beam-splitter, the probability for n photons being transmitted is given by the binomial distribution:

$$\hat{\text{L}}_{k,n}(\eta) = \binom{n}{k}(1-\eta)^{n-k}\eta^k, \tag{4.10}$$

where the beam-splitter transmission, η, imitates the probability that a photon sur-

vives loss. The photon number resolving measurement operator with loss is then:

$$\hat{\mathrm{M}}_k = \sum_n \hat{\mathrm{L}}_{k,n}(\eta) \left|n\right\rangle \left\langle n\right| . \tag{4.11}$$

which gives the probability of having k photons from n after a loss of $1-\eta$.

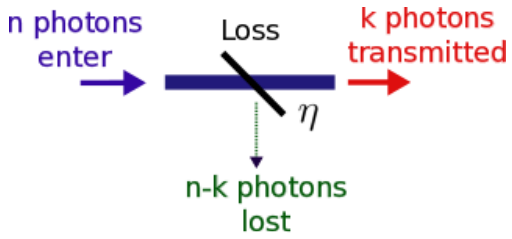


Figure 4.8: We model loss with a beam-splitter. If we begin with n photons and the arm has η efficiency then its similar to a beam-splitter with η transmission where n pass and $n-k$ are reflected.

For click detectors the measurement operators with loss are:

$$\hat{\mathrm{M}}_{\text{no click}} = \sum_{n=0}^{\infty} (1-\eta)^n \left|n\right\rangle \left\langle n\right| \tag{4.12}$$

$$\hat{\mathrm{M}}_{\text{click}} = \sum_{n=0}^{\infty} [1-(1-\eta)^n] \left|n\right\rangle \left\langle n\right| . \tag{4.13}$$

The measurement probability to detect vacuum state with less than 100% efficiency, or in other words the probability to reflect all n photons at the beam-splitter, is $(1-\eta)^n$. The measurement operator to detect a "click", any state with one or more photons, with detectors that are less than 100% efficient is $(1-(1-\eta)^n)$. Experimentally one way to measure this loss is with Klyshko efficiency measurements to be discussed in the next section.

4.2.3.3 Measuring Loss - Klyshko Efficiency

Klyshko efficiency measurements [62, 63, 2] are a standard way to characterize loss in a PDC setup by measuring the statistical character of light rather than its brightness.

Since SPDC creates states perfectly correlated in photon number, the detection of the signal without the simultaneous detection of the idler photon can only be caused by loss or detector inefficiency in the idler arm. The Klyshko measurements gives us the probability that given that the first photon of the same pair was detected in the first arm, the second photon of a photon pair is subsequently detected in the second arm. Coincidences and single-click probabilities are recorded, depicted in Figure 4.9, in the low-pump-power regime when the resulting mean photon number is much smaller than one. The probabilities for single clicks are:

$$\text{Prob}_s = \text{Prob}_{\text{PDC}} \cdot \eta_s \tag{4.14}$$

$$\text{Prob}_i = \text{Prob}_{\text{PDC}} \cdot \eta_i, \tag{4.15}$$

where η_s and η_i are the probabilities for a single photon to make it to the detector and produce a click. The probability to measure a photon pair is then:

$$\text{Prob}_{coinc} = \text{Prob}_{\text{PDC}} * \eta_s * \eta_i. \tag{4.16}$$

The efficiencies on the signal and idler arm can be calculated as such:

$$\eta_s = \frac{\text{Prob}_{coinc}}{\text{Prob}_i} \quad \text{and} \quad \eta_i = \frac{\text{Prob}_{coinc}}{\text{Prob}_s}, \tag{4.17}$$

and the setup for such measurements is Figure 4.9. The results, revealing 50% efficiency in arm A and 36% efficiency in arm B, are shown in Figure 4.10. These measurements were taken with TES detectors but results are binned as though they were taken from click detectors (all measurements with more than one photon are regarded as a click).

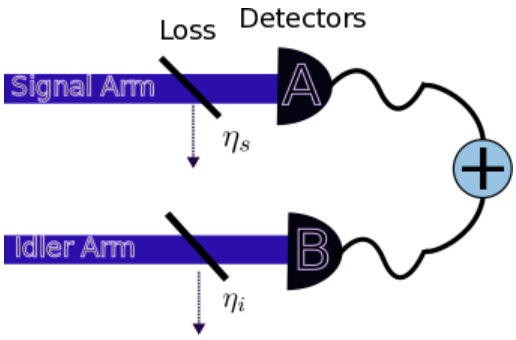


Figure 4.9: Klyshko measurements are performed by taking the ratio of the probability of coincidence to singles described more in text.

However Klyshko measurements are limited in a couple of ways. First, they rely on the assumption that only one photon pair is emitted at a time, which forces us to measure at low pump powers so higher order photons do not contaminate our measurement. We then assume that the efficiency, $\eta_{s,i}$, depends linearly with pump power and extrapolate the curve to zero power to yield the rough value of the overall efficiency. However, this means the detector is now calibrated outside the power regime that we tend to use it in. Secondly, background photons, which do not come in pairs increase the single counts and therefore reduce the calculated efficiencies. Thirdly, the Klyshko scheme is primarily designed to measure loss using single-photon detectors and does not directly translate to PNRDs. We will resolve this issue in section 4.3.3 with another method using photon number resolving detectors and marginal and joint probability distributions.

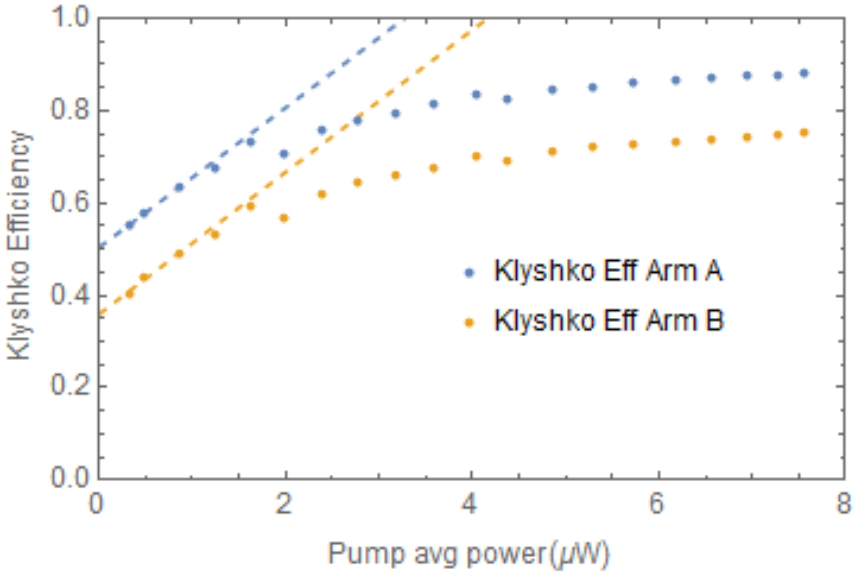


Figure 4.10: A plot for the Klyshko efficiencies measured. The error bars from the lower powers go from 0.0018 to 0.0010 at higher powers (smaller than the data points plotted). To reduce optical losses, we use Anti-Reflection (AR) coatings on all optical surfaces (filters and fibers) and we minimize the number of optical components.

4.3 Photon-number statistics measurements

4.3.1 Theory of different field contributions

In Chapter 3, we discussed how the SPDC process could be thought of as an ensemble of two-mode squeezers (in the ideal case, just one squeezer for maximum heralded purity). But now we want to explore further to see if there are additional uncorrelated thermal and Poissonian fields in each arm of our source and if so, determine their strengths.

From the very simple model of parametric downconversion, shown in Figure 4.1, which describes a source producing two output states, signal and idler, we now want to investigate this process with greater detail and determine all the possible contributions. The question is: from the photon-number statistics that we measure with

TESs, is it possible to determine the various fields in each arm, their strength and determine the overall losses? Answer: Yes with the statistics measured, the mode structure can be reconstructed from the photon-number-resolved marginal and joint probability distribution (JPD) as we will show in the rest of this chapter [15]. The method we used helps reveals the type of unwanted light that is mixed in with our signal [15]. Also the nice thing about working from the probability distributions is that we can continue analyzing our quantum source in terms of joint statistics rather than POVMs and density matrices.

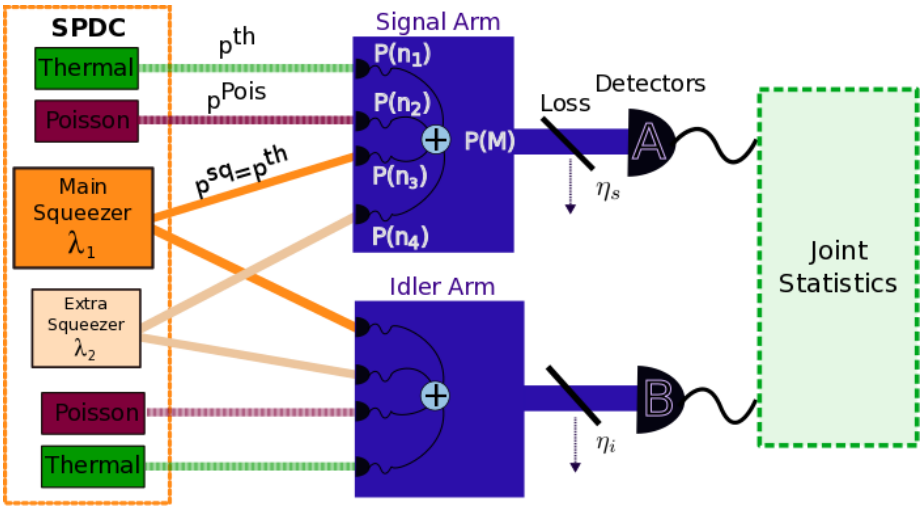


Figure 4.11: A more detailed depiction of the SPDC process originally depicted in Figure 4.1 includes additional squeezers, thermal and Poissonian noise, losses, and imperfect detectors. The origin of the photons cannot be distinguished by the detector, hence they appear as one mode by the time they arrive at the detector. The combined detected result is the same as adding results from each mode, shown in the blue boxes labelled signal and idler arm.

From Figure 4.11, we look at the probability of generating n photons from each contribution (labelled 'Thermal', 'Poissonian', etc in the boxes in the far left of Figure 4.11), which is defined by the photon probability distribution $p_\mu(n)$ for mean photon numbers μ. The possible contributions are additional squeezers (as discussed in

Chapter 3), but also possible thermal contributions from slight mode mismatch between the signal and idler or Poissonian contributions from pump laser leak through, detector dark counts and fluorescence. Therefore we can conclude that all the main contributions will have thermal and Poissonian photon-number (n) probability distributions, $p_\mu^{\text{Pois}}(n)$ and $p_\mu^{\text{therm}}(n)$ respectively:

$$p_\mu^{\text{Pois}}(n) = \frac{e^{-\mu}\mu^n}{n!} \tag{4.18}$$

$$p_\mu^{\text{therm}}(n) = \frac{\mu^n}{(1+\mu)^{n+1}}. \tag{4.19}$$

To help us visualize, simulations of individual thermal and Poissonian distributions are shown in Figure 4.12 for different average mean photon numbers.

We also need to remember that the photon number probability distribution from just looking at one arm of a correlated two-mode squeezed source has the same distribution as a thermal source:

$$p_\mu^{\text{Sq one arm}}(n) = p_\mu^{\text{therm}}(n). \tag{4.20}$$

As a recap, although the photons in the signal and idler modes are perfectly correlated from the pairwise nature of the photon creation process, the signal and idlers statistics in each mode alone are thermal as we discussed in Chapter 3 and see from a two-mode squeezed state output:

$$|\psi\rangle = \frac{1}{\sqrt{\mu+1}} \sum_{n=0}^{\infty} \left(\frac{\mu}{\mu+1}\right)^{n/2} |n,n\rangle\,. \tag{4.21}$$

Our aim in the next section is to understand the breakdown of the various contributions by analyzing the marginal photon statistics.

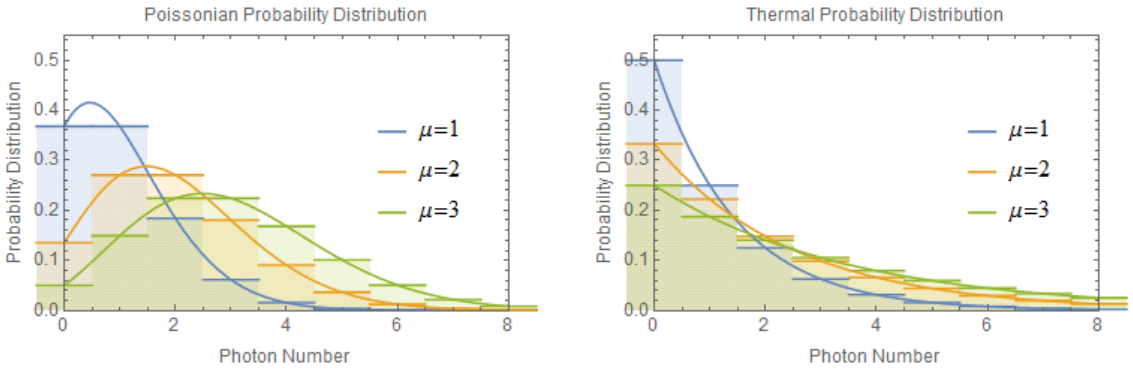


Figure 4.12: The left and right figures show the difference between Poissonian and thermal probability distributions respectively for various mean numbers- taking note this is for just one contribution in each plot (the effect of multiple contributions combined will be shown in Figure 4.13).

4.3.2 Marginal photon-number statistics

We are interested in what we can separately learn from the signal and idler arm. In order to do so, we need to determine how to analyze photon number statistics when multiple contributions are combined (visually the blue boxes in signal and idler arm of Figure 4.11).

4.3.2.1 Theory expressions

The number of photons that occur from each contribution (a.k.a. in each mode) is separate, so the probability of simultaneously generating n_j photons in each mode j is given by a probability multiplication rule:

$$P(n_1, ...n_j...) = \prod_j p_{\mu_j}(n_j). \tag{4.22}$$

To combine the statistics from multiple uncorrelated distributions and find the probability of generating a total of M photons, we use the additive role of probability of

mutually exclusive events given by:

$$P(M) = \sum_{\sum n_j = M} \prod_j p_{\bar{\mu}_j}(n_j). \tag{4.23}$$

Visually we look at what happens to the photon number probability distributions when one or more contributions are combined for thermal, Poissonian and squeezed sources, shown in Figure 4.13.

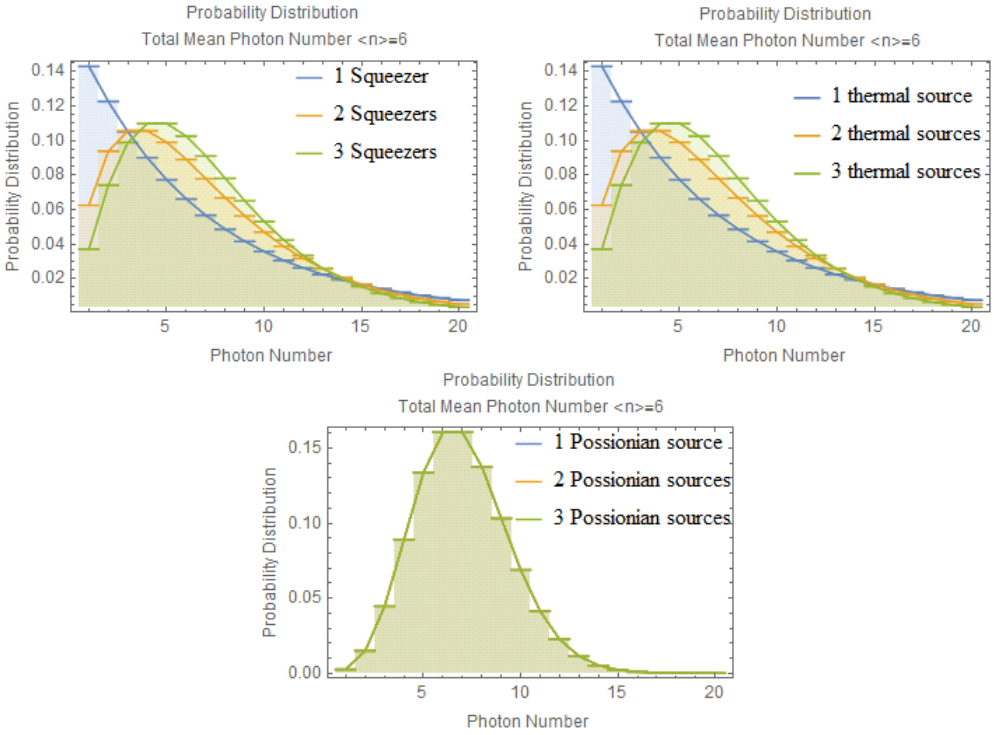


Figure 4.13: Now for the same mean photon number, let us look at different number of source distributions. For instance let's set the total mean photon number $\langle n \rangle = 6$ (which is set unrealistically high for our experiments but helps us visualize the distributions better). It means that with one squeezer, thermal or Poissonian source the set mean photon number is $\langle n \rangle = 6$, for two sources $\langle n \rangle = 3$ each, and for three sources $\langle n \rangle = 2$ each. The top two plots demonstrate that the photon statistics from one arm of a squeezer (left plot) is the same as a thermal sources in that arm (right plot). The bottom plot shows that the photon number distribution from one, two or three Poissonian sources are identical, meaning any combination of Poissonian sources are the same as long as the total mean photon number is the same.

4.3.2.2 Measurements and fits to data

Let us take this theory and now apply it to our experimental data. We plot the photon number probability distribution for the full range of mean photon numbers accessible in our experiment, Figure 4.14. We create a fit function which varies

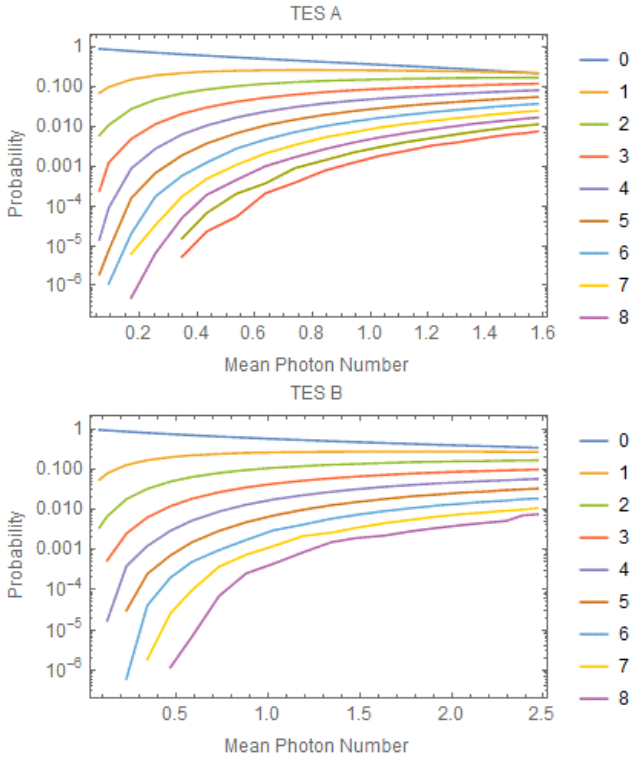


Figure 4.14: Looking at the outputs from one detector at a time (the top and bottom figure show data from TES A and TES B respectively), we plot the photon number distribution for a range of mean photon numbers. The individual traces give the probability for the different photon numbers (0-8), the vertical axis showing the probability on a log scale.

the strengths for two different possible thermal contributions (assuming one thermal contributions from the single mode of the main squeezer and a second contribution from a possible secondary squeezer or other noise) and a single Poissonian contribution (since mixing several Poissonian distributions results in a Poissonian distribution shown in Figure 4.13) to find the best fit between the model and the data from the

marginal distribution. This allows us to determine the type of modes in our source as a means of mode structure analysis. We are able to determine that there are two thermal modes in each arm with the weights $\lambda_1 = 1$, $\lambda_2 = .09$ and negligible Poissonian contributions. In Figure 4.15, we plot the experimental marginal photon-number probability distributions for two different mean photon numbers $\langle n \rangle = 1.35$ and 1.92. In the same figure, we use the results of the fits, and plot the corresponding simulated data, which factors in two thermal modes in each arm with the weights $\lambda_1 = 1$, $\lambda_2 = .09$. As the plots show, the experimental data and fit overlap very well.

Even though we can not confirm if the two thermal modes are from correlated sources or uncorrelated sources from the marginal statistic alone, we are able to assume that the main thermal source from both marginals, A and B, originate from the same squeezer, meaning in the ideal case without loss there should be perfect photon number correlations in both arms. Therefore the ratio of counts from the main thermal source in each arm would gives us the ratio of each arm's efficiencies. As a visual we plot the linear relation from our data between the mean photon number and power in Figure 4.16. Roughly the ratio of counts in TES A : TES B is proportional to the ratio of the efficiency $\eta_A : \eta_B$ (roughly 1:0.67). For a more accurate characterization of the source, we will look at the joint statistics in the following section.

4.3.3 Joint photon-number statistics

In this section, we now want to look at the joint statistics to gain more information from the correlations between signal and idler arms. We use the results from the mode

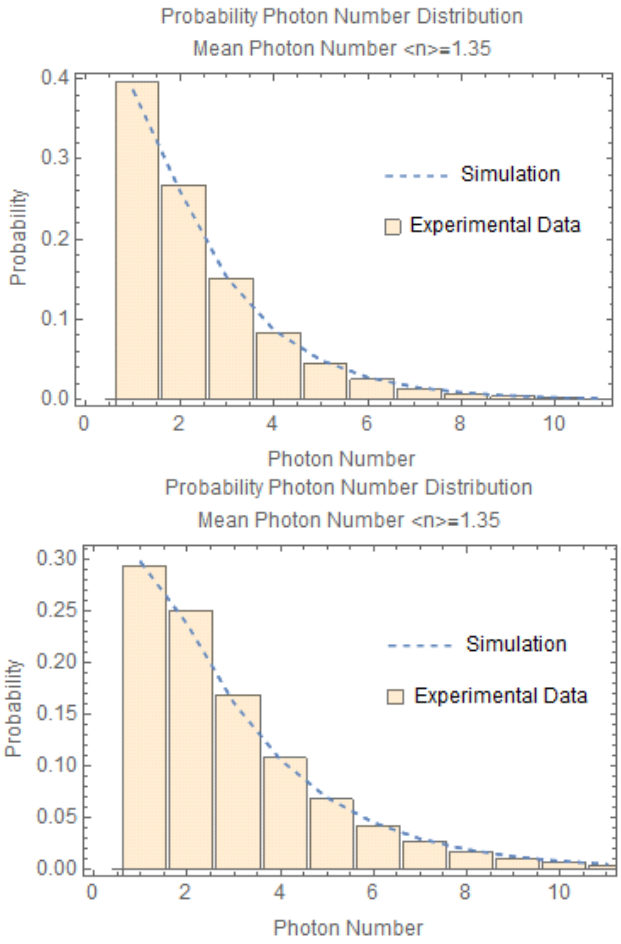


Figure 4.15: These two plots show the marginal photon-number probability distributions with bar graphs representing data (errors smaller than data points) and simulation dashed blue line. The top plot has a mean photon number of $\langle n \rangle = 1.35$ arriving at the detector and the bottom plot has a mean photon number of $\langle n \rangle = 1.92$.

structure analysis on the marginal probability distribution from above to refine the mode structure model in this next section by taking into account the joint probability distribution.

4.3.3.1 Theory

The marginal photon number statistics gave us the break down of the different types of fields in each arm. Now we use the experimentally measured joint photon-number probability distribution $P(n_s, n_i)$, which gives us the probability of detecting the

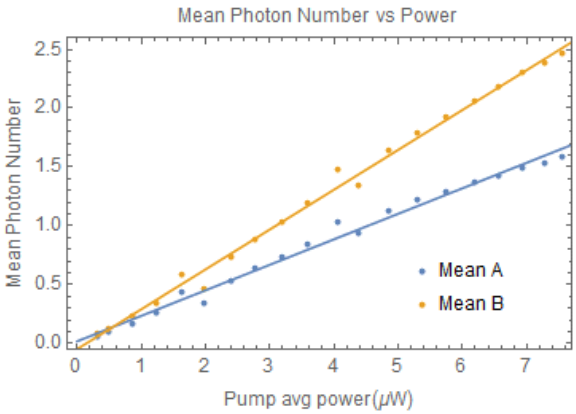


Figure 4.16: Plot showing the linear relationship between the power and mean photon numbers for the power range that we work in. We will use these linear fits to give us the efficiency ratio between both arms.

number of photons n_s and n_i simultaneously in the signal and idler arms respectively, to give us information about whether these fields come from correlated or uncorrelated fields with particular statistical distributions. With this new model we simulate and reconstruct the optical mode structure of our SPDC sources.

The joint probability distribution for a two-mode squeezed state that has a correlated distribution:

$$P_c^{\mathrm{Sq}}(n_s, n_i) = |\langle n_s, n_i|\psi\rangle|^2 = \delta_{n_s,n_i}\frac{\mu^n}{(1+\mu)^{n+1}} = \delta_{n_s,n_i}p_\mu^{\mathrm{therm}}(n). \tag{4.24}$$

Losses in correlated modes, are not so simple because losses in correlated arms have to be considered independently[1]. We incorporate losses discussed in section 4.2.3.2 with the joint probability distribution for a two-mode squeezed state:

$$P_{\mathrm{w\ loss}}^{\mathrm{Sq}}(n_s, n_i) = L_{n_j^s,k_j}(\eta_j^s)L_{n_j^i,k_j}(\eta_j^i)P_c^{\mathrm{Sq}}(n_s, n_i). \tag{4.25}$$

[1]In comparison, losses in uncorrelated modes will only alter the mean photon number while maintaining the same photon probability statistics, so the loss-adjusted mean photon number $\bar{\mu}_j$ replaces $\bar{\mu}_j = \mu_j\eta_j$ in the probability evaluations for uncorrelated distributions.

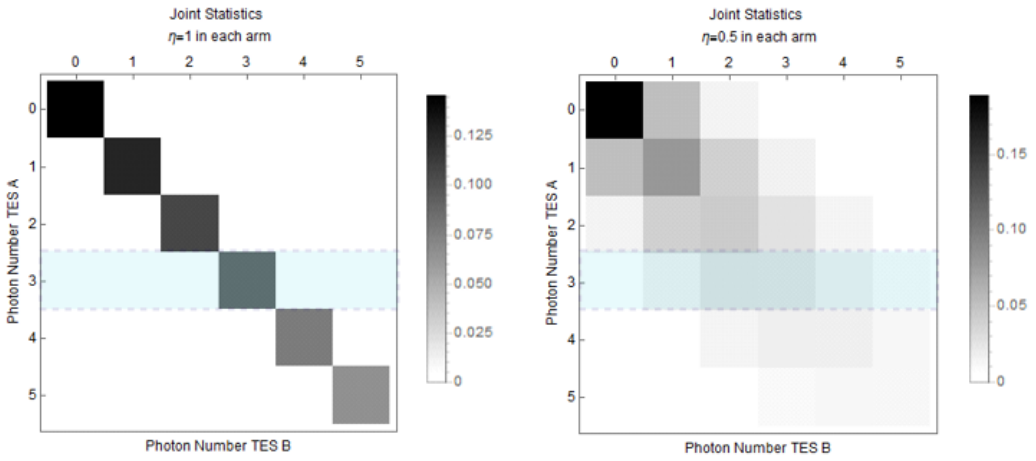


Figure 4.17: These simulations show the joint photon number statistics for two different loss scenarios. The figure to the left shows the ideal case when there is perfect efficiency (no loss and 100% detector efficiency $\eta = 1$). The result is a exact photon number correlations, which is apparent as a perfect diagonal along the TES A and TES B joint probability matrix. The plot to the right shows what happens when there is for example 50% loss. The spread is much larger as loss affects the perfect 1 to 1 photon number correlation. The rows highlighted in blue are the cross sections that we will look at in Figure 4.18.

The total joint probability distribution, taking into account all the correlated and uncorrelated modes from Equation (4.23) and (4.25) respectively, is given by:

$$P^{\text{TOTAL}}(n_s, n_i) = \sum_{\substack{N_s+M_s=n_s \\ N_i+M_i=n_i}} P^{\text{Sq}}_{\text{w loss}}(N_s, N_i) P_{u_s}(M_s) P_{u_i}(M_i) \tag{4.26}$$

where n_s, n_i are the number of photons detected in the signal and idler arms respectively and P_{u_s} and P_{u_i} are the uncorrelated parts in signal and idler arm respectively that could be composed of a combination of independent thermal and Poissonian contributions.

4.3.3.2 Measurements and fit to data

In the ideal lossless case, n photons in one arms means that there are n photons in the other arm such that the distribution only has probabilities along the main diagonal of the JPD and zero everywhere else as shown in Figure 4.17(a). However losses and

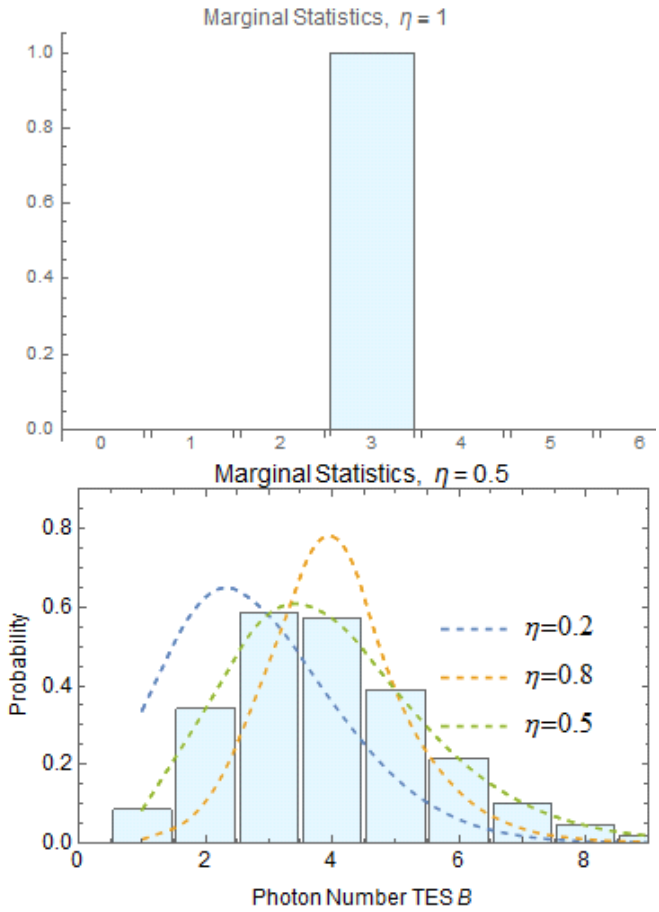


Figure 4.18: These figures show the normalized cross sections of the joint photn number probability distributions (the rows that were highlighted in blue from Figure 4.17). The top histogram shows the simulation when there is perfect efficiency. The bottom histogram shows when there is 50% efficiency and has additional fits (blue, green and yellow dashed lines) that show the different normalized photon number distributions for a system with $20\%, 50\%, 80\%$ efficiency

extra modes contaminate the signal shown in Figure 4.17(b). We can see this further in the cross section of the JPD (dotted line in figures) as the probability distribution $P(m, 3)$.

Using the results from the fit function that we acquired with the marginal photon statistics (we concluded that our source is made up of 2 thermal probability contributions with weights of 1 and 0.09), we use these outcomes as inputs into a fitting function that is used to determine whether or not thermal contributions are from

correlated or uncorrelated sources. We then determine the relative efficiency in each arm. We reconfirmed that Poissonian sources are not contributing factors, and that both marginal thermal contributions come from two mode squeezers that produce correlated photon numbers in each arm. We also conclude that the efficiencies in arm A and B are $\eta_A = 0.48$ and $\eta_b = 0.32$. It corresponds with the efficiencies that we measured using Klyshko measurements $\eta_A = 0.5$ and $\eta_b = 0.35$, discussed is Section 4.2.3.3. With Klyshko measurements one has to take measurements for a range of powers, whereas this method, using marginal and joint photon number statistics is the preferred method, because it just needs one measurement at one setting. Moreover, Klyshko measurements use click detectors so you have to extrapolate the data whereas with this method you do not.

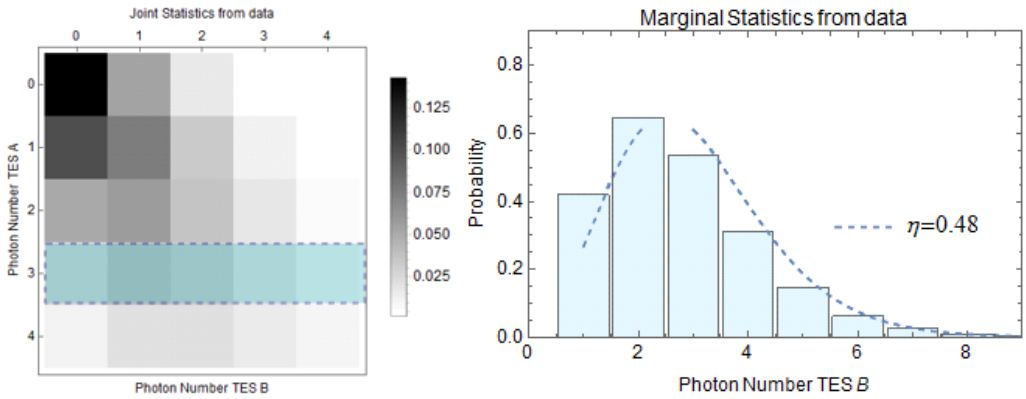


Figure 4.19: Here in the left figure, we plot the joint probability photon-statistics of our experimental data with a mean photon number of $\langle n \rangle = 1.4$. The right bar graph shows the cross section of the joint probability distribution (the row that is highlighted blue in left figure). It shows the photon number distribution seen by TES B, when heralding on a photon number that equals three in TES A. The dashed line is the simulated curve with a loss of $\eta = 0.48$.

In conclusion, we use the observable statistical properties of the quantum states to lead us to a better understanding of the physical properties of the states. In doing

so, we are able to characterize the source we are working with more accurately and able to determine the capabilities and the limitations of our source. In the end we conclude that a second squeezer contributes by a factor of 0.09 but all other thermal and Poissonian contributions are negligible. Hence our SPDC source from a PPKTP waveguide generates primarily one single two-mode squeezer, meaning that all of the generated light adds to the squeezing in this mode. This naturally leads to high squeezing values. In addition, it means that we can herald spectrally pure single photons from this source.

4.3.4 Correlation functions

We now use all the information that we acquired from the marginal and joint probability photon number statistics and use our simulation to model unheralded and heralded second order correlation measurements. We compare the simulation with the measurements that we take with photon number resolving TES detectors.

4.3.4.1 Unheralded $g^{(2)}$

In Chapter 3, we showed how to measure an unheralded second order correlation $g^{(2)}$ with click detectors by placing a balanced beam-splitter in an unheralded arm and measuring the photon number statistics from the two beam-splitter outputs. Now we will measure the unheralded $g^{(2)}$ with photon number resolving TES detectors. We start with the second order correlation function [72]:

$$g^{(2)} = \frac{\langle \hat{a}^\dagger \hat{a}^\dagger \hat{a} \hat{a} \rangle}{\langle \hat{a}^\dagger \hat{a} \rangle^2} \tag{4.27}$$

$$= \frac{\langle n^2 \rangle - \langle n \rangle}{\langle n \rangle^2}. \tag{4.28}$$

We measure the unheralded g^2 as a function of mean photon number and compare our simulation fits to the data, shown in Figure 4.20. Discrepancies occur at low powers with mean photon number of .01 where presumably the TESs have difficulty distinguishing between photon number and at high powers where there is some other process we can not fully account for.

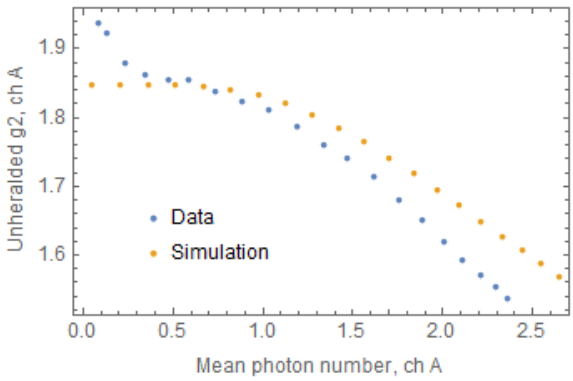


Figure 4.20: Plots of experimental unheralded $g^{(2)}$ and simulations. The blue dots are data (errors smaller than visible data points) and the yellow the simulation with two squeezer: one main squeeze with a weight of 1 and a second squeezer with a weight of 0.09. The TES detectors have difficulty resolving photon numbers when the power is super low, hence the discrepancy in the blue data at the lowest mean photon numbers, but we can use the simulation to extrapolate a $g^{(2)}$ value of 1.85. At mean photon numbers higher than 1, the data likely veers away from the simulations because of photon detector saturation effects

As expected because there is an additional two-mode squeezed vacuum contribution, the result is a "less thermal" distribution (i.e. the unheralded $g^{(2)}$ value is less than 2). For thermal statistics, $g^{(2)} = 2$ and for Poissonian statistics $g^{(2)} = 1$. The $g^{(2)}$ value from our simulation shows that we have a $g^{(2)}$ of 1.85. This is lower than the value measured with click detectors ($g^{(2)} = 1.91 \pm .05$). We need to take into account that there had been experimental changes and adjustments between both measurements, and it is not always easy to get back to the exact same setting. Also

during the measurements with click detectors, there were more power fluctuations than usual which artificially makes the mode seem more thermal and result in a $g^{(2)}$ that is higher than it really is.

4.3.4.2 Heralded $g^{(2)}$

Heralding a single photon state from a click in one mode can leave remnants of higher order photon contributions in the other modes. Therefore the quality of the heralded signal photon is important, meaning that if we see an outcome that says we have detected a single photon or any specified photon number, we need to know with a high level of certainty that the number of photons in the heralded arm is indeed the heralded photon number.

We use a heralded $g^{(2)}$ measurement to gauge the quality of heralded single photons and larger photon number states. A heralded $g^{(2)}$ measurement means measuring the $g^{(2)}$ in one mode conditioned on a certain outcome in the other mode. For ideal n-photon Fock states $g^{(2)} = 1-1/n$. (Values below 1 indicate nonclassical subpoissonian statistics, even when heralding on a much larger photon number event [46].) In Figure 4.21, we show the difference between simulated heralded $g^{(2)}$ measured with click detectors and photon number resolving detectors, when we herald on a single photon. In the ideal case, for a perfect single photon source the heralded $g^{(2)}$ stays close to the value of 0, demonstrating that it would never be possible to detect two photons or more emitted simultaneously by the source. However if there is loss, then measurements at higher mean photon numbers would cause the single photon signal to be contaminated, leading to a $g^{(2)}$ measurement that is higher than 0. We see

a clear benefit in photon number resolving detector as the efficiency in all the arms improves.

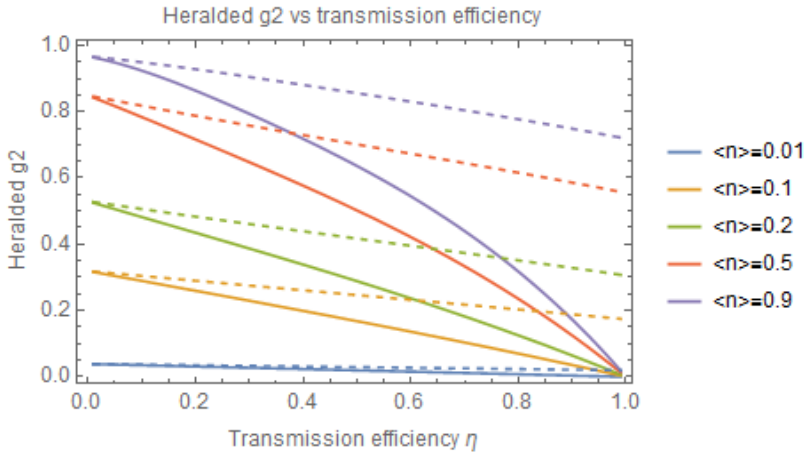


Figure 4.21: Simulated heralded $g^{(2)}$ for click detectors (dotted lines) and photon number resolving detectors (solid lines) for five different mean photon number settings $\langle n \rangle = 0.01, 0.1, 0.2, .0.5, 0.9$. As the transmission efficiency improves, it becomes evident that the single photon detectors result in a $g^{(2)}$ much loser to the ideal value of 0 than click detectors.

We perform the heralded $g^{(2)}$ experimentally with photon number resolving detectors, heralding on one photon in the heralding arm, plotted in Figure 4.22. It shows that it is possible to achieve close to single photons but because of losses in the system, this is only possible by keeping the mean photon numbers low. For instance if we keep the mean photon number as low as 0.1 photons per pulse than we can achieve a heralded $g^{(2)}$ of 0.2. The simulation matches well with the data until we reach mean photon numbers higher than $\langle n \rangle > 1.5$, similar to the the unheralded case.

4.3.5 Heralding higher photon number states

We not only care about the fidelity of single photon state, but we also care about heralding higher photon states. In Figure 4.19, we plot the joint probability photon-

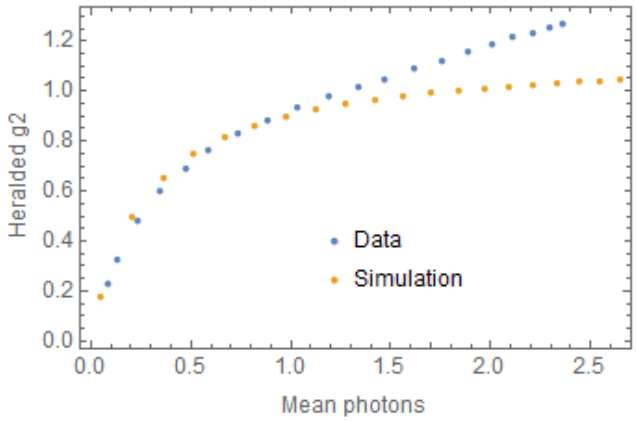


Figure 4.22: The blue data points (errors smaller than data points) represent the measured heralded $g^{(2)}$ as a function of mean photon number detected with TES detectors and the yellow data points represent the results from simulation.

statistics of our experimental data and then show how the photon number distribution looks when higher photon numbers are heralded. Because of losses, detection is not able to select on certain higher photon numbers perfectly such as shown in the first Figure of 4.18.

4.4 Conclusion

In Chapter 4 we discussed how click detectors (specifically InGaAs SPADs) and photon number resolving transition edge sensor detectors work. We discussed how to generate an appropriate model to simulate the click or photon number resolving measurements taking into account loss. We discussed the typical way to measure loss with click detectors via Klyshko measurements and then we experimentally performed those measurements as a way to gauge or system's overall efficiency including detector efficiencies. The results we attain are 50% in one arm and 35% in the other arm. The signal and idler photons have two different polarisations, thus they have

two different spatial field distributions inside the waveguide. We can only optimise for one (signal or idler) and, thus, the most likely cause for the different efficiencies.

With the introduction of photon number resolving detectors, we explored more accurate measurements based off of photon-number statistics. We discussed the different possible contributions such as additional squeezers, as discussed in Chapter 3, but this time we also looked at thermal and Poissonian noise. More importantly we now have the ability to measure the strengths of these various contributions by looking at the marginal and joint photon number statistics. We find through our simulations and fits that our source consists of a main squeezer and a second squeezer at 9% of that strength, and does not have major uncorrelated thermal or Poissonian noise. Moreover from the photon number statistics we determine the loss, which gave us 47% and 32% in arm A and B respectively, which correspond to the Klyshko efficiencies we measured before. In conclusion, we measured the heralded and unheralded $g^{(2)}$ measurements with photon number resolving detectors to benchmark the performance of your source, and having determined the contributions and strengths of our source, we found that the measurements fit well with theory.

We found that the unheralded $g^{(2)}$ measurements that we performed with photon number resolving detectors corresponded to the unheralded $g^{(2)}$ measurements we performed with click detectors in Chapter 3. The heralded $g^{(2)}$ measurements show us that we can have uncontaminated single photons when the mean photon number is low. Also with single photon resolving detectors, the heralded second order correlation function can be used to quantify the fidelity on an m-photon state. This is important because there is great interest for various quantum applications for

knowing the feasibility of creating an m-photon state. The single photon resolving detectors provide improvement but the significant improvement will become much more evident with improved efficiency. Hence, we continually work at improving the efficiency of our source so we can get to the next level of possibility.

Chapter 5

Quantum Interference of Photon Number States

After building two SPDC photon sources, integrating the sources with photon-resolving detectors, and characterizing the sources/detectors in the previous chapters, we explore new territory involving multiphoton interference in this chapter. First we demonstrate single photon Fock state interference on a balanced beam splitter, and then single and two photon Fock state interference on a variable beam splitter and discuss the advantages of multi-photon interference.

There are two basic interference setups that are of specific interest for quantum information science. One is a simple balanced beam-splitter where Hong-Ou-Mandel (HOM) interference occurs [51]. The second is the Mach-Zehnder interferometer, which is a phase shift between two beam-splitters. This can be interpreted as a beam-splitter with varying reflectivity, with the reflectivity given as function of the phase shift. A Mach-Zehnder interferometer is the standard implementation of the phase estimation problem [27]. If we want to measure a phase very precisely, we embed it in a Mach-Zehnder and look at the output intensity distribution, which is similar to looking at the output intensity distribution of a beam-splitter with varying

reflectivity. Higher-order photon number states are better for measuring phases (see Holland Burnett states with full theory [49]). We will show this with our system.

5.1 HOM interference with balanced beam-splitter

The simple HOM interference can be used to benchmark the source performance. We will present the full broadband theory, and then show the measurement results.

5.1.1 Full broadband theory

We study two photon interference on a balanced beam splitter with one photon in each input port. We look at the number of coincidences between the two output ports of the beam-splitter because this reveals the quantum properties of the photons.

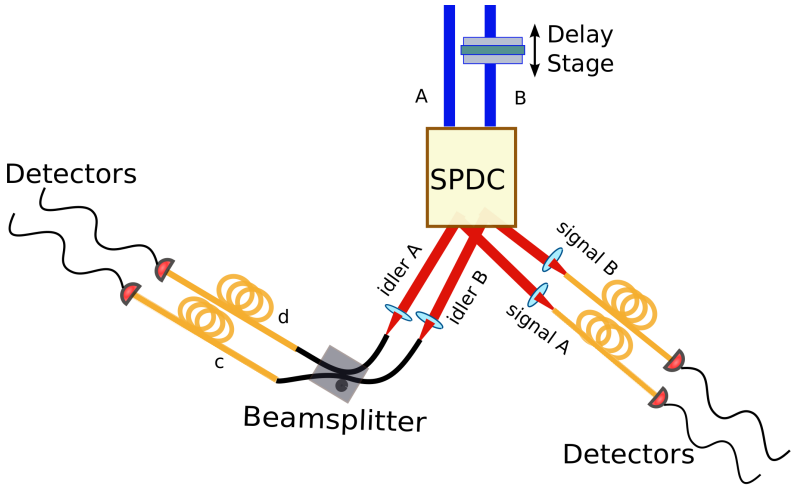


Figure 5.1: Setup for HOM interference: the heralded idler photons from two sources are interfered on a 50:50 polarization-maintaining beam-splitter. To make sure the arrival times overlap from both sources, one arm before entering the waveguide is on a motorized delay stage. For this experiment we measured the counts with superconducting nanowire single photon detectors. (For a more detailed diagram of all the filters and lenses refer back to Figure 1.6.)

In this section, we focus on the scenario when one photon enters each input port. The two photons originate from two photon pairs generated by the SPDC process. A

time delay is placed in one input arm to the SPDC crystal, in our case the $\hat{b}$-arm, to control the temporal overlap between the photons, see Figure 5.1. The corresponding operator transformation is $\hat{b}(t) \rightarrow \hat{b}(t - \delta\tau)$. After the balanced beam-splitter, using the asymmetric beam-splitter description where the phase shift occurs only for one reflection, the Heisenberg transformations of the operators in the output arms of the beam-splitter $\hat{c}$ and $\hat{d}$ in terms of the input arms are as follows,:

$$\hat{c}^\dagger(t) = \frac{1}{\sqrt{2}} \left(\hat{a}^\dagger(t) + \hat{b}^\dagger(t - \delta\tau) \right) \tag{5.1}$$

$$\hat{d}^\dagger(t) = \frac{1}{\sqrt{2}} \left(\hat{a}^\dagger(t) - \hat{b}^\dagger(t - \delta\tau) \right). \tag{5.2}$$

The coincidence probability at time t_1 and t_2, when exactly one single photon entered arms A and B, is:

$$P_{\text{coinc}}(t_1, t_2; \tau) = \langle \psi_{\text{in}} | \, \hat{c}^\dagger(t_1) \hat{d}^\dagger(t_2) \hat{d}(t_2) \hat{c}(t_1) \, | \psi_{\text{in}} \rangle \tag{5.3}$$

which by inserting Equation (5.2) becomes

$$\begin{aligned} P_{\text{coinc}}(t_1, t_2; \tau) = \frac{1}{4} \langle \psi_{\text{in}} | \left(\hat{a}^\dagger(t_1) + \hat{b}^\dagger(t_1 - \delta\tau) \right) \left(\hat{a}^\dagger(t_2) - \hat{b}^\dagger(t_2 - \delta\tau) \right) \\ \left(\hat{a}(t_2) - \hat{b}(t_2 - \delta\tau) \right) \left(\hat{a}(t_1) + \hat{b}(t_1 - \delta\tau) \right) | \psi_{\text{in}} \rangle \end{aligned} \tag{5.4}$$

$$\begin{aligned} = \frac{1}{4} \langle \psi_{\text{in}} | \Big(\hat{a}^\dagger(t_1)\hat{a}^\dagger(t_2) - \underline{\hat{a}^\dagger(t_1)\hat{b}^\dagger(t_2 - \delta\tau)} + \underline{\hat{a}^\dagger(t_2)\hat{b}^\dagger(t_1 - \delta\tau)} - \hat{b}^\dagger(t_1 - \delta\tau)\hat{b}^\dagger(t_2 - \delta\tau) \Big) \\ \Big(\hat{a}(t_1)\hat{a}(t_2) + \underline{\hat{a}(t_1)\hat{b}(t_2 - \delta\tau)} - \underline{\hat{a}(t_2)\hat{b}(t_1 - \delta\tau)} - \hat{b}(t_1 - \delta\tau)\hat{b}(t_2 - \delta\tau) \Big) | \psi_{\text{in}} \rangle . \end{aligned} \tag{5.5}$$

We only look at the underlined terms with one photon from both $\hat{a}$ and $\hat{b}$ (the other terms evaluate to zero, because they contain two creation or annihilation operators for the same mode. The input state has only one photon in each $\hat{a}$ and $\hat{b}$, so having

two annihilation operators act on that state yields zero):

$$\begin{aligned} P_{\text{coinc}}(t_1, t_2; \tau) = \frac{1}{4} \langle \psi_{\text{in}} | &- \hat{a}^\dagger(t_1)\hat{a}(t_2)\hat{b}^\dagger(t_2 - \delta\tau)\hat{b}(t_1 - \delta\tau) \\ &+ \hat{a}^\dagger(t_2)\hat{a}(t_2)\hat{b}^\dagger(t_1 - \delta\tau)\hat{b}(t_1 - \delta\tau) \\ &+ \hat{a}^\dagger(t_1)\hat{a}(t_1)\hat{b}^\dagger(t_2 - \delta\tau)\hat{b}(t_2 - \delta\tau) \\ &- \hat{a}^\dagger(t_2)\hat{a}(t_1)\hat{b}^\dagger(t_1 - \delta\tau)\hat{b}(t_2 - \delta\tau) \, |\psi_{\text{in}}\rangle \, . \end{aligned} \tag{5.6}$$

In practice, the coherence time of the photons is much narrower than the temporal resolution of the two detectors. Thus the coincidence rate, i.e. the normalized number of detected coincidences, can be written as:

$$R(\tau) = \int \int dt_1 dt_2 P_{\text{coinc}}(t_1, t_2; \tau). \tag{5.7}$$

The photons entering the input ports in our source are pulses with a finite duration time (rather than the example in the Chapter 1 which examines photons that are exactly located in time $|\psi\rangle_1 = \hat{a}^\dagger(t)\,|0\rangle$ and $|\psi\rangle_2 = \hat{b}^\dagger(t)\,|0\rangle$). Photons with finite duration time are expressed as:

$$|\psi\rangle_1 = \int dt f(t)\hat{a}^\dagger(t)\,|0\rangle\,, \quad |\psi\rangle_b = \int dt' g(t')\hat{b}^\dagger(t')\,|0\rangle\,, \tag{5.8}$$

with

$$\int dt f^*(t)f(t) = \int dt g^*(t)g(t) = 1. \tag{5.9}$$

As an example, the first term in the Equation (5.6) becomes:

$$\langle \psi_{\text{in}} | - \hat{a}^\dagger(t_1)\hat{a}(t_2)\hat{b}^\dagger(t_2 - \delta\tau)\hat{b}(t_1 - \delta\tau)\,|\psi_{\text{in}}\rangle \tag{5.10}$$

$$\begin{aligned} &= - \langle 0 | \int dt dt' f^*(t)g^*(t')\hat{a}(t)\hat{b}(t')\hat{a}^\dagger(t_1)\hat{b}^\dagger(t_2 - \delta\tau) \\ &\qquad \cdot \int dt'' dt''' f(t'')g(t''')\hat{a}(t_2)\hat{b}(t_1 - \delta\tau)\hat{a}^\dagger(t'')\hat{b}^\dagger(t''')\,|0\rangle \end{aligned} \tag{5.11}$$

$$= -f^*(t_1)g^*(t_2 - \delta\tau)f(t_2)g(t_1 - \delta\tau) \tag{5.12}$$

By focusing on photons with finite duration time, Equation (5.6) and Equation (5.7) gives us:

$$\begin{aligned} R(\tau) = \frac{1}{4}\int dt_1 dt_2 [&- f^*(t_1)g^*(t_2-\delta\tau)f(t_2)g(t_1-\delta\tau) \\ &+ f^*(t_2)g^*(t_1-\delta\tau)f(t_2)g(t_1-\delta\tau) \\ &+ f^*(t_1)g^*(t_2-\delta\tau)f(t_1)g(t_2-\delta\tau) \\ &- f^*(t_2)g^*(t_1-\delta\tau)f(t_1)g(t_2-\delta\tau)]. \end{aligned} \tag{5.13}$$

With the knowledge of Equation (5.9), we find that the second and third term of Equation (5.13) equals one, which leads to:

$$R(\tau) = \frac{1}{2} - \frac{1}{4}\int dt_1 dt_2 [f^*(t_1)g^*(t_2-\delta\tau)f(t_2)g(t_1-\delta\tau) - f^*(t_2)g^*(t_1-\delta\tau)f(t_1)g(t_2-\delta\tau)] \tag{5.14}$$

$$= \frac{1}{2} - \frac{1}{2}\underbrace{\int dt_1 f^*(t_1)g(t_1-\delta\tau)}_{\mathrm{A}}\underbrace{\int dt_2 f(t_2)g^*(t_2-\delta\tau)}_{\mathrm{A}^*} \tag{5.15}$$

$$= \frac{1}{2} - \frac{1}{2}\left|\int dt_1 f^*(t_1)g(t_1-\delta\tau)\right|^2 \tag{5.16}$$

We assume that both photons have a Gaussian temporal distribution given by

$$f(t) = g(t) = \frac{1}{(2\pi)^{1/4}\sqrt{\sigma}}\exp\left(-\frac{t^2}{4\sigma^2}\right), \tag{5.17}$$

such that Equation (5.16) can now be written as:

$$R(\tau) = \frac{1}{2} - \frac{1}{2}\left|\frac{1}{\sqrt{2\pi}\sigma}\int dt \exp\left(-\frac{t^2}{4\sigma^2} - \frac{(t-\delta\tau)^2}{4\sigma^2}\right)\right| \tag{5.18}$$

$$= \frac{1}{2} - \frac{1}{2}\left|\exp\left(-\frac{\delta\tau^2}{8\sigma^2}\right)\right|^2 \tag{5.19}$$

$$= \frac{1}{2} - \frac{1}{2}\exp\left(-\frac{\delta\tau^2}{4\sigma^2}\right). \tag{5.20}$$

HOM interference can be used to characterize the indistinguishabilty and purity of our photons. To measure the indistinguishability of the interfering photons, it is

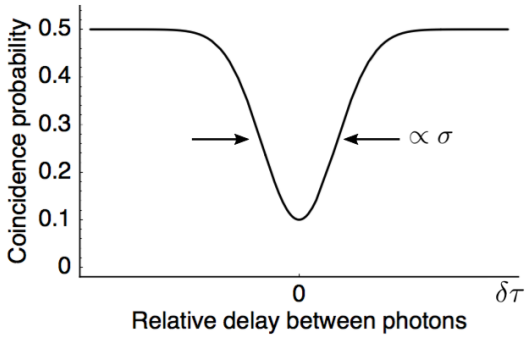


Figure 5.2: This figure shows a sample HOM dip taking into account photons that have a Gaussian temporal distribution. This plot is for photons with a remaining distinguishability whereas if both photons are identical than the coincidence probability goes down to zero.

customary to introduce a delay stage on one of the input paths into the beam-splitter in order to control the timing of the photons interfering in the beam-splitter. If the two photons at the input of the beam-splitter are distinguishable (for example if they have different frequencies, polarisation, or arrival time) then the amplitudes for "both transmitted" or "both reflected" do not cancel, and we are left with the situation where the coincidence probability of detecting one photon at each output is $P_C = 0.5$. However, if the two photons are perfectly indistinguishable then those terms cancel and the coincidence probability is $P_C = 0$.

By varying the relative temporal delay of the interfering photons, we intentionally make the photons distinguishable and register the number of coincidence events as a function of the time delay.

As the time delay is scanned, the coincidence rate of the detectors will drop towards zero if the two input photons are perfectly indistinguishable and overlap perfectly in time and then return to normal as the time delay causes the photons to be distinguishable, shown in Figure 5.2.

The visibility of this dip is characterized by

$$V = \frac{P_C(\infty) - P_C(0)}{P_C(\infty)}, \tag{5.21}$$

where $P_C(\tau)$ is the probability of obtaining coincidence detection as a function of time delay τ. The maximum visibility for classical light is $V_{\text{classical}} = 1/2$ [76], so any observed visibility greater than $V = 0.5$ is accepted as quantum interference [86]. For the interference of pure, indistinguishable single photons, the optimal visibility will be $V = 1$. This visibility can be interpreted as a measure of photon indistinguishability and (if they are from independent sources) photon purity. This makes the HOM dip a powerful characterization tool besides it being a primitive for quantum applications.

5.1.2 Single Photon HOM Experiment

In this section, I present the measured HOM interference dip from our sources. This measurement will yield the combined photon indistinguishability and purity.

To perform this measurement, the heralded idler photons from separate sources are interfered on a fiber-integrated polarization maintaining balanced 50:50 beamsplitter[1] to ensure spatial overlap. The signal photons are sent straight to detectors to herald the presence of the idler photons, as shown in Figure 5.1. We use superconducting nanowire detectors for this measurement because they are fast and reliable[2]. The filtering we use before the waveguide is described in Chapter 1 and shown in Figure 1.6. The FWHM of the pump is chosen to be 1.8 nm as determined by our unheralded $g^{(2)}$ vs pump FWHM plots Figure 3.7. To get the timing right between

[1]Fiber Coupler 50:50, 1550 nm, PM, FC/UPC from Newport Company
[2]Nanowires are bought from the company Photon Spot, Inc.

the two sources, we use a delay stage in one of the arms, which gives us 3 cm of flexibility (100 ps) with 50 nm of precision.

The coincidence rate versus a time delay in one of the beams is shown in Figure 5.3. We look at the reduction of coincidence counts due to the interference between identical single photons on the beam-splitter. The measurement is performed with intentionally low pump energy (pJ) per pulse leading to a mean photon number of 0.05. We make use of this visibility to estimate how indistinguishable our photons are and to verify that quantum interference is taking place. We obtain a visibility of $V = 85.9\% \pm 1\%$. The visibility is related to the density operators of the two photons by

$$V = Tr[\hat{\rho}_a \hat{\rho}_b]. \tag{5.22}$$

If the two photons are identical, i.e. $\hat{\rho}_a = \hat{\rho}_b$, then the visibility is equal to the purity of the photons

$$V = Tr[\hat{\rho}_a^2] = P, \tag{5.23}$$

The photons are spectrally indistinguishable by 99%, see Figure 2.12, so we take this as a close approximation. This coincides with our $g^{(2)}$ measurements that we made with the TESs. The $g^{(2)}$ has the connection with heralded purity $g^{(2)} \approx 1 + \mathcal{P}_{s,i}$ from Equation (3.13). We measured a $g^{(2)}$ of 1.85 which gives us an approximate purity of $\mathcal{P} \approx 0.85$. From Equation (5.23), the visibility from the HOM dip assumes an approximate purity of $\mathcal{P} \approx .859(1)$. Especially since the $g^{(2)}$ and the HOM measurement were measured a month apart, these correspond quite well. Hence the HOM dip validates the use of the correlation function measurement as a useful proxy for

heralded single-photon purity.

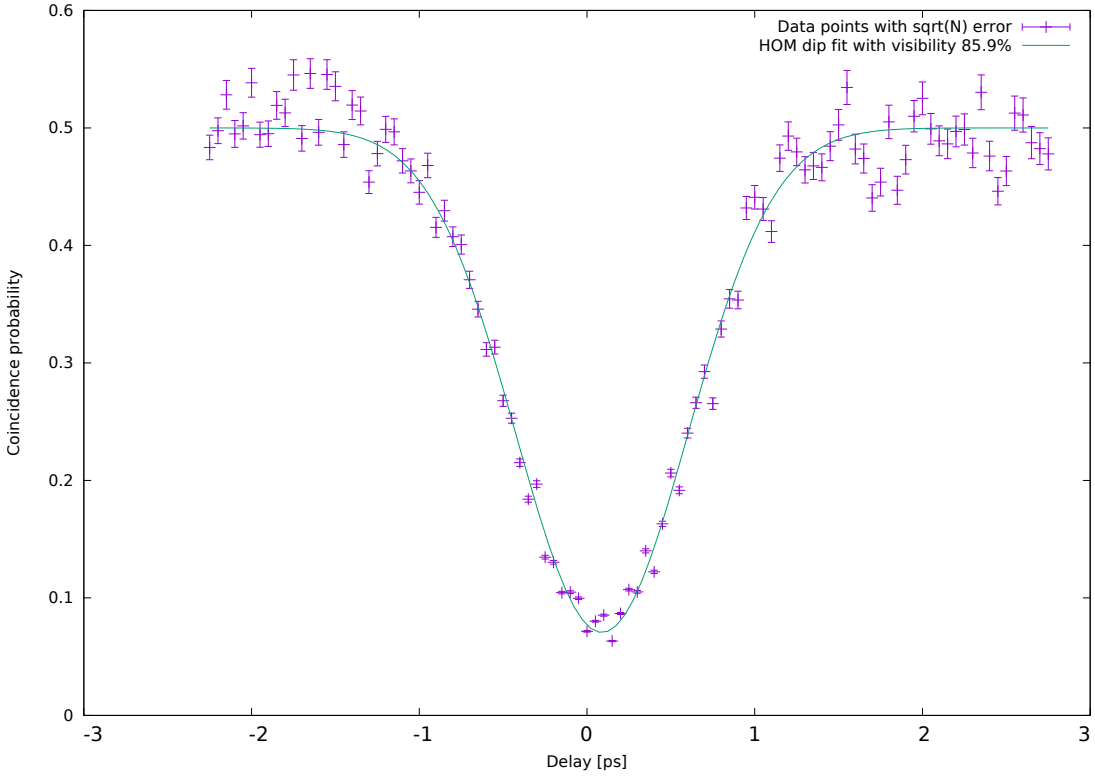


Figure 5.3: Experimental heralded two-photon HOM-dip. We test the indistinguishability and purity of our two single photon sources by performing a heralded HOM-dip by interfering the idler photons from both sources on a balanced 50:50 fiber beamsplitter. Their relative temporal delay is plotted on the x-axis. The fitted visibility is 85.9%. Poissionian error bars of $\sqrt{N}$ are shown.

There are not very many sources that generate high quality photons at telecom wavelengths without narrow spectral filtering. There exist very good sources at 830 nm without narrow spectral filtering [81, 56], but they are not applicable to telecom architectures. They also use a different dispersion configuration, which favours high photon purity at the cost of reducing signal-idler indistinguishability (interference of signal and idler from the same source would result in poor visibility). With the existing telecom sources (all based on KTP), signal and idler from the same source have been interfered to demonstrate high indistinguishability, but this measurement

only tests the exchangeability of signal and idler (i.e. how symmetric the PDC state is upon exchanging signal and idler), and does not give any insight into the purity of the photons after heralding [45, 38]. High visibilities can also be reached when applying strong spectral filtering [1]. However we have chosen to build sources that do not rely on external filtering, because strong filtering can introduce other problems (e.g. reduced heralding efficiencies due to filter losses). More recently, good quality HOM interference between photons from different sources has been measured in periodically poled KTP bulk crystal [55]. However, we are the first to demonstrate high quality HOM interference between photons from two independent, guided-wave, telecom PDC sources, which is an important step towards future integrated and thus scalable quantum network architectures.

5.2 Theory of Multiphoton HOM interference

We now push further past single photon interference to multi-photon interference on a variable beam-splitter. In this section we discuss the potential applications, the theory, model losses and discuss interference on a variable beam-splitter by looking at the joint probability distribution of photons from two sources.

5.2.1 Mach-Zehnder interferometer analogous to variable beam-splitter model

In Chapter 1, we explained how multi-photon interference would be useful for quantum technology, and could be used to yield higher resolution and more sensitive measurements than possible with classical approaches. Let us delve into this concept further.

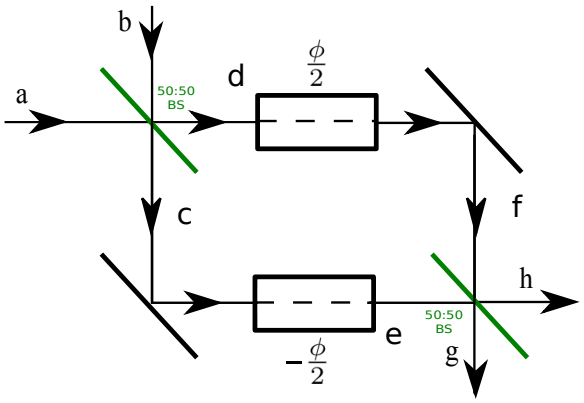


Figure 5.4: A Mach-Zehnder interferometer is a phase shift sandwiched between two balanced beam-splitters. The two input light modes are at a, b and two output modes are g, h. In a standard configuration a coherent state of light $|\alpha\rangle$ is sent into mode a. Detectors at the outputs measure the difference between the two output intensities $M = I_g - I_h$, which we shall call the signal, as a function of the phase shift, see Figure 5.5. In order to obtain quantum enhancement, one needs to make use of the b input port also, sending e.g. the squeezed vacuum state.

The paradigm multi-photon interferometer example is a Mach-Zehnder, shown in Figure 5.4, which is comprised of a phase shift in-between two beam-splitters. If we look at the matrix representation of mode transformations, a 50:50 beam splitter can be described by a Hadamard matrix:

$$H_{bs} = \frac{1}{\sqrt{2}} \begin{bmatrix} 1 & 1 \\ 1 & -1 \end{bmatrix} \tag{5.24}$$

The optical phase shifts between the two optical modes are represented by the matrix:

$$Z(\phi) = \begin{bmatrix} e^{i\phi/2} & 0 \\ 0 & e^{-i\phi/2} \end{bmatrix} \tag{5.25}$$

So then the Mach-Zehnder, which has two beam-splitters and a phase shift, is represented by the matrix:

$$U_{MZ}(\phi) = H_{bs} Z(\phi) H_{bs} = -i \begin{bmatrix} \sin(\phi/2) & \cos(\phi/2) \\ \cos(\phi/2) & -\sin(\phi/2) \end{bmatrix} \tag{5.26}$$

Classical scenario: if we insert classical light with intensity, I_a, into the input port a, shown in Figure 5.4, it is split at the first beam-splitter and recombined at the second beam-splitter after undergoing a phase shift. From Equation (5.26), light emerging from the output ports g and h have intensities $I_g = I_a \sin^2(\phi/2)$ and $I_h = I_a \cos^2(\phi/2)$ respectively. Energy is conserved such that $I_g + I_h = I_a$, for all values of ϕ. The intensities are measured and the resulting signal is taken to be the difference intensity $M = I_g - I_h$:

$$M(\phi) \equiv I_g - I_h = I_a \cos(\phi) \tag{5.27}$$

We plot M as a function of ϕ and see that it varies periodically in Figure 5.5. The uncertainty in the intensity change ΔM along the vertical axis of plot 5.5, is related to the uncertainty in phase $\Delta\phi$.

$$\frac{\Delta M}{\Delta \phi} = \frac{\partial M}{\partial \phi} = I_a \sin(\phi), \tag{5.28}$$

where the slope of the curve is $\partial M/\partial\phi$. The Equation (5.28) can be rewitten in terms of $\Delta\phi$:

$$\Delta\phi = \frac{\Delta M}{\partial M/\partial\phi} = \frac{\Delta M}{I_a \sin(\phi)}. \tag{5.29}$$

The minimal detectable phase difference is then smallest when the slope of the curve, $\partial M/\partial\phi$, is largest. But because of quantum mechanics and fluctuations of the electromagnetic field, there is a fundamental uncertainty indicated by the height of the uncertainty in the intensity displacement ΔM. For a coherent state, the intensity is proportional to the number of photons $I \propto n$ and has a standard deviation that is equal to the square root of the average number of photons $\sqrt{n}$ such that the intensity

displacement of M can never be measured with infinite precision, therefore measuring the phase ϕ will always have a related uncertainty $\Delta\phi$ which is shown by the width of the blue box.

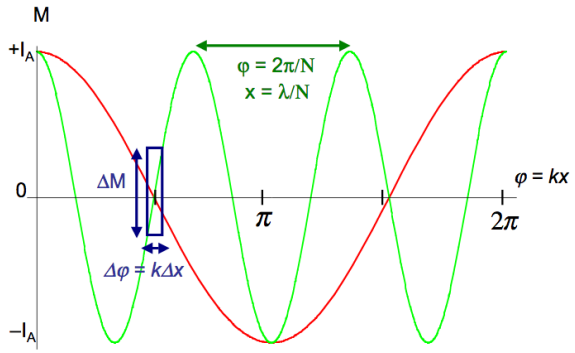


Figure 5.5: When classical light is inserted into the input ports of a Mach-Zehnder, we achieve the standard sensitivity. After the Mach-Zehnder, we look at the difference of intensities in the two output ports as function of the phase shift (red). Where the slope of the curve $\Delta M/\Delta\phi$ is largest, is where we achieve minimal phase uncertainty $\Delta\phi$. In order to obtain quantum enhancement, one needs to send in for example squeezed vacuum into the input. When Fock states are inserted into the input ports of the Mach-Zehnder, we get a bunched state after the first beam-splitter, and the fringes oscillate faster, resulting in larger slopes and hence higher measurement sensitivity. This specific example shown by the green fringe is of a three photon N00N state. A N00N state is a path-entangled N-photon state, which is a superposition of N photons in one arm and zero in the other and vice versa. This signal oscillates N times as fast as the coherent state (super resolution) and has maximum slope that is N times as steep (super sensitivity). (Here is an example of N=3). Figure from [29]. The effect is as if the N00N state was composed of photons with an effective wavelength of λ/N instead of λ.

Non-classical scenario: Quantum mechanics promises more precise measurements than possible classically. A classic example for obtaining high-precision measurements is by using two pairs of two-mode squeezed states, where one of the modes from each pair serves as herald and the remaining modes are fed through a Mach-Zehnder interferometer. Such a configuration can give rise to the famous Holland-Burnett state [20, 98]. To create a Holland-Burnett state, N photons, which can be generated from

the heralded SPDC process, are sent to both of the input arms of the first 50:50 beam-splitter. This input state can be written as $|\Psi\rangle = |N\rangle_a |N\rangle_b$. The important feature is noticing how coherent states of light versus photon number states are affected by the phase shift from Equation (5.25). When a coherent state passes through a phase shift in a Mach Zehnder, it picks up a phase of ϕ and there is no dependence in the coherent state no matter the intensity. When a number state passes through a phase shift, the phase shift is directly proportional to the number of photons n in that state, and it picks up a phase $(n \cdot \phi)$. Therefore the use of photon number states can increase the frequency of interference fringes by a factor of n and increase the precision in estimating an unknown change in phase ϕ [85].

A point that we want to focus on is that the matrix representation of a Mach-Zehnder interferometer in Equation (5.26) is exactly that of a single beam-splitter with variable reflectivity [54]:

$$\eta = \sin^2 \frac{\phi}{2}. \tag{5.30}$$

This means that a Mach-Zehnder can be mimicked with a variable beam-splitter. We change the beam-splitter reflectivities, η, and measure the resulting output photon number events, which gives a similar result as changing the parameter ϕ of a Mach-Zehnder interferometer. The analogy of the Mach-Zehnder to the variable beam splitter allows us to use a simpler setup (beam splitter vs Mach-Zehnder) to demonstrate the proof-of-principle of increased sensitivity, which we will show turns out to be very useful for certain experiments.

First let us look at what happens when we insert one photon into each input

port of a Mach-Zehnder $|1\rangle_a |1\rangle_b$. Here each step, as the state evolves through the interferometer, will be written out for clarity in creation operator and Fock state notation. After the first beam-splitter:

$$|\psi_{\text{in}}\rangle = \hat{a}_a^\dagger \hat{a}_b^\dagger |0\rangle \tag{5.31}$$

$$\xrightarrow{H_{bs}} (R\hat{a}_c^\dagger + T\hat{a}_d^\dagger)(T\hat{a}_c^\dagger - R\hat{a}_d^\dagger) |0\rangle \tag{5.32}$$

$$= \frac{1}{2}(\hat{a}_c^\dagger \hat{a}_c^\dagger - \hat{a}_d^\dagger \hat{a}_d^\dagger) |0\rangle \tag{5.33}$$

$$= = \frac{1}{\sqrt{2}}(|2\rangle_c |0\rangle_d - |0\rangle_c |2\rangle_d) \tag{5.34}$$

assuming we have a 50:50 beam-splitter such that $R = T = 1/\sqrt{2}$. Then after the phase shift

$$\xrightarrow{Z\phi} \frac{1}{2}\left(\hat{a}_e^{\dagger 2} e^{i\phi} - \hat{a}_f^{\dagger 2} e^{-i\phi}\right) |0\rangle \tag{5.35}$$

$$= -\frac{1}{\sqrt{2}}\left(e^{i\phi} |2\rangle_e |0\rangle_f - e^{-i\phi} |0\rangle_e |2\rangle_f\right). \tag{5.36}$$

Then after the second beam-splitter

$$\xrightarrow{H_{bs}} \frac{1}{2}\left(\hat{a}_g^{\dagger 2}\cos(\phi) + 2\hat{a}_g^\dagger \hat{a}_h^\dagger \sin(\phi) + \hat{a}_h^{\dagger 2}\cos(\phi)\right) |0\rangle \tag{5.37}$$

$$|\psi_{\text{out}}\rangle = \frac{\cos(\phi)}{2}\left(|2\rangle_g |0\rangle_h + |0\rangle_g |2\rangle_h\right) + \sin(\phi) |1\rangle_g |1\rangle_h, \tag{5.38}$$

which now has the same signature of a HOM dip but instead of changing the timing of the interfering photons, the phase shift in the Mach-Zehnder is changed. This signature is shown as the blue curve in Figure 5.6(a). It is referred to as the 1111 case because it is the case when two heralded sources herald on one photon and the two detectors after the variable beamsplitter also both detect one photon.

Let us look at what happens when we insert two photons into each input port of a Mach-Zehnder $|2\rangle_a |2\rangle_b$. Here each step, as the state evolves through the interfer-

ometer, will be written out for clarity in creation operator and Fock state notation. After the first beam-splitter:

$$|\psi_{\text{in}}\rangle = \hat{a}_a^{\dagger 2}\hat{a}_b^{\dagger 2}|0\rangle \tag{5.39}$$

$$\xrightarrow{H_{bs}} \frac{1}{2}(R\hat{a}_c^\dagger + T\hat{a}_d^\dagger)^2(T\hat{a}_c^\dagger - R\hat{a}_d^\dagger)^2|0\rangle \tag{5.40}$$

$$= \left(-\frac{1}{4}\hat{a}_c^{\dagger 2}\hat{a}_d^{\dagger 2} - \frac{1}{8}(\hat{a}_c^{\dagger 4} + \hat{a}_d^{\dagger 4})\right)|0\rangle \tag{5.41}$$

$$= -\frac{1}{\sqrt{4}}|2\rangle_c|2\rangle_d - \frac{3}{\sqrt{4}}\left(\frac{|4\rangle_c|0\rangle_d + |0\rangle_c|4\rangle_d}{\sqrt{2}}\right) \tag{5.42}$$

assuming we have a 50:50 beam-splitter such that $R = T = 1/\sqrt{2}$. Then after the phase shift

$$\xrightarrow{Z\phi} \left(-\frac{1}{4}\hat{a}_e^{\dagger 2}\hat{a}_f^{\dagger 2} - \frac{e^{i2\phi}}{8}\hat{a}_e^{\dagger 4} + \frac{e^{-i2\phi}}{8}\hat{a}_f^{\dagger 4}\right)|0\rangle \tag{5.43}$$

$$= -\frac{1}{\sqrt{4}}|2\rangle_e|2\rangle_f - \frac{3}{\sqrt{4}}e^{i2\phi}\left(\frac{|4\rangle_e|0\rangle_f + e^{-i4\phi}|0\rangle_e|4\rangle_f}{\sqrt{2}}\right). \tag{5.44}$$

Then after the second beam-splitter

$$\xrightarrow{H_{bs}} \left(\frac{(1-\cos 2\phi)}{16}(\hat{a}_g^{\dagger 4} + \hat{a}_h^{\dagger 4}) + \frac{(1+3\cos 2\phi)}{8}\hat{a}_g^{\dagger 2}\hat{a}_h^{\dagger 2} + \frac{\sin 2\phi}{4}(\hat{a}_g^{\dagger 3}\hat{a}_h^\dagger - \hat{a}_g^\dagger\hat{a}_h^{\dagger 3})|0\rangle\right)|0\rangle \tag{5.45}$$

$$|\psi_{\text{out}}\rangle = \frac{\sqrt{3}}{4}(1-\cos 2\phi)\left(\frac{|4\rangle_g|0\rangle_h + |0\rangle_g|4\rangle_h}{\sqrt{2}}\right) + \frac{(1+3\cos 2\phi)}{4}|2\rangle_g|2\rangle_h \tag{5.46}$$

$$+ \frac{\sqrt{3}}{2}\sin 2\phi\left(\frac{|3\rangle_g|1\rangle_h - |1\rangle_g|3\rangle_h}{\sqrt{2}}\right). \tag{5.47}$$

If we look at the probability of measuring $|2\rangle_g|2\rangle_h$ in terms of the variable reflectivity from Equation (5.30), we see that:

$$\left|\frac{(1+3\cos 2\phi)}{4}\right|^2 \quad \rightarrow \quad \left|\frac{(1+3(1-8\eta(1-\eta))^2}{4}\right|^2, \tag{5.48}$$

which is plotted as the orange curve in Figure 5.6 (a) without accounting for any loss or noise effects. We shall explore more realistic simulations in the following section.

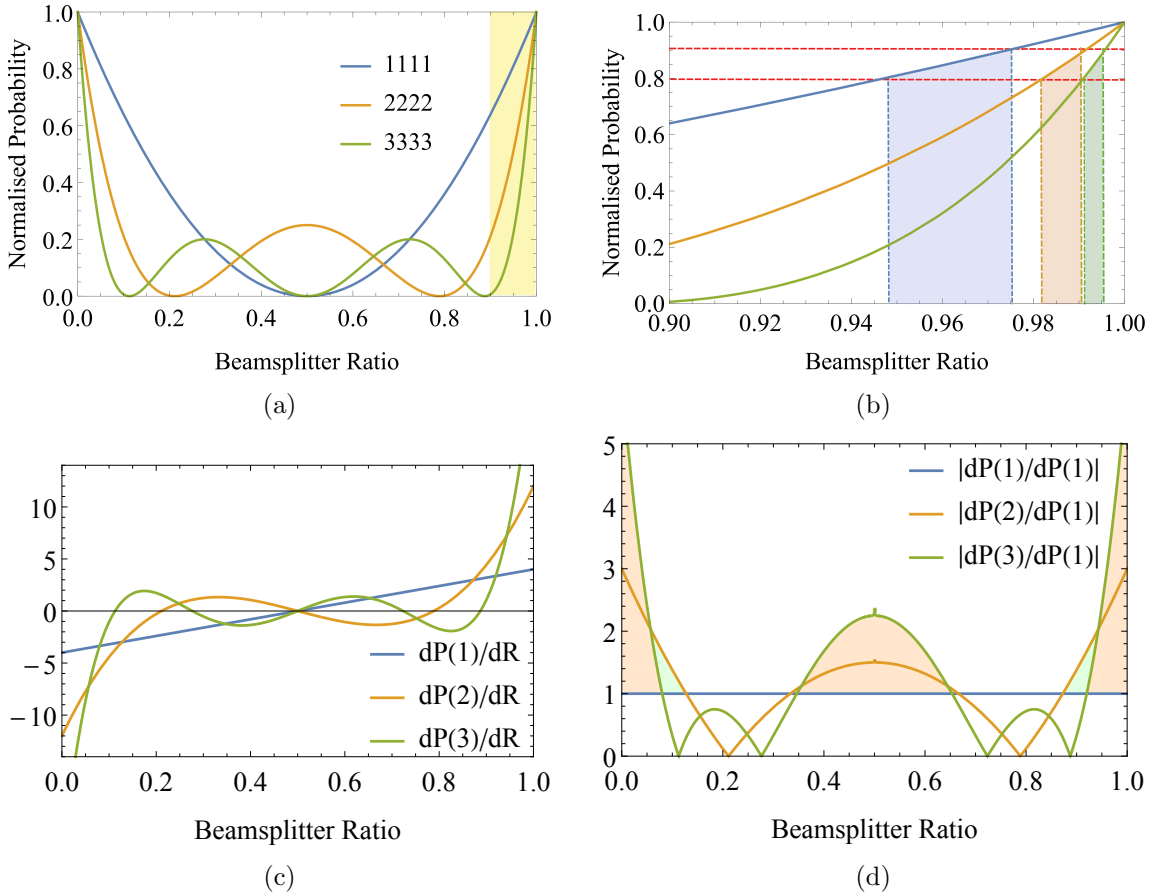


Figure 5.6: In Figure (a) we plot the simulated normalized probabilities for the 1111, 2222, and 3333 case with 100% efficiency. The highlighted yellow section is then zoomed in and shown in Figure (b). This helps us see that for the same vertical uncertainty, the probability for the normalized 1111, 2222, and 3333 case, the uncertainty for the beam-splitter ratio becomes less and less for different photon numbers: 0.027, 0.009, and 0.006 respectively. In Figure (c) we plot the derivatives of the probabilities as a function of the variable beam-splitter reflectivity, which shows that the slopes for higher photon numbers is largest towards the lower and higher end of the beam-splitter reflectivities. Figure (d) shows derivatives of the probabilities divided by the derivative of the probability of the 1111 case. This shows us all the times that the slopes are steeper than the 1111 case, which is the shaded area above 1. These are the areas that the higher 2222 or 3333 case have better sensitivity than the 1111 case.

5.2.2 Potential applications - Measuring increased sensitivity

Since a Mach-Zehnder interferometer can in turn be interpreted as a variable beam-splitter, the variable beam-splitter reflectivity can be measured with high precision

using higher-order Fock states. Looking at the output of the interferometer, the greater the slope the greater the sensitivity. From equation (5.30), we saw the connection between the phase shift in a Mach-Zehnder interferometer and the reflectivity in a single variable beam-splitter. Depending on the number of photons interfering, there will be regions of increased probability slopes as a function of the variable beam-splitter reflectivity, simulated in Figure 5.6(c). Therefore, the larger the slope, i.e. the change in the expected probability versus reflectivity of the variable beam-splitter, the larger the sensitivity to determine the reflectivity. For the higher photon number states, 2222 and 3333 case, the slope of the normalized probabilities is greater than in the 1111 case, particularly for smaller reflectivities, shown in Figure 5.6(d).

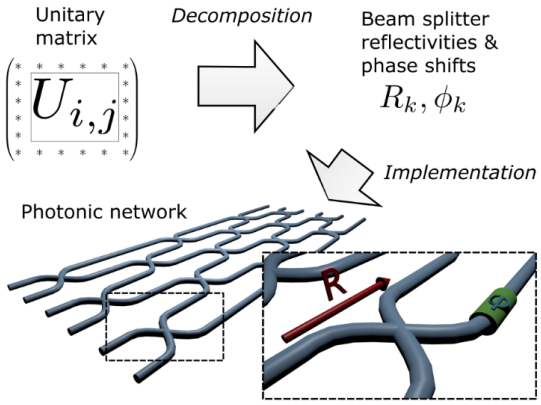


Figure 5.7: This figure is from Burgwal et al. [16] showing how a unitary matrix can be implemented into a multiport interferometer via a mathematical decomposition. The interferometer consists of pairs of beam splitters and phase shifters (see inset). The square decomposition results in the structure of the interferometer shown.

The question is: Is there a need for small reflectivities since typically interference is done with 50:50 beam-splitters. The answer is yes! To give some background, any unitary matrix can be decomposed into beam-splitters and phaseshifters as long as the the transformation from input to output is linear, shown in Figure 5.7. Boson

sampling is a great example of this. The question it answers is given N number of inputs into a random unitary, what is the output distribution? To resolve this, single photons are fed in as inputs to a large unitary interferometer, and the boson sampling task samples the output photon number distribution. If there are 10,000 beam-splitters in a random configuration, what beam-splitter reflectivities are required?

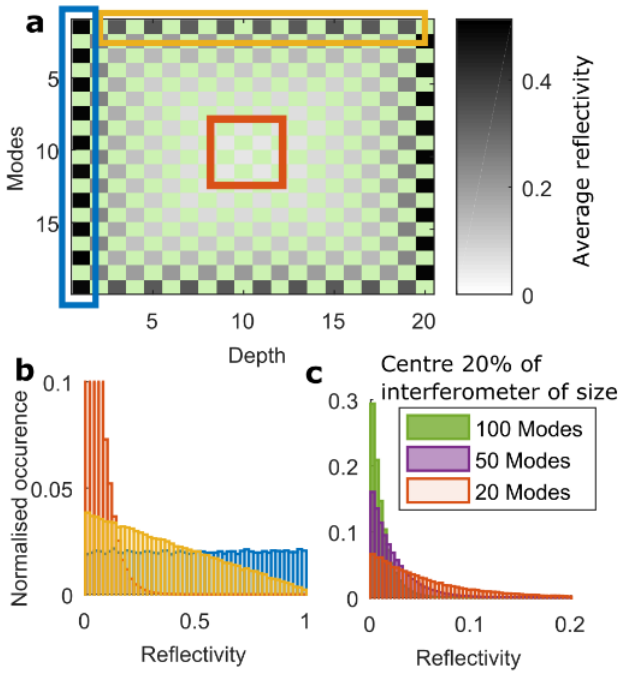


Figure 5.8: This figure is from Burgwal et al. paper [16]. Interferometers implementing unitary matrices show a specific distribution of beam splitter reflectivities. Figure (a) shows the spatial distribution of the average reflectivity in a size 20 interferometer. Figure (b) shows the underlying histograms for three regions in the interferometer, the first column, top row and centre. Figure (c) shows how the centre-of-interferometer histogram scales with the size of the interferometer. As the number of modes increase, smaller beam-splitter reflectivities are required.

A recent paper by Burgwal et al. studied the properties of large, integrated beam splitter networks that are used to implement random unitary matrices [16]. In doing so they found interesting scaling properties. As the size of the network increases, the majority of beam-splitters take on increasingly low reflectivities. They probe this sce-

nario by starting with a unitary transformation and using decomposition algorithms to translate the unitary into a set of beam splitter reflectivities and phase shifts. Surprisingly they find that already for a small network with 20 input and output modes, shown in Figure 5.8, the majority of beam-splitters have low reflectivities such that the average reflectivity is only 18%. As the number of modes increase and the interferometer becomes larger, the reflectivity distribution becomes more sharply peaked at low values and the overall average reflectivity becomes lower. They take note that one problem is that a realistic implementation using Mach-Zehnder interferometers is incapable of having a distribution of lower value reflectivities perfectly and thus has limited fidelity due to fabrication tolerances. Most reconfigurable realisations of multiport interferometers use Mach-Zehnder interferometers (MZIs) to implement variable beam-splitters [19, 95]. These interferometers contain two static 50:50 beam splitters, and in practice, these beam-splitters are not exactly 50:50, which means the MZI can generally not reflect or transmit all light. As shown above, low reflectivities are needed for the majority of MZIs in a large interferometer implementing random unitaries, thus this is problematic. We need a way to reliably measure the small reflectivities. Our approach is ideally suited to precisely determining low reflectivities and thus identifying suitable beam-splitters for such networks. With the advantage of high precision that means less measurements are required, hence less waiting time and better results.

So the big question is: can we do this with a lossy setup? Let us find out in the next section.

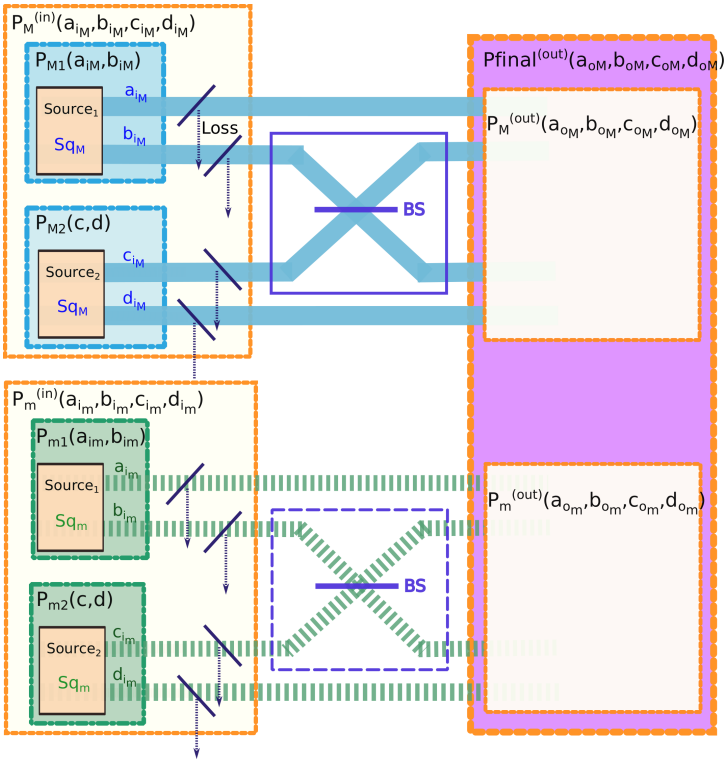


Figure 5.9: Here we model purity of two sources with two Schmidt modes. We have two sources: Source_1 and Source_2. Each source is comprised of a main squeezer Sq_M (represented with a capital M) and Sq_m (represented with a lower case m). The 2-dimensional joint probability distributions from the main squeezing contribution of both sources are combined(P_{M1} and P_{M2}), including effects from losses, to form the input 4-dimensional joint probability distribution, $\text{P}_\text{M}^{(\text{in})}$. The same is done for the contributing secondary squeezer, $\text{P}_\text{m}^{(\text{in})}$. Since the photons coming from the two different squeezers are distinguishable from each other, we model interfering the heralded photons from these squeezers separately. Starting with $\text{P}_\text{M}^{(\text{in})}$ and $\text{P}_\text{m}^{(\text{in})}$, we model heralding on the signal photon arms (a and d) and interfering on the idler arms (b and c). We then combine the resulting $\text{P}_\text{M}^{(\text{out})}$ and $\text{P}_\text{m}^{(\text{out})}$ to form the resulting output joint probability distribution $\text{P}_\text{final}^{(\text{out})}$, which models the two sources each comprised of two squeezers.

5.2.3 Joint probability distribution and loss simulations

To simulate this measurement as accurately as possible, we want a way to attain the full joint probability distribution after the idler arms of two sources (modes b and c) are interfered on a variable beam-splitter, shown in Figure 5.9. Each source, as we confirmed in Chapter 4 is composed of a main squeezer Sq_1 and a secondary squeezer

Sq_2. Since the photons from Sq_1 are distinguishable from Sq_2, they will not interfere on the beam-splitter. In order to appropriately model this, we will need to interfere the main squeezers and additional squeezers from each source separately and then combine their outputs at the end as shown in Figure 5.9. As in Chapter 4, we define the joint probability distribution for each squeezer

$$P_{\mathrm{Sq}}(n_s, n_i) = \delta_{n_s,n_i} \frac{\mu^n}{(1+\mu)^{n+1}} = \delta_{n_s,n_i} p_{\mu}^{\mathrm{therm}}(n), \tag{5.49}$$

and when including loss (discussed in section 4.2.3.2):

$$P_{\mathrm{Sq\&loss}}(n_s, n_i) = L_{n_j^s,k_j}(\eta_j^s) L_{n_j^i,k_j}(\eta_j^i) P_{\mathrm{Sq}}(n_s, n_i). \tag{5.50}$$

We will label the two-mode squeezed state coming from the main squeezer of source 1 and source 2 with a capitol M, P_{M1} and P_{M2} respectively, and from the secondary squeezer of source 1 and source 2 with a lower case m, P_{m1} and P_{m2} respectively. Then the four mode joint probability distribution which includes the same strength squeezer from the two different sources is:

$$\mathrm{P}_{\mathrm{M}}^{(\mathrm{in})}(a_{i_M}, b_{i_M}, c_{i_M}, d_{i_M}) = P_{\mathrm{M1}}(a_{i_M}, b_{i_M}) P_{\mathrm{M2}}(c_{i_M}, d_{i_M}) \tag{5.51}$$

$$\mathrm{P}_{\mathrm{m}}^{(\mathrm{in})}(a_{i_m}, b_{i_m}, c_{i_m}, d_{i_m}) = P_{\mathrm{m1}}(a_{i_m}, b_{i_m}) P_{\mathrm{m2}}(c_{i_m}, d_{i_m}), \tag{5.52}$$

where a, b, c, d indexed i_M are the inputs from the main squeezer and where they are indexed i_m are the inputs from the secondary squeezer. What we are really interested in is the output probability distribution which depends on the input joint probability distribution from Equation (5.52) and the interference of photons from arms b and c on a beam-splitter:

$$\mathrm{P}^{(\mathrm{out})}(a_o, b_o, c_o, d_o) = \sum_{b,c} \left| \mathrm{BS}(b_i, c_i; b_o, c_o) \right|^2 \mathrm{P}^{(\mathrm{in})}(a_i, b_i, c_i, d_i), \tag{5.53}$$

where a_o, b_o, c_o, d_o are the outputs and a_i, b_i, c_i, d_i are the inputs from either the main squeezer M or secondary squeezer m. The output probabilities, when the idler arms of two sources (modes b_i and c_i) are interfered on a beam-splitter, are given by the beam-splitter $\mathrm{BS}(b_i, c_i; b_o, c_o)$, which we will now discuss.

To describe the effect of the beam-splitter, we focus on the two idler arms from both sources (indicated by the purple dotted box in Figure 5.9). Since the two idler arms from separate sources are not correlated, we can ignore phase terms and assume the reflection, R, and transmission, T coefficients are real, such that

$$\mathrm{T} + \mathrm{R} = 1. \tag{5.54}$$

We want to determine the probability that given b_i and c_i number of photons from the idler arms as inputs into the beam-splitter, what is the probability of attaining b_o and c_o number of photons in the output arms. Since the photons are indistinguishable, the probability coefficients from the beam-splitter, BS, given b_i number of photons in port B gives c_{o_b} number of photons in output port C′, and $b_\mathrm{i} - c_{\mathrm{o}_b}$ photons in port B′, combined with the probability that given c_i number of photons in port C gives $c_\mathrm{o} - c_{\mathrm{o}_b}$ number of photons in port C′ and $c_\mathrm{i} - (c_\mathrm{o} - c_{\mathrm{o}_b})$ photons in port B′, are:

$$\mathrm{BS}(b_\mathrm{i}, c_\mathrm{i}; b_\mathrm{o}, c_\mathrm{o}) = \delta_{(b_\mathrm{i}+c_\mathrm{i}, b_\mathrm{o}+c_\mathrm{o})} \Bigg| \sum_{b_{\mathrm{o}b}}^{b_\mathrm{i}} \sqrt{b_\mathrm{o}! c_\mathrm{o}!} \binom{b_\mathrm{i}}{c_{\mathrm{o}b}} \sqrt{T}^{c_{\mathrm{o}_b}} \sqrt{R}^{(b_i - c_{\mathrm{o}_b})} \tag{5.55}$$

$$\binom{c_\mathrm{i}}{c_\mathrm{o} - c_{\mathrm{o}_b}} \sqrt{R}^{c_\mathrm{o} - c_{\mathrm{o}_b}} (-\sqrt{T})^{c_\mathrm{i} - (c_o - c_{\mathrm{o}_b})} \Bigg| \tag{5.56}$$

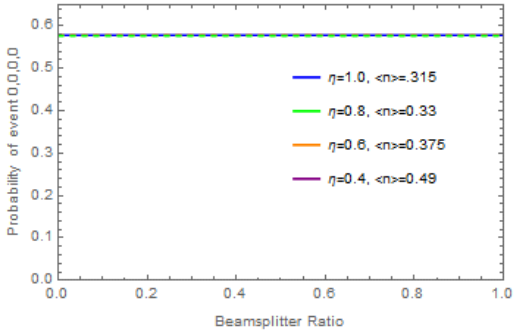
where $b_\mathrm{i}, c_\mathrm{i}$ and represent the inputs and $b_\mathrm{o}, c_\mathrm{o}$ represent the outputs.

So we get a $\mathrm{P}_M^{(\mathrm{out})}$ from the main squeezer $\mathrm{P}_M^{(\mathrm{in})}$ and $\mathrm{P}_m^{(\mathrm{out})}$ from the second squeezer. Then we combine the contributions from the main squeezer and secondary squeezer

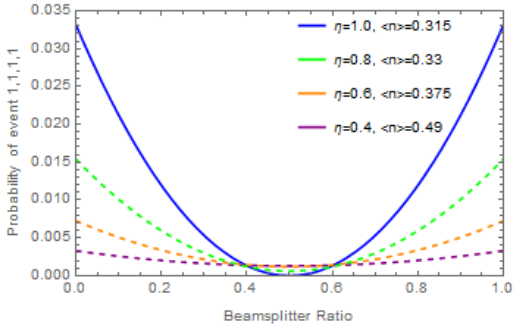
to describe the final total output joint probability distribution measured by the detectors:

$$\mathrm{P}_{\mathrm{final}}(a_o, b_o, c_o, d_o) = \sum_{a,b,c,d} \mathrm{P}_{\mathrm{M}}^{(\mathrm{in})}(a, b, c, d)\mathrm{P}_{\mathrm{m}}^{(\mathrm{in})}(a_o - a, b_o - b, c_o - c, d_o - d) \quad (5.57)$$

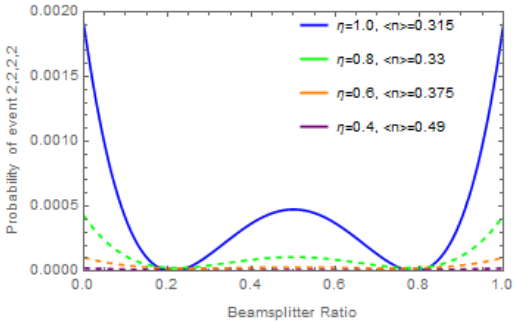
We plot the simulations of the coincidence counts on all four detectors as the variable beam-splitter ratio changes for different efficiencies in Figure 5.10 and show that for lower efficiencies not only does the total probabilities drop but also the finer features wash out. However Figure 5.11 shows that although the finer features near the middle reflectivity range wash out, there is still a sensitivity enhancement towards the lower and higher ends of the reflectivity range, even for low efficiencies such as 20%. This means that we can still reliably measure small reflectivitivities which is useful for the Burgwal et al. scenario [16].



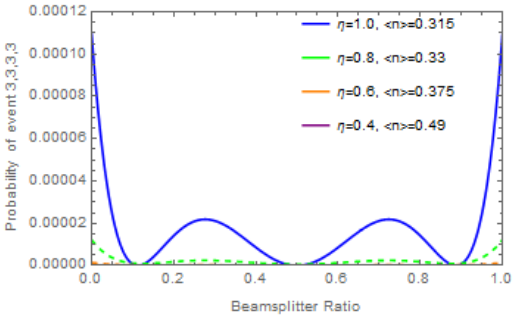
(a) 0000



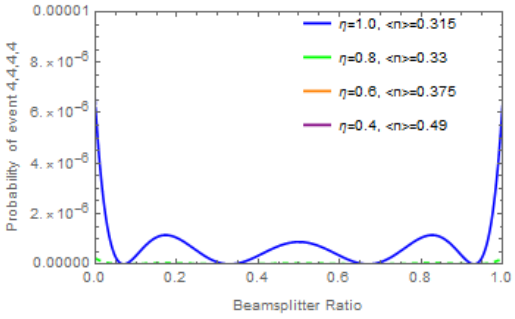
(b) 1111



(c) 2222



(d) 3333



(e) 4444

Figure 5.10: These simulations shows the coincidence counts on all four detectors as the variable beam-splitter ratio changes for different efficiencies 100%, 80%, 60% and 40% (blue, green, orange, and purple respectively). From top left to bottom, these plots show the probability of getting 0 photons in each detector; then 4-fold case when each detector measures a single photon 1,1,1,1; 8-fold when each detector measures two photons 2,2,2,2; 12-fold for the 3,3,3,3 case; and lastly 16-fold 4,4,4,4 case.

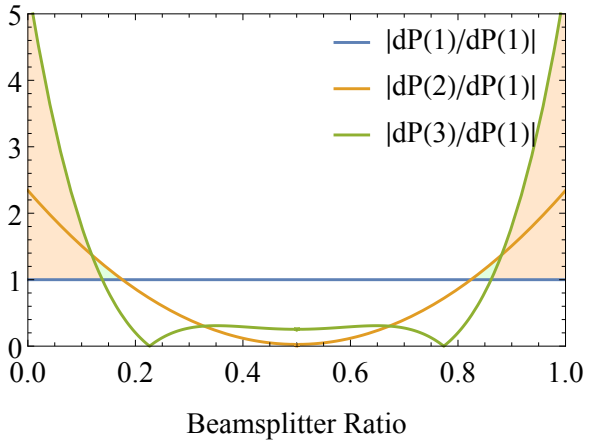


Figure 5.11: Here we plot the sensitivity plot (slope 2222/ slope 1111) for a very low efficiency 20% scenario to compare to the Figure 5.6(d), which showed the efficiency at 100%. It shows that if the loss is too large, we loose the advantage of better sensitivity as in the 100% efficient case, shown in Figure 5.6, around the reflectivity range of 0.35 and 0.65. However even though the fine features wash out near the middle of the beam-splitter reflectivity range, shown in Figure 5.10, this plot shows that towards the low ($< 15\%$) and high ($> 85\%$) ends of the reflectivity range, the slopes for the higher photon number 2222 and 3333 case are still steeper than the 1111 case. This is shown by the shaded area above 1. This means that even systems with low efficiency could be useful for the Burgwal et al. case [16].

5.3 Experimental measurements

For 23 different variable beam-splitter settings[3] our experimental data is represented by a 4-dimensional histogram, which provides the number of times a certain photon number configuration was measured by the four photon number resolving TES detectors. We use the same setup as the one used for the heralded single photon HOM measurement, Figure 5.1. But now instead of having the idler from two separate waveguide sources interfered on a balanced 50:50 beam-splitter, they are now interfered on a variable ratio coupler, also referred to as a variable fiber beam-splitter (VFB, Newport F-CPL-1550-P-FA), and detected with TES detectors instead of

[3]An arbitrary number of settings- it is necessary to have enough settings to see the signature but need to be aware that each setting takes 40 min.

nanowire detectors. This device transfers optical signals between fibers, similar to the function of bulk optic beam-splitters with controllable splitting ratio, by placing two fiber cores close together for evanescent field coupling. The splitting ratio is adjusted by changing the relative positions of the fibers with a micrometer.Since we focus on the events where each detector meausures a 1,1,1,1 or 2,2,2,2 event, the power was chosen so that barely any 3333 counts events occurred which meant aiming for a mean photon number of 0.2 per pulse (a 3333 coincidence count occurred 1:200 that a 2222 coincidence count occurred.) Each data point consisted of 700 iterations.

5.3.1 Determining BS ratio from single counts

For our experiment we will need to plot our data with respect to the variable beam-splitter coupling ratio. Since the micrometer is limited by its precision and issues from hysteresis, we use the single counts to determine the BS reflectivity, R, and transmission, $T = 1 - R$, in a way that also eliminates the effects of losses. If there were no losses, we could assume that the probability of photons coming from waveguide A will be reflected in the left arm $\mathrm{Prob}_L^{(A)}$, is the same as the BS reflectivity, which equals the number of clicks to the left divided by the total number of clicks in both arms, $R = N_L/(N_\mathrm{L} + N_\mathrm{R})$. However with losses this is not the case. Since the detectors are $> 90\%$ and there is not much loss from fiber connectors, we assume in our model that most of the loss happens before the beam-splitter due to fiber coupling. With losses in each arm, the probability of photons, coming from waveguide A, being reflected into the left arm, $\mathrm{Prob}_\mathrm{L}^{(A)}$, or transmitted into the right arm, $\mathrm{Prob}_\mathrm{R}^{(A)}$, is given by:

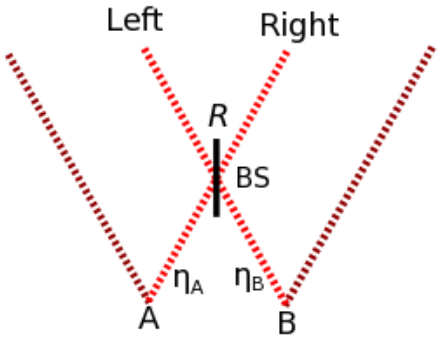


Figure 5.12: The idler photons from two SPDC sources, A and B, are interfered at a beam-splitter (BS) with a variable reflectivity R. The left and right arms before the beam-splitter have the corresponding efficiencies, η_A and η_B.

$$\text{Prob}_{\text{L}}^{(A)} = R \cdot \eta_A \qquad \text{Prob}_{\text{R}}^{(B)} = R \cdot \eta_{\text{B}}$$

$$\text{Prob}_{\text{R}}^{(A)} = (1 - R) \cdot \eta_{\text{A}} \qquad \text{Prob}_{L}^{(B)} = (1 - R) \cdot \eta_B$$

$$\text{Prob}_{L}^{(A)} + \text{Prob}_{R}^{(A)} = \eta_{\text{A}} \qquad \text{Prob}_{L}^{(B)} + \text{Prob}_{R}^{(B)} = \eta_{\text{R}}$$

where the efficiency of the left arm and right arm is η_L and η_R respectively. The reflectivity inferred with losses for source A and B is then:

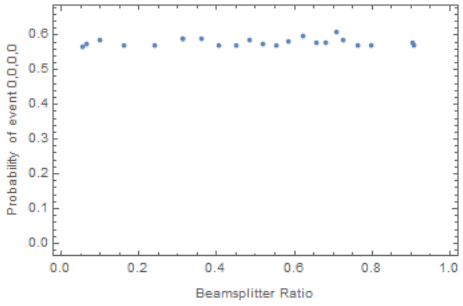
$$R = \frac{\text{Prob}_{\text{L}}^{(A)}}{\eta_A} \tag{5.58}$$

$$T = \frac{\text{Prob}_{\text{R}}^{(B)}}{\eta_B} \tag{5.59}$$

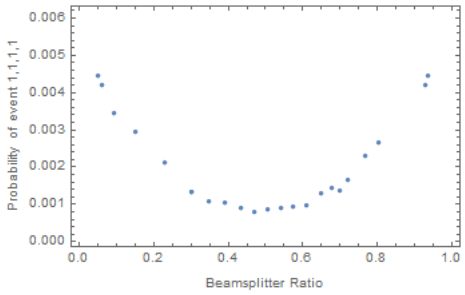
5.3.2 Multi-photon experimental measurements

After the measurement, we have 23 four-dimensional histograms, which provide the number of times a certain photon number configuration was measured by the four photon number resolving TES detectors, for each setting on the variable beamsplitter. The axes of these histograms is the measured photon number. For instance in the first bin is the 0000 case when all 4 detectors measured vacuum. We are interested in the

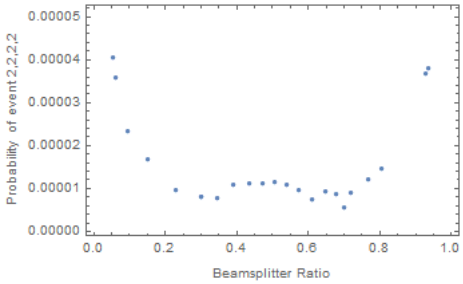
probability of measuring different joint photon number configurations (in particular measuring 1111 on all four detectors and 2222). To get the probability for each possible measured photon number combination, we take the 4-dimensional histogram and divide each element by the total number of events. We then have 23 different probabilities that we plot as a function of the variable beam-splitter coupling ratio, shown in Figure 5.13.



(a) 0000



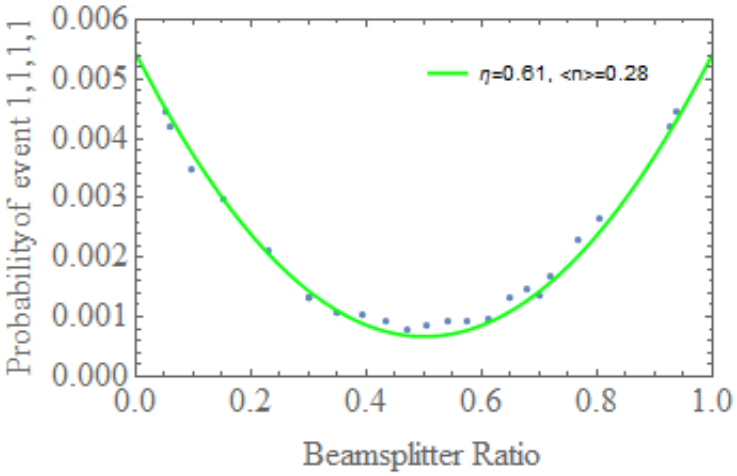
(b) 1111



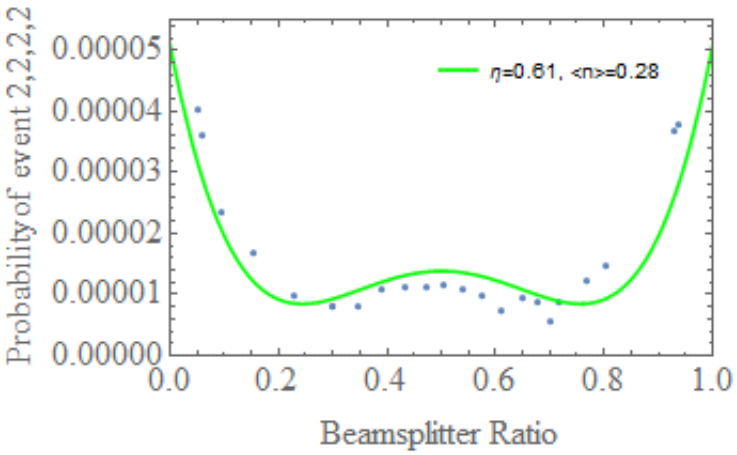
(c) 2222

Figure 5.13: Here are the data plots for the coincidence probabilities of all four detectors detecting 0000, 1111, and 2222 plotted against the BS ratio, which we attained from single counts discussed in the above section. At beam-splitter reflectivity of 0% and 100% the number of 2222 coincidences events is 1000. At reflectivity of 50% the number of 2222 coincidences events is 300 and at reflectivity of 25% the number of 2222 coincidences events is 200.

We then worked on theory curves to see if our measurements coincided with what we theoretically predict, see Figure 5.14.



(a) 1111



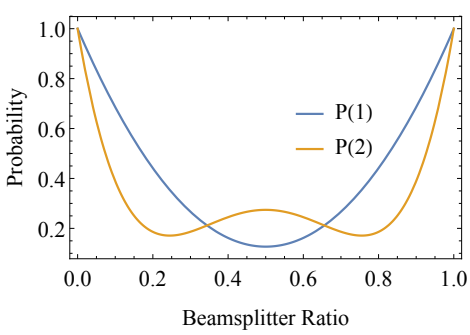
(b) 2222

Figure 5.14: These figures show the data from Figure 5.13 with the model plots. The best fit assumes a loss in each arm of 61% and a mean photon number of $\langle n \rangle = 0.28$. No scaling required. Error bars are smaller than data points.

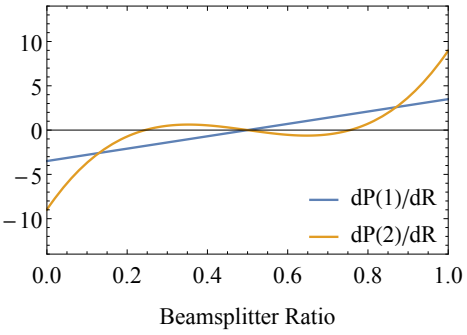
We had prepared to simulate the total output joint probability distribution by combining the contributions from a main squeezer and a secondary squeezer. However for these measurements, our fits overlap with the data better if we just took into account a main squeezer and ignored the secondary contribution for the time being. To fit them well, there was a bit of trial and error. We had the flexibility to adjust the

efficiency in both arms and to change the incoming mean photon number. We used the 0000 case to set the appropriate combination of efficiency and mean photon number. For example if we assume that the efficiency was high, then the corresponding mean photon number would have to be low in order to match with the data probability of getting the 0000 case. Then with trial and error we tested those combinations against our 1111 and 2222 data curves. In the previous chapter we had measured efficiencies of 50% and 35% and aimed for roughly 0.20 photons per pulse but the measured mean photon number oscillated between 0.275 and 0.288. The best fit assumes an efficiency in each arm of 61% and a mean photon number of $\langle n \rangle = 0.28$ which generally is in good agreement with the measurements. Further refinement of the theory is one of the future steps that should be taken in this setup.

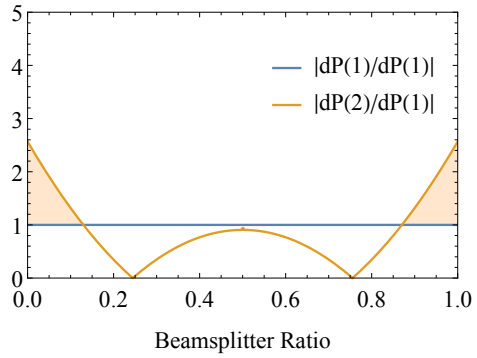
The big question is whether we can extract an increased sensitivity from these measurement results, specifically at low and high beamsplitter reflectivities, which are useful as mentioned for large, integrated beam splitter networks [16]. In order to determine if we have indeed reached increased sensitivity with measurements, we need to compare the slope of the 2222 case to the 1111 case, shown in Figure 5.15. It shows that yes there is higher sensitivity for certain beam-splitter ratios! If we look at Figure 5.15(d), the ratio of the 2222 slope to the 1111 slope for the lowest and highest beam-splitter reflectivities is slightly less (2.6 compared to 3 for the perfect scenario, shown in Figure 5.6(d).



(a) 1111



(b) 2222



(c) 3333

Figure 5.15: In figure (a) we plot fits for the normalized probabilities for the 1111 and 2222 experimental case. In figure (b) we plot the derivatives of the probabilities as a function of the variable beam-splitter reflectivity. Figure (c) shows derivatives of the probabilities divided by the derivative of the probability of the 1111 case. This shows us all the times that the slopes are steeper than the 1111 case. which is the shaded area above 1.

5.4 Pressing forward for higher-photon number heralded Fock states

Now is a very exciting time to press forward with experiments. We have integrated a new 1550 nm source with TES photon number resolving detectors. We have shown that the heralded photons are indeed pure and very nearly indistinguishable from separate waveguide sources with the signature HOM dip measurement. On that chip alone, there are 18 waveguides so the possibility to interfere indistinguishable photons from 18 different sources. With our setup we were able to show the 2,2,2,2 signature

which has never been shown before. We were able to demonstrate an enhanced sensitivity when measuring the reflectivity of a beam splitter.

However, because of losses, we had to keep the power as low as possible so higher order photon numbers would not contaminate the measurement. For this experimental run, the repetition rate for the pump pulses were set to 100 KHz to allow enough reset-time for the TES detectors. The pump pulse energy was set to 2.5 pJ in each arm leading to a mean photon number of $\langle n \rangle = 0.28$. The run took over 20 hours and there were power fluctuations from the laser, which coincided with the air conditioning 30 min cycles, that we will see in our data. It was not carried out for this experiment, but for future runs it is recommended to use a power stabilizing feedback system. In addition, the position of the variable beam-splitter for this measurement had to be manually adjusted every half hour. A new system has been made which rotates the beam-splitter via a motorized waveplate.

We are nearly at 3,3,3,3 (unfortunately power fluctuations and then ultimately the laser breaking down prevented the final measurement but the beginnings of a slight signature show that that measurement is really close).

But what happens as we go to larger heralded photon number states? Figure 5.10 shows the expected signatures for the 4-fold, 8-fold, 12-fold, and 16-fold case. As one can see, the larger the heralded photon number state, the more oscillations in the signature. But to get these larger photon number states to see these fine oscillations, the main issue that needs to be resolved is loss. Loss causes the fine signature to become contaminated as the probability of achieving such a state decreases. The high TES detector efficiencies are obviously beneficial, however loss needs to be improved

along the path from chip to detector, specifically fiber in-coupling and the variable beam-splitter. Also there seems to be some noise from a second squeezer. Having tried everything to optimise in-coupling into the waveguide, the source is probably from some irregularities in the waveguide periodic poling or from the tear-drop shape of the waveguides that is currently inevitable during fabrication.

Chapter 6

Conclusion

The main goal of my DPhil has been to push the frontier of quantum optics. With the advent of new high efficiency photon-number resolving transition edge sensor (TES) detectors that work at telecom wavelengths, our group required single photon sources which generated single photons around 1550 nm wavelengths to take advantage of the low losses and mature telecommunication technology at this regime. During my DPhil I worked on building two such sources in KTP waveguides so that we could explore multi-photon state measurements that had never been explored before. This required sources that are bright and emit heralded photons that are pure and indistinguishable.

Therefore once the sources were built, extensive characterisation of the sources was required. First we measured and analysed the joint spectral intensity (JSI) from both sources (discussed in Chapter 2). We were able to conclude that the idlers from the two separate sources are spectrally indistinguishable by 99% and centred at 1547 nm and that the signal photons were centered at 1554 nm. From the JSI we determined that the sources have a lower bound Schmidt number equal to 1.06 (where a Schmidt number equal to one is the ideal single mode scenario). To determine if any phase correlations exist, we perform the unheralded second order correlation function

($g^{(2)}$) with APD click detectors and then later with photon number resolving TES detectors (discussed in Chapter 3). With APD detectors, we measure an unheralded $g^{(2)}$ of 1.91 ± 0.04 which corresponds to a Schmidt number of 1.10 ± 0.05. With TES detectors we measure an unheralded $g^{(2)}$ of 1.85, which corresponds to a Schmidt number of 1.17[1]. The APD and TES measurements are in reasonable agreement within the experimental precision.

With photon number resolving detectors, we are able to analyze the marginal and joint photon number distribution of the photon pairs generated (discussed in Chapter 4). This allows us to characterize our source with a greater level of detail and determine that our source entails not just a single main squeezer but also a second squeezer which contributed to the total emission by around 9% with negligible additional thermal and Poissonian noise contributions, corresponding to a Schmidt number of 1.17 which is also in agreement with our measurements and reaffirms that our sources generate high-quality photons. With the joint probability statistics we are able to determine that the Klyshko efficiency in each arm is 47% and 32%. We are able to quantify multi-photon contamination and loss. Our source is uniquely bright. In fact the lowest mean photon number we generally operate is 0.1 photons per pulse, such that the probability of generating two photon pairs is 5% compared to the single pair probability. At this mean photon number, we achieve a heralded $g^{(2)}$ of 0.2 with TESs. Although this value seems high compared to other values in the literature, it is well below a $g^{(2)}$ of 0.5 which identifies our source as a single photon source and is a better value than if measured with APDs. With photon

[1]Due to the statistics, the error is insignificant.

number resolving detectors, we are also able to show that we can herald higher photon number states, which will be used in Chapter 5. In the beginning of Chapter 5 we focus on the interference of heralded photons from two independent source in a Hong-Ou-Mandel (HOM) setup measured with nanowire click detectors. Having measured a dip visibility of 85.9%, which corresponds to a Schmidt number of 1.64 (again in agreement with all other measurements), we conclude that since the photons' spectral overlap is quite high, the secondary squeezer during the process is preventing us from reaching higher visibilities.

Having set up, fully characterized and integrated the new sources with single-photon number resolving detectors, we conclude the thesis by discussing the measurement of the interference of heralded two-photon Fock states, which has not been feasible previously. We are able to demonstrate the signature of interfering 2-photon Fock states in a Mach-Zehnder by using an analogous variable beam-splitter. Instead of changing the phase in one of the arms of a Mach-Zehnder, we can perform an analogous task by changing the reflectivity of a variable beam-splitter. Because of losses, the mean photon number had to be kept relatively low (≈ 0.2). This measurement took over 20 hours (and required manually changing the reflectivity of the beamsplitter every half hour). In the end, we show 2-photon Fock state interference at different settings of a variable beam-splitter, which has not been performed before. We also developed a complete theory framework that includes losses and other imperfections, such as noise contributions, and then we were able to reproduce our results experimentally with good precision. We have evaluated the measurements, and we demonstrated an increased measurement sensitivity for the two-photon Fock

states when compared to the single-photon Fock states - a genuine quantum advantage. We have seen that this advantage works for very low ($< 15\%$) and very high ($> 85\%$) beam splitter reflectivities, which is an important regime for the characterisation of future integrated linear optical quantum networks, which heavily rely on low-reflectivity beam-splitters.

By using multi-photon number states, there is the possibility to explore increased measurement precision compared to coherent states, a result that is of great interest for the field of quantum metrology. This work paves a route towards new approaches to studying 'high' photon number states for quantum-enhanced metrology. Multi-photon number states are also useful for new interferometric protocols such as quantum walks, which provide simple models of various fundamental processes [96]. A quantum walk has the potential as a framework for developing new quantum algorithms with many indistinguishable particles and measurements of non-classical multi-particle correlations. With the benefits of multi-photon number state, it would be possible to explore 'quantum leaps, which is a process that can be achieved with fewer resources and that in a single step simulates another long process a leap immediately gives a probability distribution which results only after many steps. Multi-photon states will also be useful for all-optical quantum information processing, based on the prepared multi-photon entangled states as the ancilla [64], and for quantum communication and quantum cryptography [75].

However before pushing immediately forward to these multiphoton experiments, I would highly recommend investing in a better laser system and dilution fridge for the superconducting detectors. The detectors we used were in an older open dilution

fridge, which meant that having functioning detectors was incredibly inconsistent. Every time the fridge broke (which was often), it took at the least 3 weeks to warm up, fix and cool back down. Sometimes it would be out of commission for 3 months waiting for a part. And f the fridge was working than the laser was not. I was working with (blank old laser) which was on its last legs and had an issue with power fluctuations.

In conclusion, this thesis has laid the groundworks for future quantum applications that rely on higher-order Fock states. Without the content of this work - efficient sources, efficient detectors, a theory framework to describe the processes from generation to detection - these applications would stay out of reach. Our next steps in this setup would focus on increasing the overall efficiency, which currently limits the highest achievable photon numbers. With foreseeable improvements, we envision that this setup can generate heralded four-photon Fock states with good fidelities at rates of up to several Hertz. This will bring into reach new and exciting applications that will enable us to make full use of the quantum advantage provided by exotic quantum states of light.

Appendix A

Schmidt number from mean photon number weights

This derivation provides the corresponding Schmidt number given the mean photon number weights of two squeezers. For general details on the utilized language, see [22]. The overall mean photon number $\langle n \rangle$ is a sum of the mean photon numbers of the contributing factors:

$$\langle n \rangle = \langle n_0 \rangle + \langle n_1 \rangle . \tag{A.1}$$

Given the PDC output:

$$|\Psi\rangle = B \int_0^\infty d\omega_i d\omega_s f(\omega_i, \omega_s) \, |\omega_i, \omega_s\rangle . \tag{A.2}$$

From Schmidt decomposition [90], we showed from Equation (3.1) that we can decompose the joint spectral amplitude (which contains spectral and phase information) into orthonormal basis functions g_k and h_k [67]:

$$Bf(\omega_i, \omega_s) = \sum_k r_k g_k(\omega_i) h_k(\omega_s) \qquad \text{and} \qquad \sum_k r_k^2 = B^2, \tag{A.3}$$

where ω_i and ω_s are the frequencies of the signal and idler photons, r_k is the squeezing amplitudes associated with mode k, and B is the overall gain of the process. The

distribution of squeezing weights r_k can be split into a normalized distribution λ_k ($\sum_k \lambda_k^2 = 1$) that characterizes the probability for occupation of different squeezers in the respective optical quantum state, and the overall gain of the process $B \in \mathbb{R}^+$, which quantifies the total amount of generated squeezing according to $r_k = B\lambda_k$. The mean photon number in the k-th squeezer is related to the the normalised distribution λ_k and the gain B by:

$$\langle n \rangle_k = \sinh(\lambda_k B), \tag{A.4}$$

which in the low gain limit, such that $\langle n \rangle < 0.1$.

$$\langle n \rangle_k \approx \lambda_k^2 B^2. \tag{A.5}$$

From our measurements, we find relative weights of 1.00 and 0.09 of the two squeezers, such that

$$|n_1\rangle = \lambda_1^2 B^2 = 0.09 \langle n_0 \rangle = 0.09 \lambda_0^2 B^2 \tag{A.6}$$

We easily see that

$$\frac{1}{0.09} = \frac{\lambda_0^2}{\lambda_1^2} \quad \overset{\text{which leads to}}{\rightarrow} \quad \lambda_1^2 = 0.09\lambda_0^2 \tag{A.7}$$

From normalization,

$$\lambda_0^2 + \lambda_1^2 \quad = \quad \lambda_0^2 + 0.09\lambda_0^2 \quad \overset{!}{=} \quad 1, \tag{A.8}$$

which gives us

$$\lambda_0^2 = \frac{1}{1.09} \approx 0.917 \tag{A.9}$$

$$\lambda_1^2 \approx 0.083. \tag{A.10}$$

From these values, we can calculate the associated Schmidt number:

$$K = \frac{1}{\lambda_0^4 + \lambda_1^4} = \frac{1}{0.917^2 + 0.083^2} \approx 1.178. \tag{A.11}$$

Bibliography

[1] Pierre Aboussouan, Olivier Alibart, Daniel B. Ostrowsky, Pascal Baldi, and Sébastien Tanzilli. High-visibility two-photon interference at a telecom wavelength using picosecond-regime separated sources. *Physical Review A*, 81(2):021801, February 2010.

[2] Daryl Achilles, Christine Silberhorn, and Ian A. Walmsley. Direct, Loss-Tolerant Characterization of Nonclassical Photon Statistics. *Physical Review Letters*, 97(4):043602, July 2006.

[3] J. A. Armstrong, N. Bloembergen, J. Ducuing, and P. S. Pershan. Interactions between Light Waves in a Nonlinear Dielectric. *Physical Review*, 127(6):1918–1939, September 1962.

[4] M. Avenhaus, H. B. Coldenstrodt-Ronge, K. Laiho, W. Mauerer, I. A. Walmsley, and C. Silberhorn. Photon Number Statistics of Multimode Parametric Down-Conversion. *Physical Review Letters*, 101(5):053601, August 2008.

[5] M. Avenhaus, K. Laiho, M. V. Chekhova, and C. Silberhorn. Accessing Higher Order Correlations in Quantum Optical States by Time Multiplexing. *Physical Review Letters*, 104(6):063602, February 2010.

[6] Malte Avenhaus, Andreas Eckstein, Peter J. Mosley, and Christine Silberhorn. Fiber-assisted single-photon spectrograph. *Optics Letters*, 34(18):2873, September 2009.

[7] Burm Baek, Adriana E. Lita, Varun Verma, and Sae Woo Nam. Superconducting a-WxSi1-x nanowire single-photon detector with saturated internal quantum efficiency from visible to 1850 nm. *Applied Physics Letters*, 98(25):251105, June 2011.

[8] So-Young Baek, Osung Kwon, and Yoon-Ho Kim. Nonlocal dispersion control of a single-photon waveform. *Physical Review A*, 78(1):013816, July 2008.

[9] C. H. BENNETT. Quantum cryptography : Public key distribution and coin tossing. *Proc. of IEEE Int. Conf. on Comp., Syst. and Signal Proc., Bangalore, India, Dec. 10-12, 1984*, 1984.

[10] Charles H. Bennett. Quantum cryptography using any two nonorthogonal states. *Physical Review Letters*, 68(21):3121–3124, May 1992.

[11] RobertW Boyd. Nonlinear optics. In *Handbook of Laser Technology and Applications (Three- Volume Set)*, Handbook of Laser Technology and Applications, pages 161–183. Taylor & Francis, December 2003.

[12] Benjamin Brecht. Engineering ultrafast quantum frequency conversion. *MyScienceWork*, January 2014.

[13] G. Brida, M. V. Chekhova, M. Genovese, M. Gramegna, and L. A. Krivitsky. Dispersion Spreading of Biphotons in Optical Fibers and Two-Photon Interference. *Physical Review Letters*, 96(14):143601, April 2006.

[14] R. Hanbury Brown and R. Q. Twiss. Correlation between Photons in two Coherent Beams of Light. *Nature*, 177(4497):27–29, January 1956.

[15] I. A. Burenkov, A. K. Sharma, T. Gerrits, G. Harder, T. J. Bartley, C. Silberhorn, E. A. Goldschmidt, and S. V. Polyakov. Full statistical mode reconstruction of a light field via a photon-number-resolved measurement. *Physical Review A*, 95(5):053806, May 2017.

[16] Roel Burgwal, William R. Clements, Devin H. Smith, James C. Gates, W. Steven Kolthammer, Jelmer J. Renema, and Ian A. Walmsley. Implementing random unitaries in an imperfect photonic network. *arXiv:1704.01945 [quant-ph]*, April 2017.

[17] David C. Burnham and Donald L. Weinberg. Observation of Simultaneity in Parametric Production of Optical Photon Pairs. *Physical Review Letters*, 25(2):84–87, July 1970.

[18] X. Caillet, V. Berger, G. Leo, and S. Ducci. A semiconductor source of counterpropagating twin photons: A versatile device allowing the control of the two-photon state. *Journal of Modern Optics*, 56(2-3):232–239, January 2009.

[19] Jacques Carolan, Christopher Harrold, Chris Sparrow, Enrique Martín-López, Nicholas J. Russell, Joshua W. Silverstone, Peter J. Shadbolt, Nobuyuki Mat-

suda, Manabu Oguma, Mikitaka Itoh, Graham D. Marshall, Mark G. Thompson, Jonathan C. F. Matthews, Toshikazu Hashimoto, Jeremy L. O'Brien, and Anthony Laing. Universal linear optics. *Science*, 349(6249):711–716, August 2015.

[20] Carlton M. Caves. Quantum-mechanical noise in an interferometer. *Physical Review D*, 23(8):1693–1708, April 1981.

[21] Andreas Christ, Benjamin Brecht, Wolfgang Mauerer, and Christine Silberhorn. Theory of quantum frequency conversion and type-II parametric down-conversion in the high-gain regime. *New Journal of Physics*, 15(5):053038, 2013.

[22] Andreas Christ, Kaisa Laiho, Andreas Eckstein, Katiúscia N. Cassemiro, and Christine Silberhorn. Probing multimode squeezing with correlation functions. *New Journal of Physics*, 13(3):033027, 2011.

[23] Andreas Christ, Kaisa Laiho, Andreas Eckstein, Thomas Lauckner, Peter J. Mosley, and Christine Silberhorn. Spatial modes in waveguided parametric down-conversion. *Physical Review A*, 80(3):033829, September 2009.

[24] Andreas Christ and Christine Silberhorn. Limits on the deterministic creation of pure single-photon states using parametric down-conversion. *Physical Review A*, 85(2), February 2012.

[25] Laser Components. Single Photon Counting Modules. http://www.lasercomponents.com/us/photodiodes/avalanche-photodiodes/single-photon-counting-modules/.

[26] Hugues Guillet de Chatellus, Alexander V. Sergienko, Bahaa E. A. Saleh, Malvin C. Teich, and Giovanni Di Giuseppe. Non-collinear and non-degenerate polarization-entangled photon generation via concurrent type-I parametric downconversion in PPLN. *Optics Express*, 14(21):10060, October 2006.

[27] R. Demkowicz-Dobrzanski, M. Jarzyna, and J. Kolodynski. Quantum limits in optical interferometry. *arXiv:1405.7703 [quant-ph]*, 60:345–435, 2015.

[28] Valentin G. Dmitriev, Gagik G. Gurzadyan, and David N. Nikogosyan. *Handbook of Nonlinear Optical Crystals*. Springer, April 2013. Google-Books-ID: TZT6CAAAQBAJ.

[29] Jonathan P. Dowling. Quantum optical metrology – the lowdown on high-N00N states. *Contemporary Physics*, 49(2):125–143, March 2008.

[30] J. H. Eberly. Schmidt analysis of pure-state entanglement. *Laser Physics*, 16(6):921–926, June 2006.

[31] Andreas Eckstein, Guillaume Boucher, Aristide Lemaître, Pascal Filloux, Ivan Favero, Giuseppe Leo, John E. Sipe, Marco Liscidini, and Sara Ducci. High-resolution spectral characterization of two photon states via classical measurements. *Laser & Photonics Reviews*, 8(5):L76–L80, September 2014.

[32] Andreas Eckstein, Andreas Christ, Peter J. Mosley, and Christine Silberhorn. Highly Efficient Single-Pass Source of Pulsed Single-Mode Twin Beams of Light. *Physical Review Letters*, 106(1):013603, January 2011.

[33] A. Einstein. Über einen die Erzeugung und Verwandlung des Lichtes betreffenden heuristischen Gesichtspunkt. *Annalen der Physik*, 322(6):132–148, January 1905.

[34] M. D. Eisaman, J. Fan, A. Migdall, and S. V. Polyakov. Invited Review Article: Single-photon sources and detectors. *Review of Scientific Instruments*, 82(7):071101, July 2011.

[35] Marco Fiorentino, Sean M. Spillane, Raymond G. Beausoleil, Tony D. Roberts, Philip Battle, and Mark W. Munro. Spontaneous parametric down-conversion in periodically poled KTP waveguides and bulk crystals. *Optics Express*, 15(12):7479, 2007.

[36] K. Fradkin, A. Arie, A. Skliar, and G. Rosenman. Tunable midinfrared source by difference frequency generation in bulk periodically poled KTiOPO4. *Applied Physics Letters*, 74(7):914–916, February 1999.

[37] P. A. Franken and J. F. Ward. Optical Harmonics and Nonlinear Phenomena. *Reviews of Modern Physics*, 35(1):23–39, January 1963.

[38] T. Gerrits, F. Marsili, V. B. Verma, L. K. Shalm, M. Shaw, R. P. Mirin, and S. W. Nam. Spectral correlation measurements at the Hong-Ou-Mandel interference dip. *Physical Review A*, 91(1):013830, January 2015.

[39] Thomas Gerrits, Martin J. Stevens, Burm Baek, Brice Calkins, Adriana Lita, Scott Glancy, Emanuel Knill, Sae Woo Nam, Richard P. Mirin, Robert H. Hadfield, Ryan S. Bennink, Warren P. Grice, Sander Dorenbos, Tony Zijlstra,

Teun Klapwijk, and Val Zwiller. Generation of degenerate, factorizable, pulsed squeezed light at telecom wavelengths. *Optics Express*, 19(24):24434–24447, November 2011.

[40] R. Ghosh, C. K. Hong, Z. Y. Ou, and L. Mandel. Interference of two photons in parametric down conversion. *Physical Review A*, 34(5):3962–3968, November 1986.

[41] Vittorio Giovannetti, Seth Lloyd, and Lorenzo Maccone. Quantum-Enhanced Measurements: Beating the Standard Quantum Limit. *Science*, 306(5700):1330–1336, November 2004.

[42] Roy J. Glauber. The Quantum Theory of Optical Coherence. *Physical Review*, 130(6):2529–2539, June 1963.

[43] W. P. Grice, A. B. U'Ren, and I. A. Walmsley. Eliminating frequency and space-time correlations in multiphoton states. *Physical Review A*, 64(6):063815, November 2001.

[44] R. Grobe, K. Rzazewski, and J. H. Eberly. Measure of electron-electron correlation in atomic physics. *Journal of Physics B: Atomic, Molecular and Optical Physics*, 27(16):L503, 1994.

[45] Georg Harder, Vahid Ansari, Benjamin Brecht, Thomas Dirmeier, Christoph Marquardt, and Christine Silberhorn. An optimized photon pair source for quantum circuits. *Optics Express*, 21(12):13975, June 2013.

[46] Georg Harder, Tim J. Bartley, Adriana E. Lita, Sae Woo Nam, Thomas Gerrits, and Christine Silberhorn. Single-Mode Parametric-Down-Conversion States with 50 Photons as a Source for Mesoscopic Quantum Optics. *Physical Review Letters*, 116(14):143601, April 2016.

[47] Lukas G. Helt, Marco Liscidini, and John E. Sipe. How does it scale? Comparing quantum and classical nonlinear optical processes in integrated devices. *Journal of the Optical Society of America B*, 29(8):2199, August 2012.

[48] M. Hennrich, T. Legero, A. Kuhn, and G. Rempe. Photon statistics of a non-stationary periodically driven single-photon source. *New Journal of Physics*, 6(1):86, 2004.

[49] M. J. Holland and K. Burnett. Interferometric detection of optical phase shifts at the Heisenberg limit. *Physical Review Letters*, 71(9):1355–1358, August 1993.

[50] C. K. Hong and L. Mandel. Theory of parametric frequency down conversion of light. *Physical Review A*, 31(4):2409–2418, April 1985.

[51] C. K. Hong, Z. Y. Ou, and L. Mandel. Measurement of subpicosecond time intervals between two photons by interference. *Physical Review Letters*, 59(18):2044–2046, November 1987.

[52] K. D. Irwin and G. C. Hilton. Transition-Edge Sensors. In Christian Enss, editor, *Cryogenic Particle Detection*, number 99 in Topics in Applied Physics, pages 63–150. Springer Berlin Heidelberg, 2005.

[53] John C. Jacco. KTiOPO4 (KTP) Past, Present, And Future. volume 0968, pages 93–99, 1989.

[54] Vincent Jacques, E Wu, Frédéric Grosshans, François Treussart, Philippe Grangier, Alain Aspect, and Jean-François Roch. Delayed-Choice Test of Quantum Complementarity with Interfering Single Photons. *Physical Review Letters*, 100(22):220402, June 2008.

[55] Rui-Bo Jin, Thomas Gerrits, Mikio Fujiwara, Ryota Wakabayashi, Taro Yamashita, Shigehito Miki, Hirotaka Terai, Ryosuke Shimizu, Masahiro Takeoka, and Masahide Sasaki. Spectrally resolved Hong-Ou-Mandel interference between independent photon sources. *Optics Express*, 23(22):28836–28848, November 2015.

[56] Rui-Bo Jin, Jun Zhang, Ryosuke Shimizu, Nobuyuki Matsuda, Yasuyoshi Mitsumori, Hideo Kosaka, and Keiichi Edamatsu. High-visibility nonclassical interference between intrinsically pure heralded single photons and photons from a weak coherent field. *Physical Review A*, 83(3):031805, March 2011.

[57] Siddarth Koduru Joshi. *Entangled Photon Pairs: Efficient Generation and Detection, and Bit Commitment.* Thesis, July 2014.

[58] Satoshi Kako, Charles Santori, Katsuyuki Hoshino, Stephan Götzinger, Yoshihisa Yamamoto, and Yasuhiko Arakawa. A gallium nitride single-photon source operating at 200 K. *Nature Materials*, 5(11):887–892, November 2006.

[59] Kiyoshi Kato and Eiko Takaoka. Sellmeier and thermo-optic dispersion formulas for KTP. *Applied Optics*, 41(24):5040–5044, August 2002.

[60] Matthias Keller, Birgit Lange, Kazuhiro Hayasaka, Wolfgang Lange, and Herbert Walther. Continuous generation of single photons with controlled waveform in an ion-trap cavity system. *Nature*, 431(7012):1075–1078, October 2004.

[61] Yoon-Ho Kim and Warren P. Grice. Measurement of the spectral properties of the two-photon state generated via type II spontaneous parametric downconversion. *Optics Letters*, 30(8):908, April 2005.

[62] D N Klyshko. Utilization of vacuum fluctuations as an optical brightness standard. *Soviet Journal of Quantum Electronics*, 7(5):591–595, May 1977.

[63] D N Klyshko. Use of two-photon light for absolute calibration of photoelectric detectors. *Soviet Journal of Quantum Electronics*, 10(9):1112–1117, September 1980.

[64] E. Knill, R. Laflamme, and G. J. Milburn. A scheme for efficient quantum computation with linear optics. *Nature*, 409(6816):46–52, January 2001.

[65] Friedrich König and Franco N. C. Wong. Extended phase matching of second-harmonic generation in periodically poled KTiOPO4 with zero group-velocity mismatch. *Applied Physics Letters*, 84(10):1644–1646, March 2004.

[66] T. D. Ladd, F. Jelezko, R. Laflamme, Y. Nakamura, C. Monroe, and J. L. O'Brien. Quantum computers. *Nature*, 464(7285):45–53, March 2010.

[67] C. K. Law, I. A. Walmsley, and J. H. Eberly. Continuous Frequency Entanglement: Effective Finite Hilbert Space and Entropy Control. *Physical Review Letters*, 84(23):5304–5307, June 2000.

[68] Zachary H. Levine, Thomas Gerrits, Alan L. Migdall, Daniel V. Samarov, Brice Calkins, Adriana E. Lita, and Sae Woo Nam. Algorithm for finding clusters with a known distribution and its application to photon-number resolution using a superconducting transition-edge sensor. *Journal of the Optical Society of America B*, 29(8):2066, August 2012.

[69] M. Liscidini and J. E. Sipe. Stimulated Emission Tomography. *Physical Review Letters*, 111(19):193602, November 2013.

[70] A. E. Lita, B. Calkins, L. A. Pellouchoud, A. J. Miller, and S. Nam. Superconducting transition-edge sensors optimized for high-efficiency photon-number resolving detectors. volume 7681, pages 76810D–76810D–10, 2010.

[71] Adriana E. Lita, Aaron J. Miller, and Sae Woo Nam. Counting near-infrared single-photons with 95% efficiency. *Optics Express*, 16(5):3032, 2008.

[72] Rodney Loudon. *The Quantum Theory of Light*. OUP Oxford, September 2000.

[73] W. H. Louisell, A. Yariv, and A. E. Siegman. Quantum Fluctuations and Noise in Parametric Processes. I. *Physical Review*, 124(6):1646–1654, December 1961.

[74] A. I. Lvovsky, Wojciech Wasilewski, and Konrad Banaszek. Decomposing a pulsed optical parametric amplifier into independent squeezers. *Journal of Modern Optics*, 54(5):721–733, March 2007.

[75] Mehul Malik, Manuel Erhard, Marcus Huber, Mario Krenn, Robert Fickler, and Anton Zeilinger. Multi-photon entanglement in high dimensions. *Nature Photonics*, 10(4):248–252, April 2016.

[76] L. Mandel. Quantum effects in one-photon and two-photon interference. *Reviews of Modern Physics*, 71(2):S274–S282, March 1999.

[77] Elliott J. Mason, Marius A. Albota, Friedrich König, and Franco N. C. Wong. Efficient generation of tunable photon pairs at 08 and 16 mm. *Optics Letters*, 27(23):2115, December 2002.

[78] Wolfgang Mauerer, Malte Avenhaus, Wolfram Helwig, and Christine Silberhorn. How colors influence numbers: Photon statistics of parametric down-conversion. *Physical Review A*, 80(5):053815, November 2009.

[79] Christian Maurer, Christoph Becher, Carlos Russo, Jürgen Eschner, and Rainer Blatt. A single-photon source based on a single Ca + ion. *New Journal of Physics*, 6(1):94, 2004.

[80] Alan Migdall and et al. Single-Photon Generation and Detection: Physics and Applications. Vol. 45., 2013. Academic Press,.

[81] P. J. Mosley, J. S. Lundeen, B. J. Smith, and I. A. Walmsley. Conditional preparation of single photons using parametric downconversion: A recipe for purity. *New Journal of Physics*, 10(9):093011, 2008.

[82] Peter J. Mosley, Jeff S. Lundeen, Brian J. Smith, Piotr Wasylczyk, Alfred B. U'Ren, Christine Silberhorn, and Ian A. Walmsley. Heralded generation of

ultrafast single photons in pure quantum States. *Physical Review Letters*, 100(13):133601, April 2008.

[83] Michael A. Nielsen, Isaac Chuang, and Lov K. Grover. Quantum Computation and Quantum Information. *American Journal of Physics*, 70(5):558–559, April 2002.

[84] Jeremy L. O'brien, Akira Furusawa, and Jelena Vuckovic. Photonic quantum technologies. *Nature photonics*, 3(12):687–695, 2009.

[85] Ryo Okamoto, Holger F. Hofmann, Tomohisa Nagata, Jeremy L. O'Brien, Keiji Sasaki, and Shigeki Takeuchi. Beating the standard quantum limit: Phase super-sensitivity of N -photon interferometers. *New Journal of Physics*, 10(7):073033, 2008.

[86] Z. Y. Ou and L. Mandel. Further evidence of nonclassical behavior in optical interference. *Physical Review Letters*, 62(25):2941–2944, June 1989.

[87] Nicolás Quesada and J. E. Sipe. Effects of time ordering in quantum nonlinear optics. *Physical Review A*, 90(6), December 2014.

[88] Morton H. Rubin, David N. Klyshko, Y. H. Shih, and A. V. Sergienko. Theory of two-photon entanglement in type-II optical parametric down-conversion. *Physical Review A*, 50(6):5122–5133, December 1994.

[89] J. J. Sakurai, S. F. Tuan, and Eugene D. Commins. Modern Quantum Mechanics, Revised Edition. *American Journal of Physics*, 63(1):93–95, January 1995.

[90] Erhard Schmidt. Zur Theorie der linearen und nicht linearen Integralgleichungen Zweite Abhandlung. *Mathematische Annalen*, 64(2):161–174, June 1907.

[91] John M. Senior and M. Yousif Jamro. *Optical Fiber Communications: Principles and Practice*. Pearson Education, 2009. Google-Books-ID: 7HtqsEOMkXUC.

[92] Andrew J. Shields. Semiconductor quantum light sources. *Nature Photonics*, 1(4):215–223, April 2007.

[93] Christoph Söller. Optical fiber sources of pulsed single- and multi-photon states for quantum networks, Glasfaserquellen zur Erzeugung gepulster Ein- und Mehrphotonenzustände für Quantennetzwerke.

[94] J. Sperling, M. Bohmann, W. Vogel, G. Harder, B. Brecht, V. Ansari, and C. Silberhorn. Uncovering Quantum Correlations with Time-Multiplexed Click Detection. *Physical Review Letters*, 115(2):023601, July 2015.

[95] Justin B. Spring, Benjamin J. Metcalf, Peter C. Humphreys, W. Steven Kolthammer, Xian-Min Jin, Marco Barbieri, Animesh Datta, Nicholas Thomas-Peter, Nathan K. Langford, Dmytro Kundys, James C. Gates, Brian J. Smith, Peter G. R. Smith, and Ian A. Walmsley. Boson Sampling on a Photonic Chip. *Science*, page 1231692, December 2012.

[96] Magdalena Stobińska, Peter P. Rohde, and Paweł Kurzyński. Quantum leap: How to complete a quantum walk in a single step. *arXiv:1504.05480 [quant-ph]*, April 2015.

[97] Stefan Strauf, Nick G. Stoltz, Matthew T. Rakher, Larry A. Coldren, Pierre M. Petroff, and Dirk Bouwmeester. High-frequency single-photon source with polarization control. *Nature Photonics*, 1(12):704–708, December 2007.

[98] Magdalena Szczykulska, Tillmann Baumgratz, and Animesh Datta. Reaching for the quantum limits in the simultaneous estimation of phase and phase diffusion. *Quantum Science and Technology*, 2(4):044004, 2017.

[99] P. R. Tapster and J. G. Rarity. Photon statistics of pulsed parametric light. *Journal of Modern Optics*, 45(3):595–604, March 1998.

[100] Alfred B. U'Ren, Christine Silberhorn, Konrad Banaszek, and Ian A. Walmsley. Efficient Conditional Preparation of High-Fidelity Single Photon States for Fiber-Optic Quantum Networks. *Physical Review Letters*, 93(9):093601, August 2004.

[101] Alfred B. U'Ren, Christine Silberhorn, Reinhard Erdmann, Konrad Banaszek, Warren P. Grice, Ian A. Walmsley, and Michael G. Raymer. Generation of Pure-State Single-Photon Wavepackets by Conditional Preparation Based on Spontaneous Parametric Downconversion. *arXiv:quant-ph/0611019*, November 2006.

[102] Alejandra Valencia, Maria V. Chekhova, Alexei Trifonov, and Yanhua Shih. Entangled Two-Photon Wave Packet in a Dispersive Medium. *Physical Review Letters*, 88(18):183601, April 2002.

[103] Wojciech Wasilewski, Piotr Wasylczyk, Piotr Kolenderski, Konrad Banaszek, and Czeslaw Radzewicz. Joint spectrum of photon pairs measured by coincidence Fourier spectroscopy. *Optics Letters*, 31(8):1130, April 2006.

[104] B. Ya. Zel'Dovich and D. N. Klyshko. Field Statistics in Parametric Luminescence. *ZhETF Pisma Redaktsiiu*, 9:69, January 1969.

[105] F. C. Zumsteg, J. D. Bierlein, and T. E. Gier. KxRb1-xTiOPO4: A new nonlinear optical material. *Journal of Applied Physics*, 47(11):4980–4985, November 1976.